Analysis of MODIS-Aqua imagery to determine spring phytoplankton phenology in the Strait of Georgia, Canada

by

Tyson Kyle Carswell
BSc, University of Victoria, 2011

A Thesis Submitted in Partial Fulfillment
of the Requirements for the Degree of

MASTER OF SCIENCE

In the Department of Geography

Supervisory Committee

Analysis of MODIS-Aqua imagery to determine phytoplankton phenology in the Strait of Georgia, Canada

by

Tyson Kyle Carswell

BSc, University of Victoria, 2011

Supervisory Committee

Dr. Maycira Costa, (Department of Geography)
Supervisor

Dr. Jim Gower, (Department of Geography)
Committee member

Abstract

Supervisory Committee

Dr. Maycira Costa, (Department of Geography)
Supervisor

Dr. Jim Gower, (Department of Geography)
Committee member

The goal of this research was to construct a time series of accurate chlorophyll-*a* concentration for the Strait of Georgia (SoG), Canada, using an improved atmospheric correction scheme and workflow for the Moderate Resolution Imaging Spectroradiometer AQUA (MODIS) satellite instrument to describe the *chla* dynamics and spring bloom phenology in the SoG. *In situ* radiometric samples were acquired via Aerosol Robotic Network (AERONET), and hyperspectral data collected from a Hyperspectral Surface Acquisition System (HyperSAS) to assess three potential atmospheric correction schemes. Water property samples including total suspended material (TSM), chromophoric dissolved organic matter (CDOM), and chlorophyll concentrations (*chla*) were collected to further assess atmospheric corrections and the applied 'Ocean Color 3 Modis' (OC3M) standard chlorophyll algorithm. Regression, Absolute percentage difference (APD), Relative Percentage difference (RPD), and Root mean squared error (RMSE) analysis revealed the most appropriate method to be the 'Management Unit of the North Seas Mathematical Models' (MUMM) using the shortwave infrared spectrum (SWIR) to determine NIR-derived aerosol model. This method was used to construct a time series (July 2002-June 2014) of daily chlorophyll maps for all available imagery. Files were spatially binned into 8-day composites for the North and Central SoG where a

modified threshold-based definition was used to determine the start of the spring phytoplankton bloom period, as well as timing of maxima and duration of the largest spring bloom. Results indicate Central SoG start dates range from late February to late April, with an average start date at the last week of March. These results compare favorably to Hindcast predictive modelling of bloom start dates. The Northern SoG bloom phenology starts on average 9 days earlier, and experiences lower chlorophyll-*a* magnitudes. Hierarchical clustering with correlation similarity of spring seasons indicate 2008 and 2007 were anomalous, while 2009 and 2012 were the most correlated for blooms occurring in the spring season.

Table of Contents

List of Tables

List of Figures

List of Abbreviations and Symbols

Abbreviation/Symbol	Full Name	Units
λ	wavelength	nm
λ_0	reference wavelength	nm
a	absorption coefficient	m^{-1}
b_b	backscattering coefficient	m^{-1}
θ_s	solar zenith angle	
$\bar{F}_0$	extraterrestrial solar irradiance	
t	atmospheric diffuse transmittance	
ω_a	aerosol single scattering albedo	
ε	aerosol reflectance ratio	
τ_a	aerosol optical thickness	
α	fixed water reflectance ratio	
Chl*a*	chlorophyll-a concentration	Mg m^{-3}
aCDOM	absorbance from chromophoric dissolved organic material	
APD	absolute percentage deviation	
RPD	relative percentage deviation	
RMSE	root mean squared error	
n	number of samples	
l	path length	m
Å	angstrom coefficient	
MAD	median absolute deviation	
YD_{init}, YD_{dur}, YD_{max}	yearday initiation, duration, and maximum, respectively	
$R_{rs}(\lambda)$	remote sensing reflectance	
L	radiance	
ρ	reflectance	
TSM	total suspended material	Mg l^{-1}
ƒ	Aerosol size distribution	

Acknowledgements

There are several individuals paramount for completion of this thesis. First and foremost, the project would not have been possible without my supervisor, Maycira Costa. Her guidance and commitment to the project and student growth are truly appreciated. Secondly, I would like to thank my committee member Dr. Jim Gower for his support of my thesis. Dr. Gower brought needed clarity, editorial guidance, and was always available for expert advice.

I would like to thank Peter Chandler, Ruston Sweeting, Chrys Neville, and Dick Beamish for allowing me space and time on their research cruises. My fondest memories of this project are from these trips, as it allowed me to be engrossed in a learning atmosphere amongst consummate scientists.

The unwavering emotional and financial support, intellect, and endurance of my partner Erika Young cannot be understated. Erika was heavily involved in the processing of initial image data. Her efforts and knowledge of remote sensing were critical towards defining the final methods. This thesis would not exist without her.

The fellow members of the SPECTRAL Lab including Justin Belluz, Felipe Lobo, and Stephen Phillips all helped with various equipment, sampling, discussion, and most importantly, commiseration. Their teamwork, ability, and friendship are appreciated.

Lastly I would like to thank my parents, Linda and Barron. My mom has provided unwavering encouragement throughout my academic career. My father was the first scientist I was exposed to, and taught me to always ask “why” in search of truth. These are precious gifts, thank you.

Funding for this research has been generously provided by BCFRST NRAS program and by NSERC Discovery Grant to Dr. Maycira Costa.

Chapter 1 - Introduction

There is a need for improved monitoring, evaluation and reporting of dynamic processes such as ocean productivity, critical habitats, and fisheries in coastal environments, given the effects of increasing human pressures and a changing climate (Stelzenmüller *et al*., 2013). Traditional methods for monitoring coastal water properties typically rely on *in situ* sampling from ship or buoy based systems. These methods are often prohibitively costly and both spatially and temporally limited. The inability to effectively monitor and characterize these dynamic zones poses a significant barrier to fisheries and environmental management. As an example, the Fraser River sockeye salmon (*Oncorhynchus nerka*) stocks, an economically and ecologically important species, have experienced a marked decline with extreme intercohort condition and recruitment variability. It is hypothesized that stock variability is at least somewhat a function of timing of juvenile salmon marine entry (approximately static) to highly variable phytoplankton bloom timing and the closely coupled zooplankton populations (Beamish, Neville, Sweeting, & Lange, 2012; Thomson *et al.*, 2012). To assess the impact of bottom-up forcing on fish populations, there is a specific need of long-term spatio-temporal productivity data (Perry & Masson, 2013). Data derived from satellite remote sensing offer an unparalleled tool for synoptic biomass sampling associated with high (near daily) sampling frequencies.

Since the Coastal Zone Color Scanner proof of concept (CZCS, 1978-1986)(Gordon & Clark, 1981), satellite derived ocean colour has emerged as an important tool to monitor water

properties including phytoplankton over large areas at high temporal differences (McCain, Hooker, Feldman, & Bontempi, 2006). The success of CZCS prompted the National Aeronautical Space Administration (NASA) and the European Space Agency (ESA) to launch ocean colour sensors such as Sea-viewing Wide Field-of-View Sensor (SeaWiFS, 1997-2004), Medium Resolution Imaging Spectroradiometer (MERIS, 2002) and Moderate Resolution Imaging Spectroradiometer (MODIS, 1999 & 2002), Visible Infrared Imager Radiometer Suite (VIIRS) (Welsch *et al*., 2001), and the upcoming Sentinel-3 platforms (Drinkwater & Rebhan, 2005). Significant improvements in reliability and quality of spectral and radiometric instruments have been made. Several challenges, however, remain, and include effectively removing atmospheric interference from at-sensor satellite signals and developing robust satellite-based chlorophyll-*a* algorithms (Chen, Zhang, Cui, & Wen, 2013; Wang & Shi, 2005).

Confounding contributions to the signal detected by the satellite originate from absorption by gasses and aerosols (Fraser & Kaufman, 1985) as well as gas and aerosol scattering (Andre Morel & Prieur, 1977). Atmospheric correction derived for optically simple waters, typically found in open ocean where chlorophyll is the dominant optical constituent (case 1 waters), relies on the assumption of complete water absorption of all light in the near infrared spectrum (NIR). In these cases all signal detected is estimated as a function of atmospheric path radiance and sea surface reflectance; a concept commonly known as the black-pixel assumption (BPA) (Gordon & Wang, 1994, 'GW94'). This method is established and reliable for optically simple waters (McCain *et al*., 2006; McClain, 2009), and historical success of ocean colour for water monitoring has been performed here. In

these regions, variability of marine optical properties such as absorption and scattering is solely a function of phytoplankton composition (Morel & Prieur, 1977). Optics in coastal waters are more complex and the black-pixel assumption is not consistently effective (Dogliotti, Ruddick, Nechad, & Lasta, 2011). Here, total suspended material (TSM), which includes both organic and inorganic matter, often contribute to significant backscattering in the NIR (Doxaran, Cherukuru, & Lavender, 2006; Morel & Prieur, 1977; Morel, 1980; Ruddick, Ovidio, & Rijkeboer, 2000). The consequence is overestimation of aerosol reflectance due to contributions of suspended particle reflectance in the NIR. NIR band mischaracterization confounds the selection of appropriate atmospheric model, causing error in back calculations of path radiance and poor estimates of all spectral bands. The result is low or negative water leaving reflectances in the blue and unrealistic spectral distributions leading to the failure of chlorophyll-*a* (*chla*) and inherent optical property retrievals (Siegel, Wang, Maritorena, & Robinson, 2000; Zibordi, Mélin, *et al*., 2009). Therefore, there is a specific need for atmospheric corrections that are accurate and robust in coastal waters (Vanhellemont & Ruddick, 2015).

Algorithms to convert ocean color (i.e., spectral reflectance) to the phytoplankton proxy of chlorophyll-*a* (mg m^{-3}) have existed since early empirical regressions (Robinson, 2007) to semi analytical inversion techniques (Chen, Quan, & Cui, 2015; Zhongping Lee, Carder, Mobley, Steward, & Patch, 1998; Maritorena, Siegel, & Peterson, 2002), each with inherent advantages and disadvantages. Empirical algorithms based on band ratios of measured ocean color are the most numerous, and include the OC3M algorithm used in this study (O'Reilly *et al*., 2000). Regardless of chl*a* approach used, it is imperative that its

application for a region is assessed in respect to the absolute accuracy in determining *in situ chla* concentrations *(Morel et al*., 2007).

Positive contribution to ecosystem-based fisheries management (EBM), requires ocean colour products be analyzed and presented in a robust and interpretable manner to address specific objectives (Stuart & Platt, 2009). It is important that satellite derived biomass indicators, such as chlorophyll-*a*, be investigated and analyzed in a way consistent with known marine ecology dynamics. In particular, the onset and dispersal of phytoplankton blooms can be modelled in terms of phenology that describe magnitudes and durations (Blondeau-Patissier *et al.*, 2014).

The objectives of this research are (1) to evaluate MODIS-Aqua (here-after MODIS) derived *chla* products generated from three atmospheric correction schemes in the estuarine system of the Strait of Georgia, Canada, and (2) from the MODIS based chlorophyll products, define phenology indicators of the spring bloom in the central and north regions of the SoG. To accomplish this, the first step was to evaluate a time-series of MODIS imagery acquired from 2002 to 2014 for the Strait of Georgia based on three different atmospheric correction methods: (1) the NASA algorithm using 2-Band relative humidity based model selection and iterative NIR correction (hereafter, 'NIR' method), (2) the NASA algorithm with a substitution of SWIR bands (1240nm, 2130nm) ('SWIR' method), and (3) a GW94-based algorithm that assumes spatial homogeneity of the atmosphere over the region of interest (Ruddick *et al*., 2000) but with an additional modification using advantages of SWIR bands in turbid waters to estimate NIR

contributions ('MUMM+SWIR' method, Komick, 2007). Atmospherically corrected images were subjected to the OC3M chlorophyll algorithm and products assessed in comparison to *in situ chla*. The accuracy results were used to identify most accurate product, which was subsequently used to define bloom phenology.

MODIS offers over 14 years of daily data, enabling the investigation of long-term variability of water properties at both discrete and global scales. The sensor has 36 spectral bands, nine of which are frequently used for standard ocean color products. These are visible spectral bands centered at λ = 412, 443, 488, 531, 547, 667, and 678 nm, with two bands (748nm, 869nm) in the near infrared typically used to determine atmospheric aerosol properties (Meister, Franz, Kwiatkowska, & McClain, 2012), and shortwave infrared bands (1240nm, 2130nm) that have shown success in determining atmospheric aerosol properties in more turbid waters (Wang, Son, & Shi, 2009a; Wang, Son, Zhang, & Shi, 2013a).

The following chapters give an overview of atmospheric correction algorithms and the *chla* algorithm used in this research (Chapter 2), project procedures and evaluation methods (Chapter 3), results (chapter 4), discussion (chapter 5), and the general conclusion and recommendations of this research (Chapter 6).

Chapter 2 - Algorithms Description

The following section provides a brief review of NASA's Ocean Biology Processing Group (OBPG) standard Gordon & Wang (1994a) method for aerosol model selection. We provide theoretical background, justification and major assumptions for the different atmospheric-correction algorithms used in the present research, as well as the standard Ocean Color 3-MODIS (OC3M) algorithm used in this study to derive chlorophyll-*a* concentrations.

2.1 Atmospheric algorithms

Reflectance, ρ, is used in lieu of radiance L for this study. The terms are interchangeable through the equation $\rho = \pi L/F_0 \cos\theta_s$, where F_0 is extraterrestrial solar irradiance and θ_s is solar zenith angle (Kuchinke, Gordon, Harding, & Voss, 2009). MODIS sensor measured reflectance at top of atmosphere (TOA, ρ_t) is expressed as the sum of atmospheric and water contributions (Gordon & Wang, 1994):

$$\rho_{t(\lambda)} = \rho_r(\lambda) + \rho_a(\lambda) + \rho_{ra}(\lambda) + \rho_g(\lambda) + t(\lambda)\rho_w(\lambda) \quad (1)$$

Here $\rho_w(\lambda)$ is water-leaving reflectance, and contains the useful information on water properties to be isolated from ρ_t through atmospheric correction (Gordon & Wang, 1994; Kevin George Ruddick *et al*., 2000; Siegel *et al*., 2000). The $t(\lambda)$ term is diffuse transmittance of the atmosphere, and is available through lookup tables. ρ_g represents reflectance from sun glint and whitecaps, and is ignored by using appropriate solar and viewing geometries (Wang & Bailey, 2001; Gordon & Wang, 1994; Wang & Bailey, 2001). Terms $\rho_r(\lambda)$, $\rho_a(\lambda)$, and $\rho_{ra}(\lambda)$ are reflectance from Rayleigh scattering, aerosols, and

the interactions between both, respectively. $\rho_r(\lambda)$ is accurately derived from lookup tables computed for different solar and viewing geometries, atmospheric pressure and wind speed (Wang, 2002). While Rayleigh scattering is easily defined, $\rho_a(\lambda) + \rho_{ra}(\lambda)$ are highly variable and cannot be predicted beforehand from auxiliary data.

The Gordon and Wang (1994) approach solves Equation 1 by quantifying aerosol reflectance, $\rho_a(\lambda)$, at two bands where water-leaving reflectance is assumed to be zero ($t(\lambda)\rho_w(\lambda) \approx 0$) due to high water absorption. One band is used to evaluate magnitude of aerosol contribution and a second is required for evaluating wavelength dependence (Gordon and Wang, 1994). The OBPG approach uses two NIR bands centered at 748nm and 869nm (Werdell, Franz, & Bailey, 2010) where pure water absorptions are approximately 2 - 5 m^{-1}, respectively (Shi & Wang, 2009). Any detected signal at these bands is assumed to correspond to atmospheric contributions to total signal. The effects of aerosols and Rayleigh-aerosol interactions, $\rho_a(\lambda) + \rho_{ra}(\lambda)$, are then estimated at the two NIR bands from sensor-measured radiances, computed Rayleigh scattering, and estimated whitecap contributions. The ρ_{ra} is zero where radiation is only scattered once by either aerosols or air. This is true for low aerosol optical thicknesses (sensor near nadir), therefore in Equation 1 $\rho_a(\lambda) + \rho_{ra}(\lambda)$ are replaced by aerosol single scattering reflectance, $\rho_{as}(\lambda)$ (Gordon & Castaño, 1989; Gordon & Voss, 1999):

$$\rho_{t(\lambda)=}\rho_{as}(\lambda) + t(\lambda)\rho_w(\lambda) \quad (2)$$

Where:

$$\rho_{as}(\lambda) = \frac{\omega_a \tau_a(\lambda) P_a(\theta,\theta_0,\lambda)}{4cos\theta \cos\theta_0} \quad (3)$$

ω_a is aerosol single scattering albedo, τ_a is aerosol optical thickness, and ρ_a is the aerosol scattering phase function, α, or the amount of light scattered in each direction. The estimated effects of aerosols at the two NIR bands is then extrapolated and removed in the visible spectra. This is achieved through a process of aerosol model selection for each image pixel by evaluating the atmospheric correction parameter ε(λi, λj), defined as:

$$\varepsilon(\lambda i,\lambda j) = \frac{\rho as(\lambda i)}{\rho as(\lambda j)} = \frac{\omega a(\lambda i)\tau a(\lambda i) Pa(\theta,\theta 0,\lambda i)}{\omega a(\lambda j)\tau a(\lambda j) Pa(\theta,\theta 0,\lambda j)} \quad (4)$$

where (λi, λj) represent the shorter and longer wavelength, respectively. The value of ε(λi, λj) characterizes the spectral variation of aerosol extinction coefficient, which includes the aerosol optical thickness, single scattering albedo, and aerosol phase function. It is then used to retrieve appropriate atmospheric optical properties in the visible wavelengths through predefined lookup tables comprised of 80 aerosol models (Ahmad *et al.*, 2010; Shettle & Fenn, 1979). These models depend on 8 relative humidity values (RH), and fine particle fraction in aerosol size distributions (ƒ, 10 values). Typical marine ε values are ≈ 1, while in an extreme case of an atmosphere with no aerosol ε ≈ 2.2 (Gordon & Wang, 1994; Stumpf, Arnone, Gould, Martinolich, & Ransibrahmanakul, 2003). The aerosol model selection works by varying ƒ of the two bounding aerosol models with closest ε to the observed. This process is done with two families of aerosol models comprised of RH closest to the one observed from ancillary National Centers for Environment Prediction (NCEP) (Mélin, Zibordi, Carlund, Holben, & Stefan, 2013). The

final determined aerosol contribution is a weighted average of the four identified models. The NIR contributions of water-leaving reflectance are handled via an iterative process before ε(λi, λj) selection as described below.

2.1.1 Standard NASA algorithm 2-Band iterative NIR correction (Method 1)

The traditional black-pixel assumption (BPA) generally fails in waters with high particulate backscattering (algal and suspended sediments) (Goyens, Jamet, & Schroeder, 2013; Jamet *et al*., 2011; Siegel *et al*., 2000). If the NIR reflectances are non-negligible two errors in the determined aerosol contributions occur. First, if the longer wavelength $R_{rs}(\lambda)$(869nm) in Eq. (4) is non negligible, then aerosol contributions are overestimated resulting in overcorrection at all bands producing lower $\rho_w(\lambda)$. Secondly, if the shorter NIR band, $R_{rs}(\lambda)$(748nm), is non negligible, then the aerosol type will be mischaracterized (Stumpf *et al*., 2003). To address pixels that failed the black pixel approach, the OBPG developed an iterative bio-optical model to estimate $R_{rs}(\lambda)$(NIR) for the third SeaWiFS reprocessing (R2000.0) (Siegel *et al*., 2000). This reprocessing approach assumed that the backscattering signal covaries with *chla*, and used GW94 model (Gordon and Wang, 1994) to solve for backscattering. This model relaxed the BPA and was initiated by running the standard BPA and ignoring any $R_{rs}(\lambda)$(NIR) > 0 sr^{-1} to estimate *chla* using visible bands. Known relationships between chlorophyll concentration and theoretical particulate backscattering are used to quantify and remove the contributions in the NIR from TOA. The whole process was iterated until *chla* estimates converged to estimated inputs. However, due to unreasonably high initial values of *chla* and non-universal covariance of

chla and backscattering, b_{bp}(NIR) is generally overestimated leading to overcorrections (Bailey, Franz, & Werdell, 2010).

The current OBPG standard algorithm, originally developed by Stumpf *et al*., (2003) (R2002.0), and updated by Bailey, Franz, & Werdell, (2010) (R2009.0) is based on the R2000.0 approach, however the iterative approach considers convergence to NIR reflectance opposed to the convergence to *chla* as in the R2000.0 to quantify the particulates contributions in the R_{rs}(NIR). Once the difference between estimated R_{rs}(NIR) and the previous R_{rs}(NIR) is lower than a certain threshold, the iteration process stops and the atmospheric model is selected (Eq. 4) to define the new the R_{rs} in the visible wavelengths. An updated bio-optical model, which considers absorption and backscattering at a reference and NIR wavelengths is a key component of this approach:

$$R_{rs}(\lambda_r) = R_{rs}(\lambda_0)\frac{a_{tot}(\lambda_0)}{a_{tot}(\lambda_r)}\, r_{bb}(\lambda_r\lambda_j), \tag{5}$$

Where, the backscatter relationship, $r_{bb}(\lambda_r\lambda_j)$, is:

$$r_{bb}(\lambda_r\lambda_j) = \left[\frac{b_b(\lambda_r)}{b_b(\lambda_j)}\right]^{\eta}, \tag{6}$$

and η is the empirically derived constant (Lee, Arnone, Hu, Werdell, & Lubac, 2010):

$$\eta = 2.0 * \left[1 - 1.2e^{\left(-0.9*\frac{\mathrm{Rrs}(443)}{\mathrm{Rrs}(551)}\right)}\right] \tag{7}$$

The total absorption, a_{tot}, in Eq. (5) is the sum of absorption coefficients from water, a_w, phytoplankton, a_{ph}, and dissolved and detrital matter, a_{dg} (Stumpf *et al*., 2003). The latter two are assumed to contribute negligibly to $a_{tot}(\lambda_r)$ in the NIR (748nm and 869nm)

bands, while a_w is determined through predefined lookup tables. For the reference band however, all three terms are determined. $a_{ph}(\lambda)$ and a_{dg} determination is based on single *chla*-based empirical relationship that determines a(670nm) (Bailey *et al*., 2010). The equation was derived using the OBPG NOMAD dataset (Werdell & Bailey, 2005), and is expressed as (Bailey *et al*., 2010):

$$a(670) = e^{(\ln(chla)*0.9389-3.7589)} + a_w(670) \quad (8)$$

The iteration scheme first assumes BPA(NIR) to back-calculate initial estimates of the reference wavelength in the visible, used in turn to calculate a new estimate of R_{RS}(NIR). This process is iterated up to ten times or to convergence (R_{rs} changes by less than 2%). Once the $\rho_w(\lambda)$ contribution is removed from the top of atmosphere, model selection based on Eq.4 is performed.

2.1.2 2-Band iterative SWIR correction (Method 2)

Wang (2007) first proposed the two band method using the SWIR bands for aerosol characterization in highly turbid waters where the NIR method fails. The SWIR method is performed the same way as the standard NIR, however, uses the 1240 and 2130nm bands and assumes light is completely absorbed by the ocean at 2130nm. This assumption is generally valid as water absorption is more than two-orders of magnitude larger at 2130nm than in the NIR (Hale & Querry, 1973). Previous studies that have focused on highly turbid inland and coastal waters have shown that this method can be useful for deriving realistic reflectance values, when the NIR approach fails (Sanwlani, Chauhan, & Navalgund, 2011; Shi & Wang, 2009;Wang, Son, Zhang, & Shi, 2013b). A potential

drawback to this method is the low signal-to-noise (SNR) values in SWIR bands. Low SNR produces broad, frequency distributions relative to NIR bands (Bailey *et al*., 2010). For this reason the SWIR method performs worse in non-turbid and open ocean waters (Wang, Son, & Shi, 2009b). The SWIR corrected product represents an intermediary step between the NIR and the final method under investigation (MUMM+SWIR).

2.1.3 MUMM+SWIR approach (Method 3)

The final method was first proposed and developed for SeaWiFS and uses a non-iterative approach whereby the assumptions of zero water-leaving reflectance in the NIR bands are replaced by the assumptions of spatial homogeneity of aerosol type (Ångstrom coefficient and τ_a) in the region of interest (Ruddick *et al*., 2000). This method is commonly referred to as the MUMM (Management Unit of the North Sea Mathematical Model) model. The method requires *a priori* knowledge of normalized reflectance ratios for water ($\rho_w N$), $\alpha(\lambda_{NIR1}, \lambda_{NIR2})$, and aerosol, $\varepsilon(\lambda_{NIR1}, \lambda_{NIR2})$, between two NIR bands (Ruddick *et al*., 2000).

$$\alpha(\lambda \mathrm{NIR1}, \lambda \mathrm{NIR2}) = \frac{\rho_w N(\lambda \mathrm{NIR1})}{\rho_w N(\lambda \mathrm{NIR2})} \tag{9}$$

$$\varepsilon(\lambda \mathrm{NIR1}, \lambda \mathrm{NIR2}) = \frac{\rho_A(\lambda \mathrm{NIR1})}{\rho_A(\lambda \mathrm{NIR2})} \tag{10}$$

When both $\alpha(\lambda_{NIR1}, \lambda_{NIR2})$ and $\varepsilon(\lambda_{NIR1}, \lambda_{NIR2})$ are known, the two above equations can be used to separate the reflectance from aerosols and water in Rayleigh-corrected

reflectance (Ruddick *et al*., 2000). Successful results from the MUMM method requires the accurate definition of $\alpha(\lambda\mathrm{NIR1}, \lambda\mathrm{NIR2})$ and $\varepsilon(\lambda\mathrm{NIR1}, \lambda\mathrm{NIR2})$ representing clear waters in the image to apply to turbid waters in the image. However, this algorithm can still underestimate the water-leaving reflectance, $\rho_{w,}$ in extremely turbid water conditions since the ratio of ρ_w at two NIR wavelengths, α, is changed with increased concentration of suspended particles (Lee, Ahn, Park, & Kim, 2013).

Presence of high concentrations of suspended particulates in the central SoG makes identification of NIR optically clear waters difficult. For this reason, the spatially averaged NIR aerosol properties, ε(748,869), were estimated from previous SWIR-corrected images according to Method 2. Adjacency effect from land, however, can make these bands problematic for atmospheric correction of coastal water bodies such as the SoG. To limit potential adjacency effects and possible effects of reflectance from turbid water, the mean ε(748,869) was derived from a region farther from the coastline and away from known areas of high turbidity as identified in Loos & Costa, (2010) (Figure 2). To further limit any potential effects of low SNR or variability, a 5x5 ROI was used to produce an average α and ε for input into atmospheric correction. While Komick, (2007) indicated generally favorable results when applying these methods to MODIS images, his subsequent analyzed image database was constrained to a few images representing only spring conditions, and therefore may not be effective for all seasons.

2.2 Ocean Color 3 MODIS (OC3M) Chlorophyll algorithm

Chlorophyll concentrations were derived from all atmospherically corrected images using the standard OBPG chlorophyll algorithm, Ocean Color 3 MODIS (Mcclain *et al*., 2000).

OC3M is an empirically derived algorithm developed as an extension of the OC4 and OC2 SeaWiFS algorithms adapted for the specific spectral bands of the MODIS sensor. It was statistically derived from chlorophyll concentrations ranging from 0.0008 to 90mg m^{-3}, with the majority of concentrations ranging between 0.08 to 3 mg m^{-3} using the SeaWiFS Bio-optical Algorithm Mini-Workshop (SeaBAM) dataset *(O'Reilly et al.* 2000). The OC3M algorithm is defined as:

$$\mathrm{Log10}[chla] = a_o + a_1 X + a_2 X^2 + a_3 X^3 + a_4 X^4 \quad (11)$$

where

$$X = log\left[\frac{\max(R_{rs}(443), R_{rs}(489))}{R_{rs}(547)}\right] \quad (12)$$

And the coefficients a_0,a_1,a_2,a_3,a_4 are 0.2424, -2.7423, 1.8017, 0.0015, and -1.2280, respectively. Here, the larger observed value of R_{rs} (443) and R_{rs} (489) nm bands is chosen as dividend to the R_{rs} (547) value in calculating reflectance ratio X.

Chapter 3 - Methods

The following section provides an overview of the physical dimensions and biophysical conditions of Strait of Georgia during the sampling period. This is followed by a description of *in situ* radiometric and biophysical sampling procedures, as well as imagery processing (§ 3.2), and statistical analysis methods in section 3.3. Section 3.4 provides methods on the compiled time-series analysis, including the binning technique used to aggregate data, followed by phenology metrics (§ 3.5), and hierarchical clustering analysis (§ 3.6).

3.1 Study Area

The Strait of Georgia (SoG) is a deep estuarine-forced temperate sea located on the south west coast of British Columbia, Canada (Figure 1)(Pawlowicz, Riche, & Halverson, 2007). The SoG is approximately 200 km long and 28 km wide having an average depth of 150m, extending to 400m in the central region (Thomson, 1981). It is connected to the Pacific Ocean by outlets at its north and south extremities. Water movement is mostly south flowing estuarine circulation driven by freshwater surface outflow exchanging with subsurface saline and nutrient rich waters from the Pacific Ocean (Li, Gargett, & Denman, 2000). Significant tidal mixing occurs in the southern boundaries through the Haro Strait and southern Gulf Islands in part moderated by semidiurnal tides. Currents in these areas are as high as $1ms^{-1}$, and decrease northward (Halverson & Pawlowicz, 2008; Masson & Cummins, 2004). Tidal mixing produces near homogenous waters during the winter for

the south, and is most stratified in Central and Northern waters with increased water residence times (Waldichuk, 1957).

Water movement in combination with biological and riverine inputs leads to more optically complex surface waters in the central and southern Strait where regions of high particulate backscattering is present (Hoff *et al*., 1997; Loos & Costa, 2010). The greatest light attenuation from suspended matter occurs at surface waters, particularly in the spring and summer (Johannessen, Masson, & Macdonald, 2006; Loos & Costa, 2010), where high loads of inorganic particles enter the Strait as a riverine plume. However, Sutton *et al*. (2013) demonstrated spatial variability in suspended matter, where a larger proportion of organic material in the Northern SoG is derived from phytoplankton than the Southern, Fraser River dominated region.

Biologically, the SoG exhibits typical temperate diatom-dominated spring blooms followed by weaker fall bloom events (Sprules, Collins, Allen, & Pawlowicz, 2009), where primary assemblages are *Thalassiosira* spp., *Skeletonema costatum*, and *Chaetoceros* spp. (Harrison, Fulton, Taylor, & Parsons, 1983; Louis, 1997). Timing of spring bloom is observed to vary interannually by 6 weeks from late February to mid-April (Allen & Wolfe, 2013; Gower *et al*., 2013; Sprules *et al*., 2009), mediated by light availability (Allen & Wolfe, 2013), wind events controlling the mixed-layer depth and timing of outflow from the spring freshet (Sprules *et al.*, 2009). Dinoflagellates are the second most abundant group of phytoplankton; often the dominating total biomass in summer and early fall (Pospelova, Esenkulova, Johannessen, O'Brien, & Macdonald, 2010), when productivity is

nitrate limited (Yin *et al.*, 1997). During winter, nutrients tend to be above limitation level creating a situation where phytoplankton growth is light limited (Sprules *et al.*, 2009).

A key feature of the SoG is inputs from the Fraser River which discharges ~140km^3 of fresh water and ~20 megatons of associated sediment annually (Yunker & Macdonald, 2003), providing up to 80% of the freshwater for the SoG (Johannessen, Macdonald, & Paton, 2003; Stronach, 1981). These inputs drive circulation and form a brackish surface plume that dominates southern and central portions of the SoG (Stronach, 1981). Fraser River also dominates the supply of allochthonous chromophoric dissolved organic matter (CDOM) to the SoG. However, there is some variation locally within the SoG in which CDOM covaries with the onset and dispersal of localized phytoplankton blooms, often hourly (Twardowski & Donaghay, 2001). CDOM may play a larger role in the total light attenuation in northern waters, relative to total suspended matter (Loos & Costa, 2010).

Another important SoG property to consider is the variation of above-water optical contributions. In general, the aerosol optical depth distribution in the northeastern Pacific is due to biogenic and sea salt sulfate emissions (Bokoye *et al*., 2001). Sulfate aerosols scatter radiation without significant absorption and are a product of phytoplankton dimethylsulphide reacting with available SO_2. In the SoG, significant loads of aerosols are emitted from major urban sites including Nanaimo, Victoria and Vancouver in the southern and central extents, and can create a plume over the SoG (Hoff *et al*., 1997; Pawlowicz *et al*., 2007; Vingarzan & Thomson, 2004). These tend to be carbonaceous, and can be roughly divided into either ‘organic’ or ‘black’ groups. While both are emitted from

biomass and fossil fuel combustion, organics tend to scatter while black aerosols strongly absorb radiation and are hydrophobic (Takemura *et al*., 2000). Absorbing aerosols are not easily differentiated from non-absorbing aerosols in current atmospheric correction algorithms, which can lead to increased negative bias in the derived short wavelength $R_{rs}(\lambda)$ (Franz, Bailey, Meister, & Werdell, 2012).

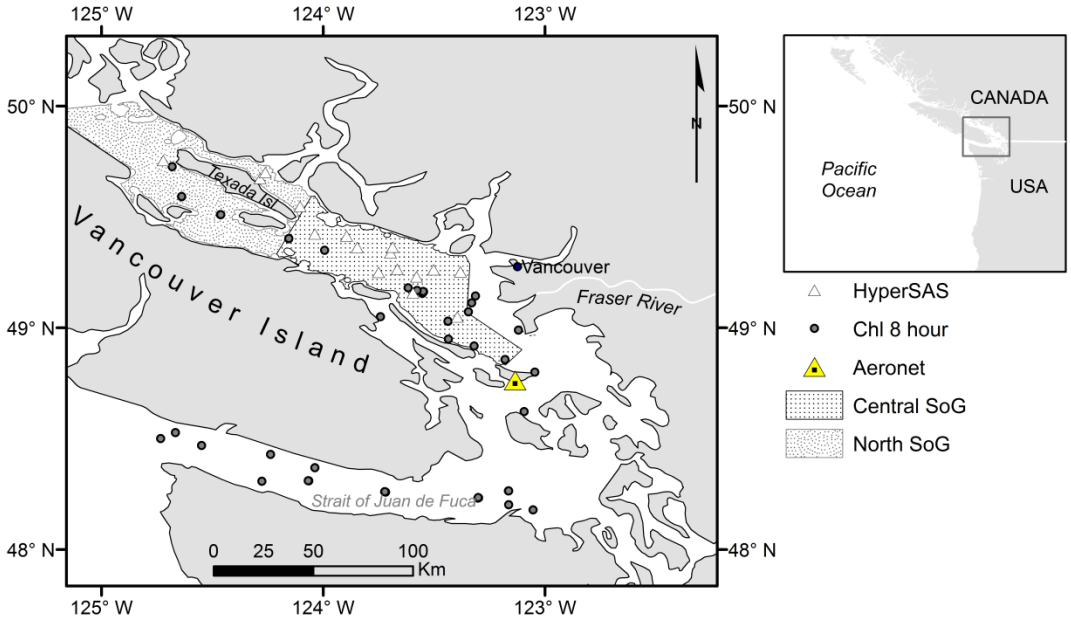

Figure 1. Strait of Georgia study area with in *situ* sampling stations used in this study. Chlorophyll-*a in situ* sampling stations of 2012 and 2013 are represented by grey points; HyperSAS acquisition sites (2012) are represented by triangles; AERONET site is represented by large triangle. North and Central regions adapted from Thomson, (1981).

3.2 Dataset

3.2.1 *In Situ* Radiometric Measurements

Two sets of *in situ* radiometric data were used to estimate uncertainties of remote sensing products from the three atmospheric corrections. The first dataset is comprised of AOT and Ångstrom exponent (Å) from the Aerosol Robotic Network (AERONET) (Holben *et al*., 1998). AERONET is a global network of surface-based sun-photometers providing a long-term, near real-time database of columnar integrated aerosol optical properties (Holben *et al*., 1998). There is one AERONET site in the SoG, located on the small (31 km^2) and sparsely populated Saturna Island that is maintained by AEROCAN (Bokoye *et al*., 2001). An advantage to this location is its central position in the SoG, adjacent to more open water for image comparison, in contrast to bordering Gulf Island locations. Only cloud-screened and quality controlled (level 2.0) data were downloaded and used for this study. Spectral τ_a for the channels corresponding to 440, 675, 870 nm, and the Ångstrom exponent, Å(440nm/870nm), were extracted to matchup with MODIS-derived data. The Ångstrom exponent is computed as the linear regression slope value of the log-transformed τ_a as a function of λ in the 440-870nm range, expressed as (Ångström, 1964; Schuster, Dubovik, & Holben, 2006):

$$\text{Å}(\lambda_1, \lambda_2) = \frac{-log\left(\frac{\tau_a(\lambda_1)}{\tau_a(\lambda_2)}\right)}{log\left(\frac{\lambda_1}{\lambda_2}\right)} \tag{13}$$

Where λ_1, λ_2 represents 440 and 870nm, respectively. It is commonly used to characterize the wavelength dependence of τ_a, and provides basic information of prevailing aerosol

size as spectral shape is directly related to particle size (Eck *et al*., 1999). Values of Å less than 1 indicate aerosols typically associated with dust and sea salts. Values greater than 2 indicate finer aerosols associated with urban influence of by-products of organic combustion (Ahmad *et al*., 2010).

The AERONET and MODIS matchup data are constrained by the land-based site location, and cannot completely geographically match satellite pixels. Therefore, satellite values were extracted from a 3x3 averaged pixel-box (Region of interest – ROI) to the south, centered on 48.7327° North, -123.1181° West; approximately 5km from the AERONET site, and away from direct influence of the Fraser River plume. The assumption is satellite derived values of an appropriately large adjacent ROI is indicative of *in situ* values for comparison. Expected uncertainty for τ_a in both visible and NIR regions is between 0.01-0.02 due to calibration limitations of AERONET field instruments (Eck *et al*., 1999; Zibordi, Berthon, Mélin, D'Alimonte & Kaitala, 2009). Since each aerosol model corresponds to a unique Ångstrom exponent value at $\tau_a(440{,}870nm)$ in the atmospheric correction data processing system (Wang, 2007), frequency distributions can be compared between *in situ* AERONET and MODIS-derived values to assess the ability of the defined model to characterize common atmospheric dimensions present in the SoG, as well as direct comparison to determine uncertainty of atmospheric corrections (Jamet *et al*., 2011; Mélin *et al*., 2013; More, *et al*., 2013)

The second set of radiometric data was comprised of *in situ* above-water $R_{rs}(\lambda)$ collected during cruises using the Satlantic Hyperspectral Surface Acquisition System (HyperSAS).

This system features sensors for quantifying sea surface radiance ($L_t(\lambda)$), sky radiance ($L_s(\lambda)$), and sky irradiance ($E_s(\lambda)$) at 136-channels in the 350-800nm range with an 8.5° field of view (FOV) for the L_t and L_s sensors. The system was bow-mounted at a height of approximately 6m from sea surface. An effort was made to maintain a consistent acquisition geometry, whereby the system was at 90°-120° azimuth from the sun, and the L_t and L_s sensors at 40° from nadir in opposite directions (Mobley, 1999). At each station, approximately 2 minutes of radiometric sampling were acquired, and spectra having the lowest 5% reflectance in the NIR (~780nm) were used to produce averaged reflectance spectra. This is a practical procedure to reduce erroneous spectra due to sun glint (Ahmed *et al*., 2012). Ancillary information on sea state and wind conditions was recorded and data were discarded for unsuitable ambient conditions. In order to directly compare results to derived imagery, the radiances were converted to above-water remote sensing reflectance according to Eq. 14-16 (Mobley, 1999; Ruddick, De Cauwer, Park & Moore, 2006):

$$R_{rs}(\lambda) = \frac{L_t(\lambda) - \rho_{sky} L_s(\lambda)}{E_s(\lambda)}, \tag{14}$$

$$\rho_{sky} = 0.0256 + 0.00039W + 0.000034W^2, when \frac{L_s(750)}{E_s(750)} < 0.05 \tag{15}$$

$$\rho_{sky} = 0.0256, when \frac{L_s(750)}{E_s(750)} \geq 0.05 \tag{16}$$

Where ρ_{sky} represents reflected sky radiance off of the water surface, being dependant on wind speed, W, and the fraction of cloud cover in the sky radiance measurements identified by $L_s(750)/E_s\ (750)$. During clear sky conditions, where the ratio is < 0.05, the ρ_{sky} value is attributed to water surface roughness and associated bright reflections. In contrast, for overcast conditions (≥ 0.05), sky lighting is more diffuse resulting in ρ_{sky} being independent of glint (Mobley, 1999; Ruddick *et al.*, 2006).

For direct comparison to MODIS spectra, the final processing step was to convolve HyperSAS $R_{rs}(\lambda)$ data to MODIS bands using the MODIS Spectral Response Function available from the OBPG. A total of 194 spectra were acquired for this study including 15 spectra from Komick *et al*, (2008) that were acquired and processed using the same methods (Table 1).

3.2.2 *In Situ* biogeochemical data

In situ chlorophyll surface concentrations from two separate datasets were acquired for imagery validation (Table 1). The first dataset corresponds to data from water samples collected aboard the CCGS W.E. Ricker during the summer and fall of 2012. All chlorophyll samples (n=192) were collected at an approximate three meter depth using the continuous shipboard laboratory pump. Triplicate 1L samples were filtered using 0.7 µm Whatman GF/F glass fiber filters following the Ocean Optics protocols (Mueller *et al*., 2003). Samples were stored at -25°C during the cruise and then transferred to a -80°C facility at the University of Victoria until pigment extraction. *Chla* pigment concentrations were determined using a Dionex high phase liquid chromatography (HPLC) system

equipped with a PDA-100 photodiode array detector and DHI pigment standards (Arar, 1997). Ancillary data collected at each station includes total suspended material (TSM) following the gravimetric method outlined in Mueller (2003), and absorption by chromophoric dissolved organic material (a_{CDOM}). Absorbance measurements were defined using distilled water as a reference standard and were corrected by subtracting average values between 650 and 875nm due to negligible expected a_{CDOM} in this range. Final values were converted to $a_{\mathrm{CDOM}}(\lambda)$ using Beer-Lambert's Law (Hoge, Vodacek, & Blough, 1993; Loos & Costa, 2010):

$$a_{\mathrm{CDOM}}(\lambda) = 2.303\,\frac{A(\lambda)}{l}, \qquad (17)$$

where $A(\lambda)$ is measured absorbance at given wavelength, and l is cuvette length in meters.

The second *in situ* chlorophyll dataset of surface chlorophyll concentrations (n=618) was provided by the Institute of Ocean Sciences, Fisheries and Oceans Canada, as part of their Data repository (http://www.pac.dfo-mpo.gc.ca/science/oceans/data-donnees/index-eng.html) for water property profiles (DFO, 2014). These data were collected from predetermined Rosette stations and *chla* concentrations were determined through a Turner 10AU fluorometer calibrated to Sigma pigment standards (Holm-Hansen, Lorenzen, Holmes, & Strickland, 1965). Only surface sample (≤3.0m) depths were included for analysis to be consistent with the Ricker Cruise data.

Table 1. Cruise data used in this study and associated sources

Sampling Institution	Geographic Area	Vessel	Periods	N Stations	Data
Institute of Ocean Sciences	Strait of Georgia	CCGS Vector	Intermittent, May 2002-July 2013	618	Chlα
	Juan de Fuca Strait		July 2013		
	Johnstone Strait				
Pacific Biological Station	Strait of Georgia	CCGS W.E. Ricker	June/July 2012	192	Chlα
	Juan de Fuca Strait		September 2012	194	$R_{Rs}(\lambda)$
			June/July 2013	238	TSM
			September/October 2013	163	CDOM
Komick,Costa & Gower (2009)	Strait of Georgia	R/V John Strickland	April 25-28 2006	15	$R_{Rs}(\lambda)$
			July 12-17 2006		

3.2.3 Biophysical conditions during sampling period

There was a range of conditions of the SoG biophysical properties during the sampling periods. The central SoG exhibited significant influence from the Fraser River plume with higher TSM concentrations (10.93-26.6 mg L^{-1}) and relatively greater a_{CDOM}(443nm) (1.09-1.73 m^{-1}) when compared to northern waters which show lower TSM concentrations (1.49-3.84 mg L^{-1}) and $a_{\mathrm{CDOM}}(\lambda 443\mathrm{nm})$(0.14-1.16 m^{-1}). Biophysical data-points spatially interpolated to produce a map using Inverse distance weighting (0.5 power) indicate the southern half of the Central region dominated by higher TSM with a distinct gradient moving northward (Figure 2). The range of TSM found in the Central plume-dominated regions are much higher than open ocean conditions and are consistent with previous studies of the area (Johannessen *et al*., 2006; Komick *et al*., 2009; Loos & Costa, 2010).

In contrast, elevated levels of $a_{\mathrm{CDOM}}(\lambda 443\mathrm{nm})$ are not isolated to areas under influence of the Fraser River plume, and extend throughout the northern region surrounding Texada Island. The average $a_{\mathrm{CDOM}}(\lambda 443\mathrm{nm})$ in the Strait is equal to 0.47m^{-1} ,and

indicative of estuarine systems (Keith, Yoder, & Freeman, 2002; Zhu, Shen, & Hong, 2010). The disparity of spatial distributions between TSM and CDOM suggest that CDOM production in the northern waters is most likely autochthonous, or is more easily transported from the Fraser River plume by currents when compared to TSM.

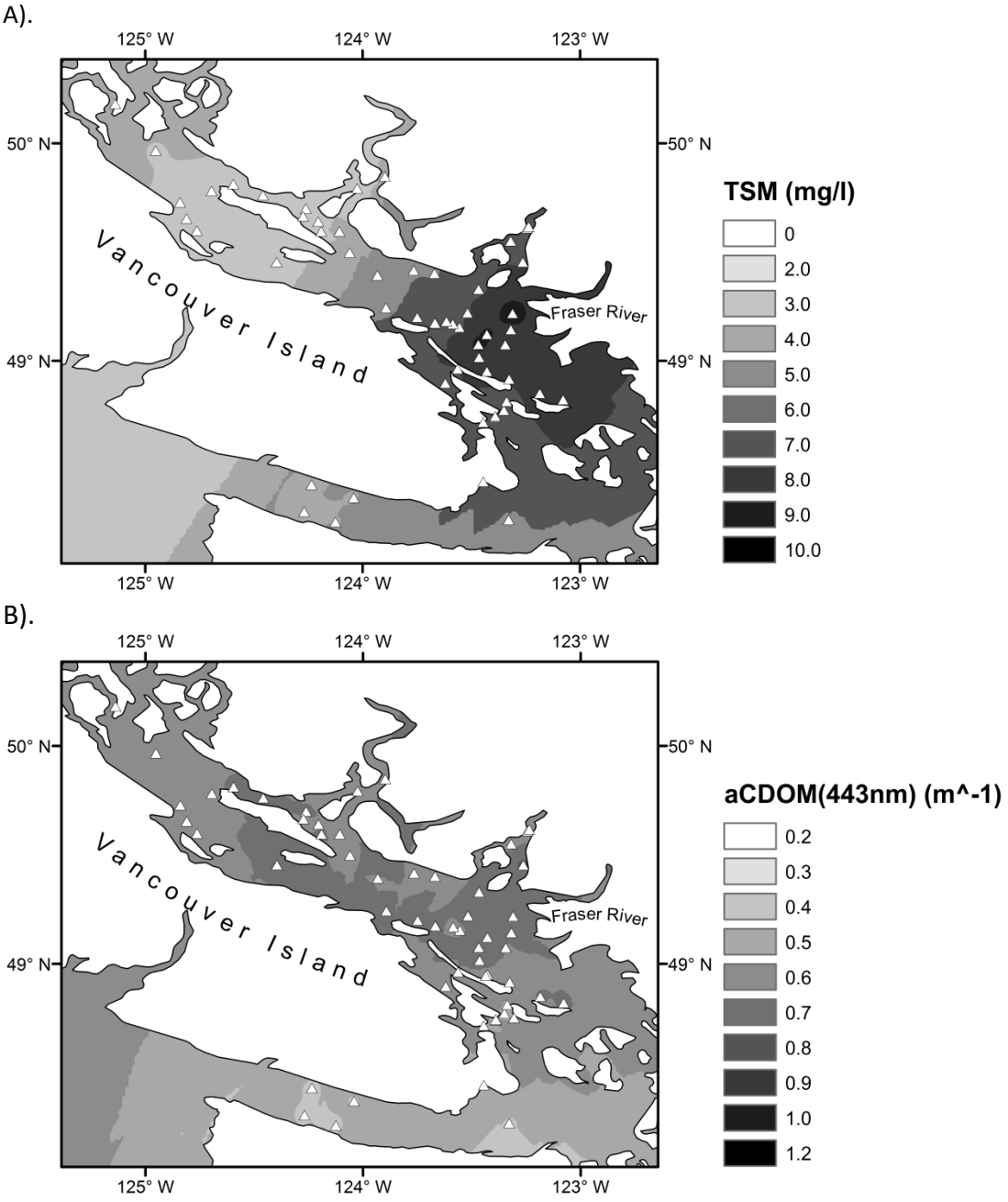

Figure 2. Spatial distribution of A). TSM and B). *aCDOM*(443) during the CCGS Ricker cruises (Table 1.).

In situ chlorophyll values collected during sampling covered a wide from ~0.1 to 45.0 mg m^3 with an average of 4.4 mg m^3. The highest levels of *chla* occurred in the central Gulf Islands, and the Malaspina Strait (28.0-45.0 mg m^{-3}), while the lowest (0.6 – 1.5 mg m^{-3}) were observed in Howe Sound and the Strait of Juan de Fuca.

3.2.3 MODIS Imagery processing

All available Level-1A files of the SoG were acquired from the OBPG. The time-series spanned from June 2002 through June 2014 at ~1 km^2 nadir spatial resolution. Of all available L1A files for this period, 3396 were evaluated to potentially contain pixel information for the study area and were selected for further processing. The L2GEN program in the SeaWiFS Data Analysis System 6.4 (SeaDAS) was used to generate the standard Level-2 files (NIR, 'method 1') containing $\rho_w(\lambda)$, spectral aerosol optical thickness and Ångstrom exponents. These files are identical to standard products distributed by the OBPG for research, with the exception of added products listed.

For SWIR processing ('method 2'), the NIR parameter files were duplicated and the 1240nm and 2130nm bands were substituted for the standard 748nm and 869nm epsilon calculation in Eq. 4. The L2GEN program was rerun for the time-series with the new parameters to produce a second dataset consisting of SWIR-corrected imagery.

For MUMM+SWIR approach ('method 3'), the SWIR corrected imagery from 'Method 2' was used as an initial input. The NIR radiances from method 2 were used for the critical step in the MUMM+SWIR method for retrieving Epsilon and Gamma values in Eq. 9-10.

Epsilon and gamma were characterized using a 5x5 sample pixel-box located in more northern and open waters, away from the Fraser River, in order to minimize influence of turbidity as well as land contaminations causing poor signal to noise ratio in the larger wavelength bands. The box was centered at 49.404°N/-123.965°W with the average 5x5 pixel value recorded. For images with cloud contamination, the nearest clear location was used, and image flagged for quality control.

Following the atmospheric correction step, the OC3M chlorophyll algorithm was applied to corrected reflectance products resultant from each atmospheric method to produce chlorophyll products. Processing masks were used to exclude data with high solar zenith angle, high sensor zenith angle, land, and straylight. High solar and sensor zenith angles (>70°) can cause *chla* overestimation due to increased path length and ultimately, atmospheric correction failures (Ding & Gordon, 1994). Erroneously high *chla* (>60mg m^3), likely a result of straylight, were found to be present in our dataset during winter periods before masking. Straylight contamination is a result of light contamination from bright, adjacent pixels from clouds and land onto the relatively low radiance ocean pixels through atmospheric scattering leading to extremely high *chla* concentration values (Hooker *et al*., 2003; Werdell *et al*., 2009). Straylight is characterized by the sensors modelled point spread function (PSF), giving information of contribution from adjacent pixels (Franz *et al*., 2003). To account for this, we adopted a 3x3 pixel straylight flag mask around high-radiance pixels, which captures 0.997 of the intensity of the theoretical PSF (Meister *et al*., 2012). The 3x3 mask was found to conserve good quality data, while eliminating sharply different reflectance values present near cloud and land. A final step in the

exclusion criteria, in part based on project results described below, excludes any remaining pixels with negative reflectance values in the blue wavelength bands, due to obvious atmospheric correction failure.

3.3 Method validation

3.3.1. Validation dataset

Validations of the respective atmospheric corrections and the OC3M algorithm retrievals were performed using *in situ* radiometric data and *chla, respectively*, following a matchup workflow procedure (Figure 3). The validation procedure consisted of three main components. The first component compared the Ångstrom exponent and aerosol optical thickness at 443, 679, and 869nm aerosol properties, as explained below.

For the matchup exercise, all AERONET data coinciding with the time of imagery acquisition (2002-2014) within 15 minutes temporal bound was used. Satellite derived values were extracted from a 3x3 average pixel-box located slightly to the south of the AERONET site centered on 48.7327°, -123.1181°. Although previous research have suggests using a 5x5 km pixel-box as a compromise between SNR and effective MODIS spatial resolution (Bailey & Werdell, 2006; Werdell, Franz, Bailey, Harding Jr, & Feldman, 2007), a 3x3 km pixel-box was selected as our analysis indicated this to be an acceptable trade-off to increase number of viable match-ups in an area with persistent cloud flagging. The assumption in this process is a degree of spatial homogeneity of aerosol properties within the ROI area of 9km^2. The AERONET Ångstrom (443nm/869nm) and AOT (443nm, 679nm, 869nm) were retrieved and compared with MODIS-derived Ångstrom and AOTs for the different atmospheric correction processes.

The second component of the matchup workflow was to compare MODIS atmospheric corrected $R_{rs}(\lambda)$ to *in situ* HyperSAS $R_{rs}(\lambda)$ aiming to define the accuracy of respective atmospheric corrections. This was accomplished in two steps. The first step was to compare spectra of concurrent *in situ* HyperSAS and MODIS derived atmospheric corrected spectra to assess reflectance distribution trends. For this, imagery 3x3 box-averaged $R_{rs}(\lambda)$ were extracted at HyperSAS sampling locations. Matchups were restricted to a ±3 hour temporal difference. Only matchups with data for all methods were used for a direct comparison to HyperSAS $R_{rs}(\lambda)$ since the different approaches to atmospheric correction created disparate valid-pixel distributions for the same daily acquisitions. Out of the 194 HyperSAS spectra acquired, only 6 samples taken aboard the W.E. Ricker and 10 samples from the Komick, Costa, & Gower, (2009) dataset were available for direct comparison to imagery with the given constraints for a total of 16. By relaxing the need for completely coincident values between atmospheric correction methods, the total number of matchups to HyperSAS $R_{rs}(\lambda)$ data increased to maximum of 34 (Table 2).

A second step of the *in situ* spectra matchup analysis was reflectance comparison at each band. To accomplish this, linear regression of MODIS $R_{rs}(\lambda)$ to HyperSAS $R_{rs}(\lambda)$ was performed on any positive MODIS $R_{rs}(\lambda)$ correspondent to HyperSAS of the same band. Negative MODIS $R_{rs}(\lambda)$ were observed and result from potential atmospheric correction errors.

The third component of the matchup workflow was related to the accuracy of the derived chl*a* products. For this component we compared *in situ* and MODIS-derived chlorophyll concentrations. All MODIS-derived surface chlorophyll samples were extracted using a 3x3 km average pixel-box for the *chla* products derived from the three different atmospheric correction approaches. A temporal difference of ±8 hours between *in situ* and MODIS acquisition was used as a maximum realistic 'daily' comparison. We investigated efficacy of the methods to increased temporal differences at ±8, ±6, ±4, ±2, and ±1 hour intervals.

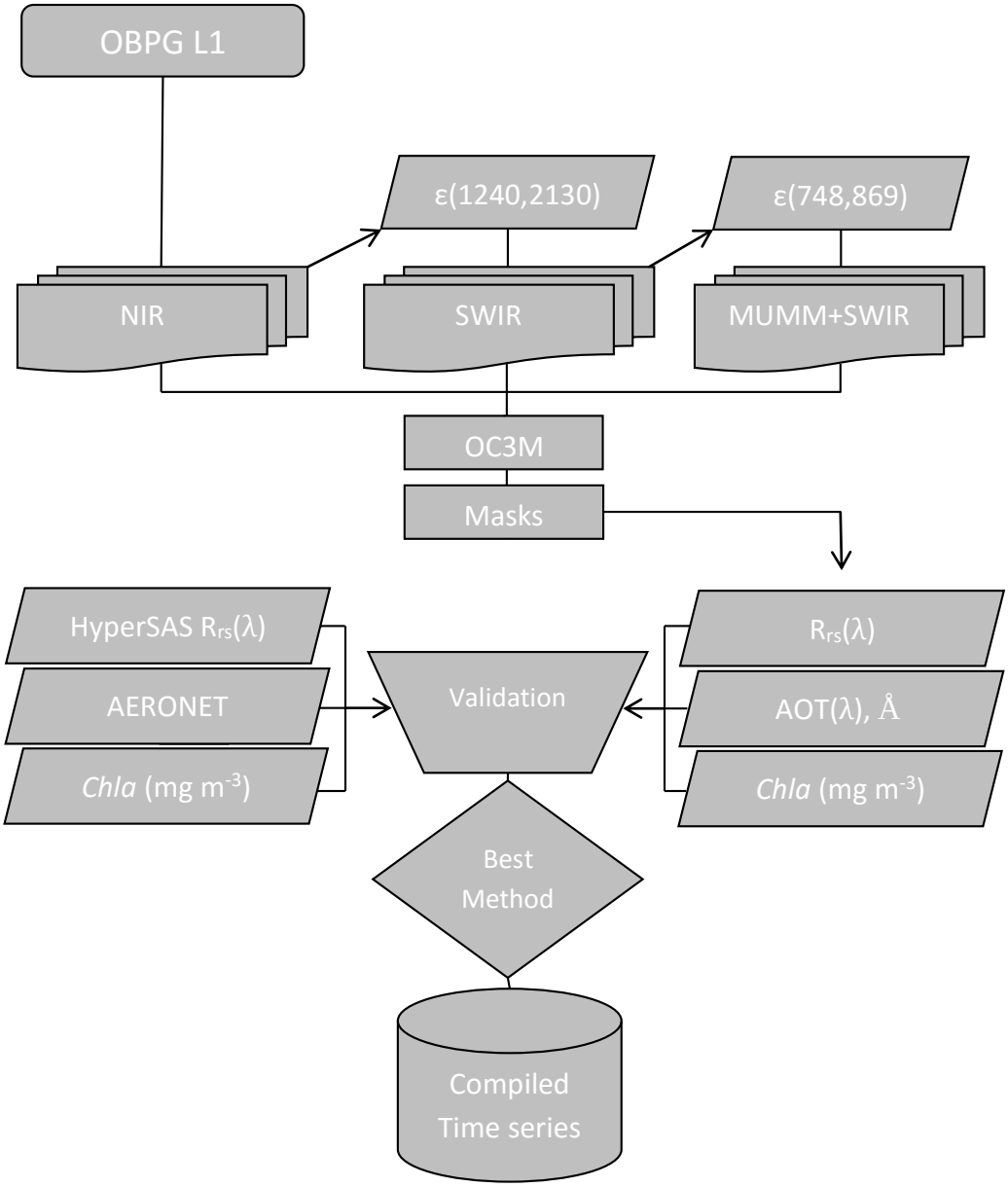

Figure 3. Data workflow for Imagery processing and validation to assess most appropriate method for time series creation.

3.3.2. Matchup Statistics

The match up statistical analysis considered the AERONET *vs.* satellite products, HyperSAS *vs.* satellite products, and *in situ* chl*a vs.* MODIS derived chl*a*. For all AERONET to satellite product matchups, the differences between AERONET (SITU) and Satellite (SAT) of variable X are expressed by the median absolute relative percent difference ($|\psi|$), median relative percent difference (ψ), median absolute difference ($|\delta|$), and median differences (δ) (Mélin *et al*., 2013):

$$|\psi| = 100 \times \text{median}\left(\frac{\left|X_i^{SAT} - X_i^{SITU}\right|}{X_i^{SITU}}\right)_{i=1,N} \quad (18)$$

$$\psi = 100 \times \text{median}\left(\frac{X_i^{SAT} - X_i^{SITU}}{X_i^{SITU}}\right)_{i=1,N} \quad (19)$$

$$|\delta| = \text{median}\left(X_i^{SAT} - X_i^{SITU}\right)_{i=1,N} \quad (20)$$

$|\psi|$ and ψ indicate % uncertainty and bias, while $|\delta|$ and δ are in uncertainty and bias in unit X, respectively. The median operator is chosen here to minimize outlier effects on calculated central tendency. These evaluative statistics were chosen for direct comparison to other work conducted globally that use the same statistics.

Linear regression analysis, and associated slopes and correlation coefficients, were carried out to evaluate performance of satellite to *in situ* HyperSAS and *chla* values. Median values were used for central tendencies for the relatively large AERONET dataset, however, the mean operator is used here to easily identify outliers in uncertainty and bias calculations in a much smaller dataset. Evaluative statistics used are the standard used in

the literature, the mean absolute percentage difference (APD), the mean relative percentage difference (RPD), and the root mean squared error (RMSE) between satellite-derived (X_{sat}) and *in situ* (X_{situ}) $R_{rs}(\lambda)$ and *chla* presented here as (Werdell *et al*., 2009; Williams *et al*., 2013):

$$APD = 100 \times \frac{1}{n}\sum_{n=1}^{N}\left|\frac{X_{SAT} - X_{SITU}}{X_{SITU}}\right|, \tag{21}$$

$$RPD = 100 \times \frac{1}{n}\sum_{n=1}^{N}\left(\frac{X_{SITU} - X_{SITU}}{X_{SITU}}\right), \tag{22}$$

$$RMSE = 100 \times \sqrt{\frac{1}{n}\sum_{n=1}^{N}(\frac{X_{SAT} - X_{SITU}}{X_{SITU}})^2} \tag{23}$$

Surface chlorophyll concentrations tend to be log-normally distributed (Campbell, Blaisdell, & Darzi, 1995), therefore, both MODIS and *in-situ chla* were log transformed and the root mean-square log-error ($RMSE_{log}$) were calculated by:

$$RMSE_{log} = \sqrt{\frac{1}{n}\sum_{n=1}^{N}\left(log_{10}(Chl_{SAT}) - log_{10}(Chl_{SITU})\right)^2} \tag{24}$$

For this study, statistical significance is defined at confidence intervals greater than the 95% level.

3.4 Time-series Analysis

3.4.1 Data binning

Results from the methods validation in section 3.3 were used to define the most accurate correction scheme and create a 12 year time-series (2002-2014) of MODIS *chla* products. Quality control flags and cloud cover, however, results in a lack of consistently available daily chlorophyll product for the SoG. To overcome this issue, daily images were transformed into level-3 'binned' data consisting of spatially and temporally averaged products (Campbell *et al*., 1995). The binning procedure, a component of the SeaDAS processing software, creates 8-day composite periods (MODIS 'week') using arithmetic mean of all available pixels, to create a grid of $1km^2$ values. The $1km^2$ binned grid is arranged in rows beginning at the South Pole. Each row begins at 180° longitude, circumscribing the earth at given latitude. The 8-day periods begin at the first day of the year for a total of 46 binned 'weeks'. Week 46 contains only five or six days, instead of eight. This arrangement makes it possible to directly compare weeks comprised of identical days-of-year (DOY) between different years. The benefit of binning data is a reduced-volume dataset with more continuous time series of increased spatial coverage with the assumption that the values used are representative of the weekly period. Temporal resolutions are reduced compared to level-2 data, however level-3 data are effective in depicting seasonal patterns at larger spatial scales (Campbell *et al*., 1995). All data were projected to BC Albers Equal Area Conic projection, using North American Datum 1983 (NAD83) to reduce areal distortion; a provincial standard for geodesy in British Columbia (British Columbia Gov., 2011).

3.4.2 Outlier Detection and Removal

Chla concentrations were extracted from polygon shapefiles (region of interest-ROI) for the North and Central region of the SoG (Figure 1) with a 1km buffer from shoreline. The North and Central delineations were based general biogeochemical differences between the regions (Section 3.1), and adapted from Figure 10.18 in Thomson (1981). The ROIs were designed to include the largest and most open portions of the SoG with the least potential of contamination from land adjacency and turbidity from the Fraser River. For this reason the waters within the Gulf Islands to the south and the northern Discovery Islands were excluded, as were data from the coastal inlets on the mainland. An additional buffer of the mudflats and most turbid regions of the Fraser River outfall designated by Komick, Costa, & Gower, (2009) was also used in this study.

A dataset of mean, median, standard deviation and pixel counts of chlorophyll concentrations and associated flags were extracted from all available binned composites (n=545) for the period of July 2002-June 2014. While composites were created for the 2002 year, MODIS data acquisition occurred after the spring period. Therefore, while processed, this data were excluded for the creation of the final time series shown in Figure 12.

Median values of SoG *chla* were chosen as a robust measure of central tendency over arithmetic mean for the binned-data extraction, as it is less susceptible to outliers (Dixon, 1953). This is a common practice when working with remotely-sensed chlorophyll data (Kahru & Mitchell, 2001; Werdell *et al*., 2009), due to persistent lognormal distributions (Campbell, 1995). Furthermore, in addition to the processing flag exclusion criteria

performed in daily-imagery creation (§ 3.2.3), a statistical outlier detection and removal process was performed as a final quality control measure. For instance, even though pixels with negative water reflectances in the blue band were removed, there remains the possibility of negligible reflectances stemming from CDOM absorption. This is typical of waters under strong influence of the Fraser River plume (Loos & Costa, 2010), which the OC3M empirically derived method cannot account for. This can lead to increased values of chlorophyll that manifest as incongruous zones in the final binned dataset.

The statistical outlier detection and removal process was based on the median absolute deviation from the median (MAD), a robust estimator of scale. MAD was used to identify a threshold of extreme values for removal. The MAD of pixels within an ROI is expressed as (Huber, 1981; Leys, *et al*., 2013):

$$MAD = b\, M_i\left(\left|x_i - M_j\left(x_j\right)\right|\right) \tag{25}$$

Where x_j is number of original pixel observations and M_j is the median of the ROI. The b constant takes the value 1.4826, and is a normalization factor assuming a Gaussian distribution. To account for Gaussian distributions, it was necessary that pixel data were log transformed for a more normal distribution to fit the assumption. Normality was assessed based on histograms of $\log_{chla}$ and normal quantile plots. Pixel rejection criteria were set at a moderately conservative 2 MAD, where any value falling outside this range was removed, and the final statistics were recalculated and plotted with a 1-MAD shaded error-bar indicating level of dispersion.

3.5 Definition of spring phenology metrics

The two general approaches to analyze time series and derive meaningful evaluative bloom metrics are time and time-frequency domain methods (Blondeau-Patissier *et al*., 2014). The first method, time domain, analyzes data in the same time-space of which data were observed, while the latter technique, time-frequency domain, deconstructs data to larger time scales and frequencies, and reconstructs the time series as a function of varying sinusoidal signals. For this study three time-domain and one time-frequency domain methods were evaluated to determine applicability for the spatial scales of the SoG. The first time-domain method consisted of fitting a shifted-gaussian model using non-linear least squares approach (Platt, Fuentes-Yaco, & Frank, 2003; Platt, White, Zhai, Sathyendranath, & Roy, 2009; Platt & Sathyendranath, 2008). The second time-domain method investigated was the TIMESAT program, which consists of a stepwise procedure using basis functions and least squares fit to a polynomial or Gaussian function (Jönsson & Eklundh, 2004).

The time-frequency method was the Harmonic Analysis of Time Series (HANTS), which constructs a Fourier series from the timeseries, while removing outliers and replacing them with Fourier-derived values (Roerink, Menenti, & Verhoef, 2000). Due to highly variable nature of chlorophyll concentrations within the SoG, all three methods were determined to be inappropriate to derive useful phenological indicators.

Siegel, Doney, & Yoder (2002) proposed defining spring bloom metrics based on reasonable thresholds of satellite derived *chla* for a given area, and associated annual

biomass. The authors suggest using a simple time domain method where the annual median chlorophyll concentration +5% to define the yearday of initiation, YD_{init}. Similarly, the maximum *chla* concentration occurring within the spring bloom period is defined as the yearday of maximum spring bloom, YD_{max}. A modified version of this method was applied by Schweigert *et al*. (2013) for the Strait of Georgia using the standard OBPG (NIR) dataset to investigate YD_{init} effects on herring abundance. For this study, this method is adapted to determine YD_{init}. The Central SoG YD_{init} is defined as the week where chlorophyll concentrations are over a threshold of 5mg m^{-3}, or when two consecutive weeks have measurements of the annual median plus 5%. The defined yearday is then the center of the week (midnight day 4), bounded by four days. Prior analysis indicated the north region exhibits a global median of approximately 2mg m^{-3} lower than the central region, therefore a threshold of 3mg m^{-3} was used here in lieu of 5mg m^{-3}. The definition of YD_{max} is unchanged, and is simply the center of the week exhibiting the highest concentration of chlorophyll for each respective region.

Given the dynamic nature of 8-day chlorophyll levels in the SoG, it is possible to have multiple spring-bloom events, where there are different periods of elevated *chla* in succession separated by lower levels as suggested in Schweigert *et al*. (2013). For instance, strong wind events can increase the surface mixing layer depth, disrupting any bloom (Yin *et al*., 1997). To address this, duration of the longest spring-bloom, YD_{dur}, is defined as the total duration of the longest period of elevated *chla* remaining above the YD_{init} threshold and being not interrupted by more than one week lower than YD_{init} *chla* concentrations. Depending on *chla* conditions, YD_{dur} can be independent of the YD_{init}

associated bloom. The inclusion of a week buffer period is to take into account the possibility of wind events that may temporarily increase the mixing depth layer while the system is not necessarily nutrient limited. Additionally, it is designed to address weeks of few or no data availability that may conceal *chla* concentrations for the specific region.

3.6 Hierarchical Clustering Analysis of Spring Seasons

Beyond investigating annual *chla* YD_{init}, duration, and amplitudes, and given the large variability of *chla* in the SoG, we further examined the similarity of regions between years. Agglomerative hierarchical clustering analysis (HCA) was conducted to identify similar and dissimilar interannual spring seasons; i.e., to define years that exhibit similar or dissimilar *chla* time series patterns. This is an exploratory method where observations, in this case weekly MODIS-derived *chla*, are statistically grouped in a way that similar cases (years) fall within the same cluster while dissimilar cases (years) are categorized into other clusters (Warren Liao, 2005). This method was originally developed for the study of genomics, however, the technique has been applied to several biological studies including clustering MODIS chlorophyll time-series and grouping environmental data (Abbas, Mansor, Pradhan, & Tan, 2012; Liao, 2005). This approach is relatively novel for ocean color usage, however, D'Ortenzio, Antoine, Martinez, & Ribera d'Alcalà (2012) grouped CZCS and SeaWiFS timeseries to develop maps of regions exhibiting similar phenologies using hierarchical clustering. By comparing clustering results from two 5 year time periods, the authors were able to record apparent shifts in regional cluster memberships. In our work, the time-series corresponds to MODIS-derived *chla* from 2003-2013 and encompasses the week of first available data that has not been flagged (week 7) to the

week of the spring season (week 23). 2002 and 2014 were excluded due to the sensor not being operable (spring 2002) and image processing extent (early spring 2014).

The process is initiated by calculating an all-to-all similarity matrix between time-series data. To calculate similarities, HCA requires the definition of a similarity method. The similarity distance is defined as $1-r$, in which (r) corresponds to the Pearson's correlation, or strength of correlation for two series, and therefore given perfect correlation between weeks the similarity distance results in a distance of zero. A similarity distance based on correlation is useful for our study because we are interested in magnitude of weekly *chla* in response to the same period (week) of different years. In contrast, other possible distance metrics, i.e. Euclidean distance, describe the sum of differences between recorded *chla* of the pairwise weeks, and are not effective to describe differences when chl*a* is lognormally distributed.

The second component of HCA is the definition of pairwise-distance linkage method to merge similar years into a cluster. For this study, simple arithmetic average between pairwise series was used to combine corresponding weeks of two years. A new matrix is then calculated with all remaining clusters and the process is iterated until only one cluster remains. Given an *m*-by-*n* data matrix X, which is treated as *m* (1-by-*n*) row vectors x_1, x_2, ..., x_m, the various Pearson's Correlation distances between the vector x_s and x_t are defined as follows (MathWorks, 2015):

$$d_{st} = 1 - \frac{(x_s - \bar{x}_s)(x_t - \bar{x}_t)'}{\sqrt{(x_s - \bar{x}_s)(x_s - \bar{x}_s)'}\sqrt{(x_t - \bar{x}_t)(x_t - \bar{x}_t)'}}, \text{ where} \quad (26)$$

$\bar{X}_s$=$\frac{1}{n}\sum_j x_{sj}$ and $\bar{X}_t = \frac{1}{n}\sum_j x_{tj}$ (27)

Here, the correlation reflects the degree of linear relationship similarity between two years considering weeks 7-23, or the spring patterns. This method is not sensitive to scaling differences and works well for absolute value data (D'haeseleer, 2005), however it does not account for possible non-linear relationships.

Chapter 4 - Results

4.1 Atmospheric correction evaluation

4.1.1 Ångstrom and Aerosol Optical Thickness

The results suggest that the dominant aerosol size distributions near Saturna Island were coarse mode aerosols (radii $\gtrsim$0.5µm) for the sampling period (2002-2012). 92% of AERONET aerosol Ångstrom values acquired in the area were less than 2.0, with the majority between the 1.2-1.6 (Figure 4). Due to the site proximity to the coast, this is an expected result and typical of dust and salts. Approximately 10% of all Å retrievals, however, were fine mode (Å >2, radii $\lesssim$ 0.5µm) indicating presence of strongly absorbing aerosols associated with urban pollution and associated biomass combustion (Eck *et al*., 1999; Fraser & Kaufman, 1985). The relative frequency of the AERONET Å(440/870nm) retrievals varied for the three atmospheric correction methods due to differences in the total number of matchup images available for each method (n = NIR (581), SWIR (620), MUMM+SWIR (618)).

The NIR method produced the most consistent Ångstrom frequencies when compared to AERONET, and was the only method that resolved exponents greater than 2.0 (Figures 4 & 5). Validation results (Table 2) indicate that the NIR exhibits the second lowest uncertainty when compared to AERONET with $|\psi|$ of 24.48% (0.29 Å) paired with the smallest bias, ψ, of -3.27% and lies close to the 1:1 line (Figure 5). The SWIR method tended to slightly over represent Ångstroms in the 1.6-2.0 range by ~20% while underestimating all other ranges. The SWIR validation shows similar uncertainty ($|\psi|$ =

24.33%) to NIR but exhibits high dispersion highlighted by large positive ψ of 11.65% (0.15Å), and no discernible 1:1 relationship. MUMM+SWIR exhibited similar results to the NIR at Ångstroms less than 0.8, but for Å between 0.8-1.2 it was over represented by 12%, and under characterized Ångstroms that were greater than 1.6. The MUMM+SWIR was the only method of the three to show a negative bias of 13.79%, while the absolute median percent relative difference was only ±0.03% larger than the other methods. There was high dispersion of match-up values, however, were generally located around the theoretical 1:1 relationship (Figure 5).

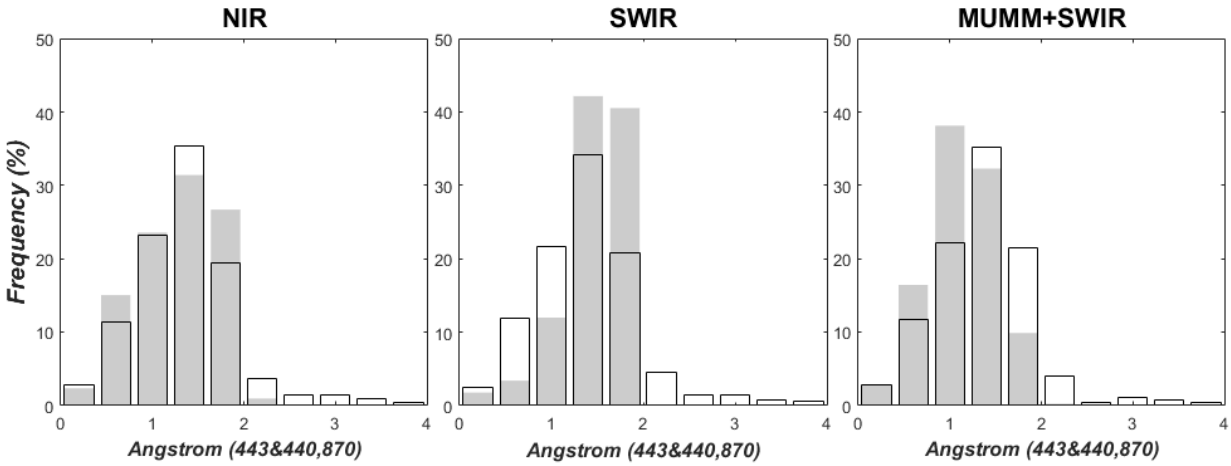

Figure 4. Histogram matchup (15 minute resolution) of Ångstrom exponent derived from three MODIS atmospheric corrections and Saturna AERONET measurements (July 2002 to July 2012). MODIS and AERONET data are plotted as shaded and black outlined bars, respectively. (N=581, 620, 618, respectively)

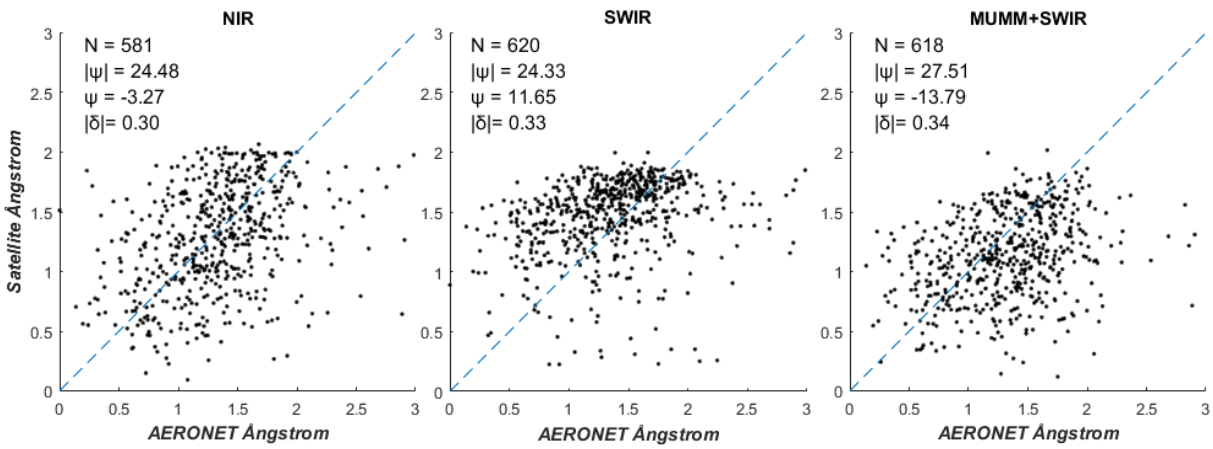

Figure 5. Regression results of MODIS to AERONET derived Ångstrom exponents. Here Ångstrom statistics are |ψ| and ψ (in %) and |δ| and (in Ångstrom units)

The results for the aerosol optical thickness are similar to the Ångstrom exponent results. For all the three atmospheric correction methods τ_a at shorter wavelengths (443nm) showed on average 87% less uncertainty, |ψ|, than longer wavelengths (870nm). All methods were positively biased (52.58% to 88.90%) indicating persistent MODIS overestimation. This is observed in Figure 6 where MODIS τ_a estimates are above the theoretical 1:1 line. For all wavelengths, the MUMM+SWIR exhibited the lowest uncertainty, ranging from 71.34% to 110.9%, and a slope closest to 1. This represents 22.2 to 23.1% less uncertainty when compared to the NIR method for the same bands (Table 2). Despite lower uncertainties, MUMM+SWIR had slightly lower R^2 values for the linear relationship. The highest bias for MUMM+SWIR occurs at τ_a(865nm) (88.9%). The SWIR method produces much higher |ψ| (150.0-200.0%), the lowest R^2 (0.18-0.19) and large positive biases (0.045 - 0.15 $\tau_a(\lambda)$).

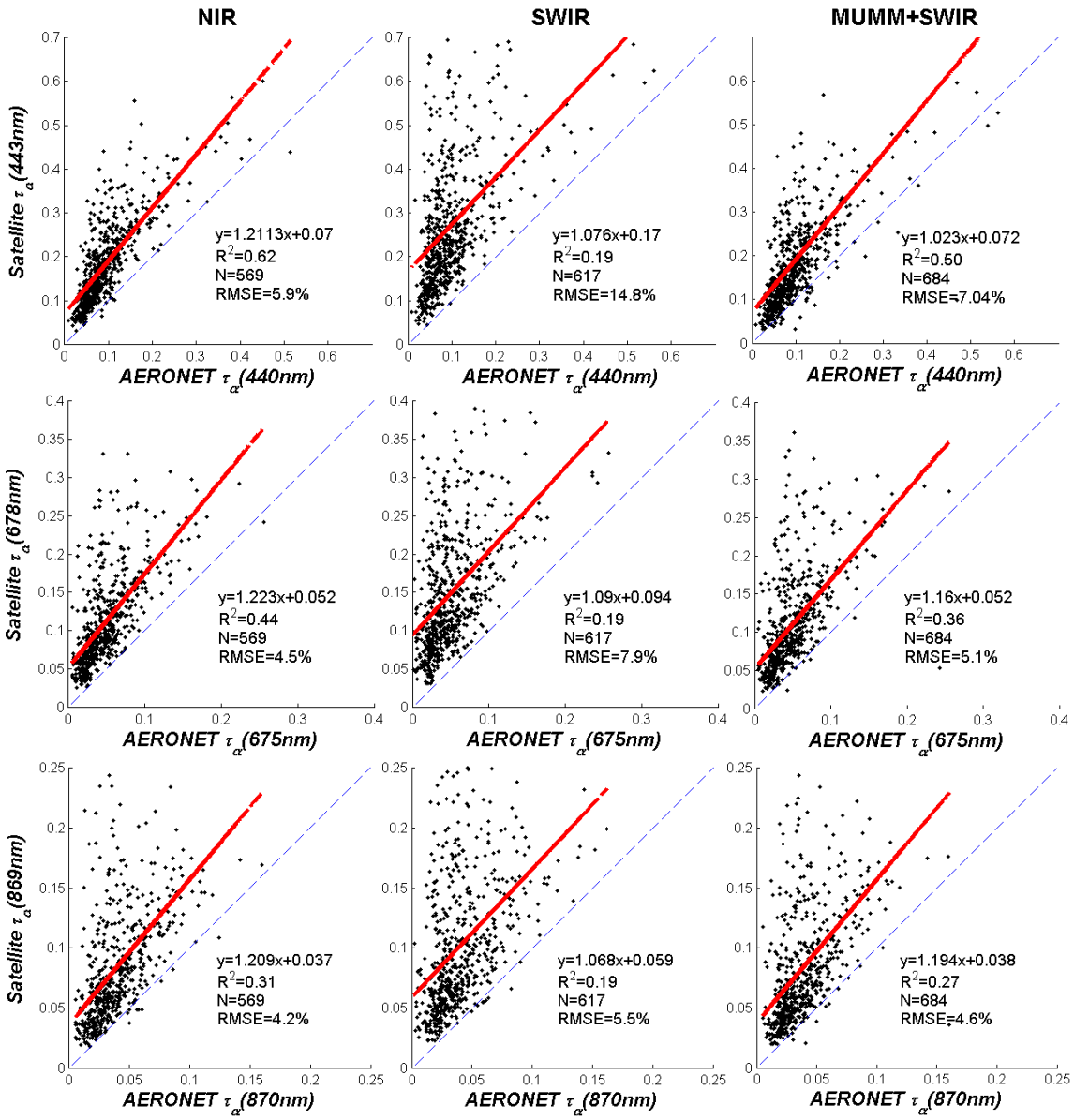

Figure 6. Matchup of MODIS to AERONET aerosol optical thickness at three wavelengths for three atmospheric correction procedures. Red line is the regression line of the equation, and dashed line indicates a hypothetical 1 to 1 relationship. 15 minute temporal difference.

Table 2. Validation statistics for the three atmospheric correction methods (Columns) for MODIS-derived τ_a expressed as $|\psi|$ and ψ (in %) and $|\delta|$ and δ (in τ_a units)

Parameter	NIR	SWIR	MUMM+SWIR
$\tau_{a\ (443nm)}$			
$\|\psi\|$ [%]	93.57	168.18	71.34
ψ [%]	+93.57	+168.18	+70.45
$\|\delta\|$	0.08	0.13	0.06
$\tau_{a\ (675nm)}$			
$\|\psi\|$ [%]	123.40	200.00	110.88
ψ [%]	+123.40	+200.00	+52.58
$\|\delta\|$	0.05	0.08	0.05
$\tau_{a\ (865nm)}$			
$\|\psi\|$ [%]	91.76	150.00	88.90
ψ [%]	+91.76	+150.00	+88.90
$\|\delta\|$	0.03	0.05	0.03
Å(440,870nm)			
$\|\psi\|$ [%]	24.48	24.33	27.51
ψ [%]	-3.27	+11.65	-13.79
$\|\delta\|$	0.30	0.33	0.34

5.1.2 Remote Sensing Reflectance: HyperSAS R_{rs} and MODIS R_{rs}

There were 13 to 34 matchups for the $R_{rs}(\lambda)$ analysis between various MODIS imagery atmospheric corrections and HyperSAS measurements within the defined ±3 hour temporal window from the 194 HyperSAS measurements acquired during the CCGS W.E. Ricker and R/V John Strickland Cruises (Table 1). Individual atmospheric correction methods produced different match ups between HyperSAS $R_{RS}(\lambda)$ and MODIS $R_{rs}(\lambda)$ as a result of differing pixels for the same image. Cloud cover over the area during the sampling period resulted in the small number of total observed matchups.

The NIR method produced the highest average incidence of matchups (n=29) across all wavelengths with the lowest percentage of negative values (15%) followed by the

MUMM+SWIR (n=20, 24%) then the SWIR (n=13, 47%), respectively. For all methods, the greatest frequency of negative $R_{rs}(\lambda)$ occurred in the 412 and 443nm bands. The NIR method was the only method that did not result in negative R_{rs}(488-547nm). In contrast, nearly half of all SWIR-derived $R_{rs}(488-547\text{nm})$ were negative, and therefore, invalid. All negative $R_{rs}(\lambda)$ values (mostly blue wavelengths) were removed and all remaining positive values were investigated for further analysis.

The mean absolute percentage difference of the dataset ranged between 38%-404% (NIR), 53%-587% (SWIR), and 37%-56% (MUMM+SWIR). The SWIR method produced the highest percent APD in the 412 and 443 bands, followed by NIR (404%, 98%), with the lowest APD for 667nm. Of the three methods, the SWIR method exhibited the highest APD for all bands. It also exhibited more negative bias and high dispersion around a theoretical 1:1 relationship (Figure 7). MUMM+SWIR produced the lowest APD% and RPD% for the 412-488nm bands (42% and 48%, respectively), but was comparable to the NIR method for the 531nm and 547nm bands. MUMM+SWIR was the only method to produce negative biases for all bands, indicating that the atmospheric correction generally produced lower reflectance values when compared to *in situ* HyperSAS $R_{rs}(\lambda)$. The extreme APD for the NIR method is attributed to one station ('k53', Fig 7.) from the Komick dataset (2008), located north of Texada Island. When this station is excluded from this method, the APD is reduced to 412nm=46%, and 443nm=53% (versus 404%, 98%, respectively). SWIR APD for 412nm was also reduced with the removal of this station from 587% to 28%. MUMM+SWIR was minimally affected by the removal of Station k53 for

412nm and 443nm (1.2% and 13% respectively). Longer wavelengths for all three methods were not greatly affected by the station.

Regression analysis between HyperSAS and MODIS reflectances varied across all three methods. The NIR method resulted in poor correlation coefficients (R^2=0.09) and slopes (<0.2) for the 412nm and 443nm and moderate-strong relationship to *in situ* data for the 488-547nm bands with correlation coefficients ranging from 0.68-0.81, and slopes of 0.69-1.0. The SWIR method showed the poorest correlation across all bands, with slopes ranging 0.27-0.51 indicating it achieved only weak-moderate relationships to *in situ* $R_{rs}(\lambda)$. While the MUMM+SWIR technique was moderately correlated in all bands (R^2=0.53 ± 0.14) with slopes of 0.66 ± 0.19, thus showing the most consistent of all methods for bands above 412nm. In bands greater than 412nm the average slope was 0.62 ± 0.04 showing a consistent overestimation of the atmospheric correction technique across all bands.

Table 3. Results of MODIS and HyperSAS $R_{rs}(\lambda)$ comparison. Percentage of negative retrievals given. Statistics based on all remaining positive values.

Method	(λ)	% Negative	Count (N)	APD %	RPD %	RMSE	R^2	Slope
NIR	R_{rs}(412)	62	14	404	321	0.002	0.09	0.18
	R_{rs}(443)	15	29	99	-4	0.002	0.09	0.16
	R_{rs}(488)	0	34	58	-31	0.002	0.68	0.69
	R_{rs}(531)	0	34	54	-9	0.002	0.7	1.07
	R_{rs}(547)	0	34	38	157	0.002	0.81	1
	R_{rs}(667)	12	30	54	-35	0.002	0.71	0.31
	Average	**15**	**29**	**118**	**67**	**0.002**	**0.51**	**0.57**
SWIR	R_{rs}(412)	64	9	587	550	0.003	0.06	0.27
	R_{rs}(443)	56	11	151	107	0.003	0.12	0.34
	R_{rs}(488)	56	11	74	16	0.003	0.31	0.43
	R_{rs}(531)	40	15	54	-20	0.004	0.4	0.51
	R_{rs}(547)	28	17	53	-32	0.004	0.33	0.46
	R_{rs}(667)	40	13	70	-32	0.002	0.14	0.29
	Average	**47**	**13**	**165**	**98**	**0**	**0.23**	**0.38**
MUMM+SWIR	R_{rs}(412)	52	13	42	-13	0.002	0.47	0.85
	R_{rs}(443)	37	16	48	-6	0.002	0.44	0.66
	R_{rs}(488)	19	22	56	-22	0.002	0.45	0.61
	R_{rs}(531)	11	23	44	-10	0.002	0.54	0.61
	R_{rs}(547)	4	23	37	-14	0.019	0.61	0.62
	R_{rs}(667)	22	21	43	-38	0.019	0.67	0.61
	Average	**24**	**20**	**45**	**-17**	**0.019**	**0.53**	**0.66**

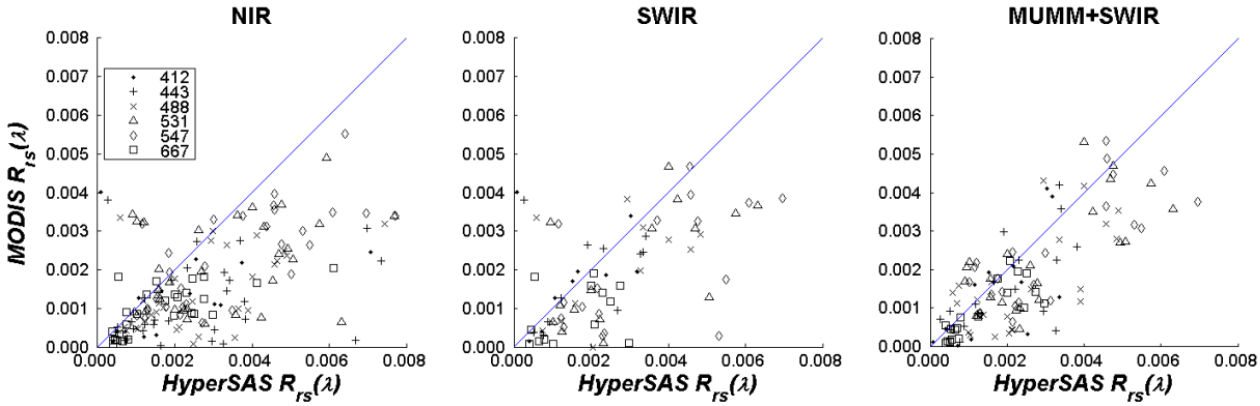

Figure 7. Matchup of MODIS remote sensing reflectance to convolved HyperSAS data. Respective bands are denoted with symbols. Horizontal line represents hypothetical 1 to 1 relationship.

To compare spectral distributions between all three methods, MODIS $R_{rs}(\lambda)$ to *in situ* $R_{rs}(\lambda)$ matchups that are concurrent of all methods were plotted (Figure 8). Here stations labelled "R#" were collected from the 2012-2013 Ricker Cruises, while "K#" stations were from the previous work by Komick (Table 1). The results show that the SWIR and NIR corrections produced generally flatter spectral shapes and negative reflectance values when compared to the MUMM+SWIR. Specifically, a greater proportion of results based on NIR and SWIR methods showed negative reflectance in the 412nm, 443nm, and 488nm bands relative to MUMM+SWIR. The absolute percentage difference across these bands supports this observation (Figure 9). All three methods produced ≥10% overcorrection, with NIR and SWIR producing errors ≥30% and MUMM+SWIR producing errors <20% at wavelengths longer than 443nm, respectively. The 412nm band exhibited the highest errors, where MUMM+SWIR overcorrected by 38% and both NIR and SWIR methods were upwards of 70%. The 531nm and 547nm showed the greatest similarity, while 443nm and bands between 667-678nm showed greater differences.

Given that the OC3M models rely on the ratio, X, of 443nm or 488nm to 551nm bands to derive accurate chlorophyll concentration $(\text{Equations } 11-12)$. The MUMM+SWIR method generally results in more accurate $R_{rs}(\lambda)$ in the bands specifically used for *chla* determination (Figure 8). Ratio X was compared to derived HyperSAS reflectance to MODIS (n=16, from Figure 7) according to the different atmospheric methods. Here MUMM+SWIR exhibited the lowest average absolute difference and variance to *in situ* (1.33, 0.17 sr^{-1}) compared to NIR (1.42, 0.19 sr^{-1}) and SWIR (1.33, 0.35 sr^{-1}).

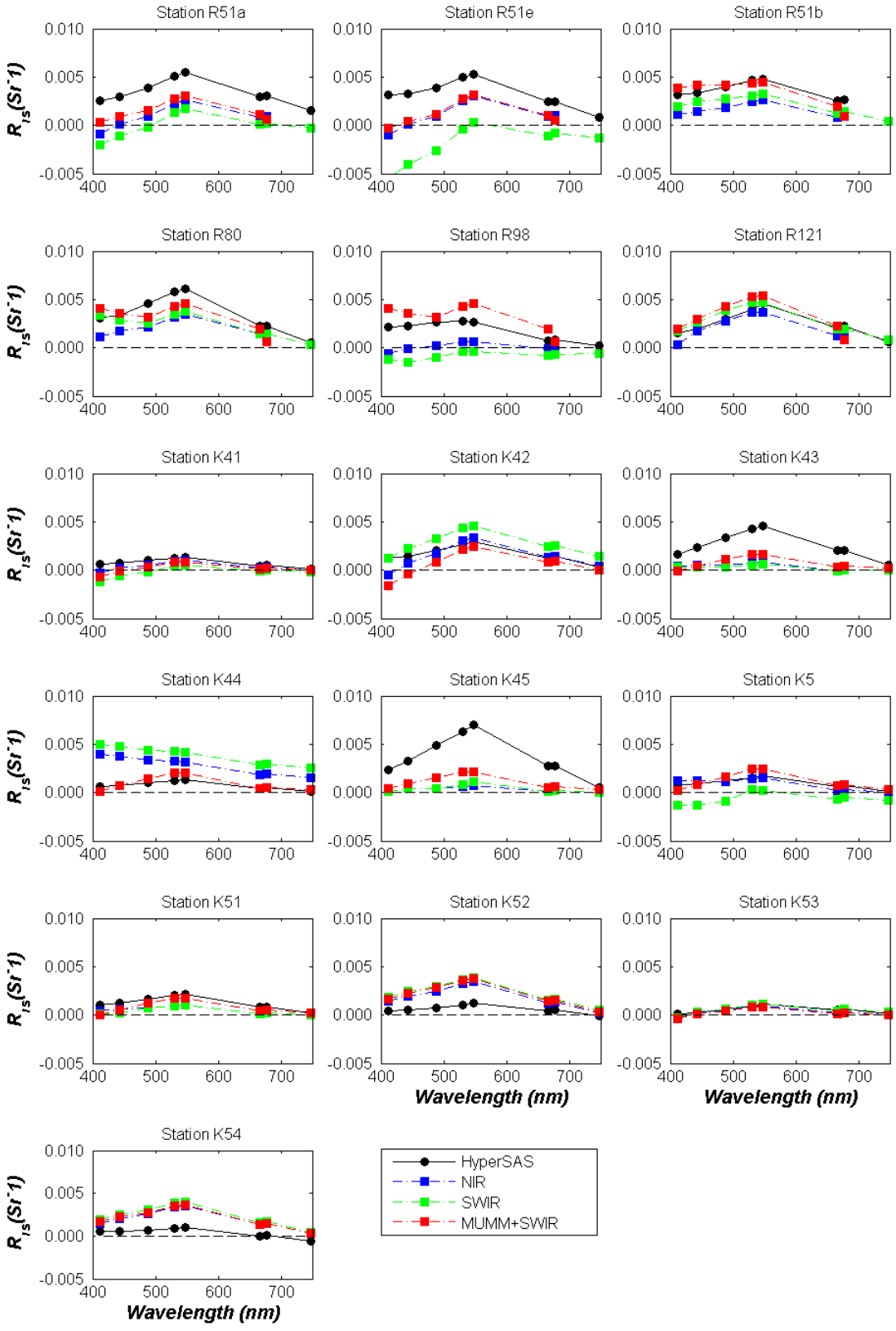

Figure 8. Relationship of MODIS to convolved HyperSAS $R_{RS}(\lambda)$ for NIR, SWIR, and MUMM+SWIR atmospheric corrections.

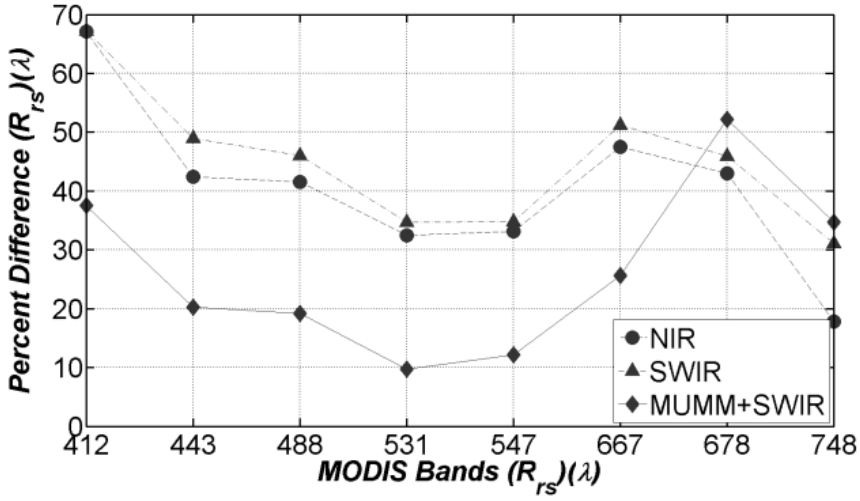

Figure 9. Comparison of matching satellite-derived to *in situ* (HyperSAS) remote sensing reflectance for three atmospheric correction schemes. Y-axis indicates negative percent difference to respective MODIS bands along x-axis (N=16)

4.2 Chlorophyll matchup evaluation

MODIS-OC3M derived versus *in situ* chlorophyll concentrations for the three atmospheric correction methods were compared for five (±1hr to ±8hrs) time differences (Figure 10) between *in situ* measured and satellite overpasses (Table 4). For both the NIR and SWIR methods extreme outliers were present with MODIS chlorophyll estimates in excess of 150 mg m^3 sampled at less than ±2 hours image acquisition. The NIR method produced lower correlation coefficients and slope while producing consistent RMSE values. The consistently large APD and RPD paired with small correlation and low slope indicate that the NIR method is not appropriate to derive chlorophyll concentration in these waters. MODIS NIR values above ~30mg skew the relationship, and removal of these data would produce a better relationship. The SWIR results exhibit a consistently high APD and RPD over the temporal periods, and consistently low correlation coefficients and slope. This indicates the method also fails to retrieve accurate chlorophyll concentrations as results

have high uncertainty, large positive bias, and tends to underestimate concentrations. In contrast, the MUMM+SWIR method exhibited consistently the lowest APD, bias, residuals, a slope closest to 1.0, and a R^2 of 69%. Perhaps most importantly, it is the only method with increasing correlation and slope closer to 1.0 with finer temporal differences (Table 4).

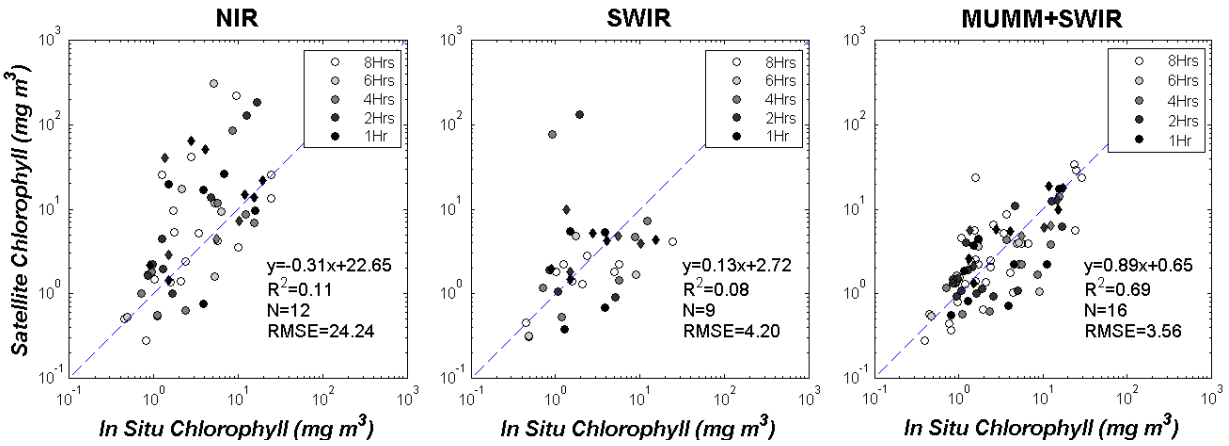

Figure 10. Relationship between MODIS derived chlorophyll concentration and *in situ* samples for different temporal differences. Circles represent Institute of Ocean Sciences data, while diamonds represent High performance liquid Chromatography results. Statistics are given for the one hour temporal difference.

Table 4. Summary statistics for MODIS vs. *in situ* remote chlorophyll concentrations

Method	Parameters	Count (N)	APD %	RPD %	$_{log}$RMSE	R^2	Slope
NIR	*chla* 8 hours	54	481	453	0.66	0.05	2.07
	chla 6 hours	38	510	483	0.67	0.06	2.75
	chla 4 hours	32	394	368	0.63	0.17*	2.87
	chla 2 hours	23	489	472	0.69	0.20	3.24
	chla 1 hour	12	460	438	0.69	0.11	-0.31
SWIR	*chla* 8 hours	35	508	452	0.60	0.01	-0.49
	chla 6 hours	26	667	611	0.70	0.02	-1.04
	chla 4 hours	23	741	688	0.70	0.02	-1.18
	chla 2 hours	16	529	482	0.65	0.01	-0.84
	chla 1 hour	9	82	31	0.43	0.08	0.13
MUMM+SWIR	*chla* 8 hours	83	80	35	0.36	0.55*	0.77
	chla 6 hours	52	62	14	0.35	0.58*	0.69
	chla 4 hours	46	62	15	0.34	0.60*	0.71
	chla 2 hours	34	67	27	0.33	0.63*	0.75
	chla 1 hour	16	62	21	0.33	0.69*	0.89

Note: *p < 0.05.

Examples of final *chla* maps produced from the respective atmospheric correction techniques are shown in Figure 11. Three dates are shown and correspond to winter, spring and summer condition, respectively. February results show lower presence of *chla* (<2.0mg m^{-3}), and large areas of null data for all three methods. The low chlorophyll concentrations and lack of data is consistent with the whole dataset for this time of year, where growth is often light limited, in part due to presence of clouds (Allen & Wolfe, 2013). An example of spring-bloom conditions is shown for April 2, 2008, where *chla* concentrations are in excess of 20.0 mg m^{-3} through a majority of the SoG. The SWIR method produces a noisy distribution of *chla*, with the majority of values within the 5.0±3.0 mg m^{-3} range. The NIR method produces the most extreme values of *chla* within the SoG, generally ranging from 5.0-20.0 mg m^{-3}, with large central areas in excess of ≥60.0 mg m^{-3}. In Figure 11, this is directly associated with negligible (<0.001) and negative

reflectances in the blue wavelengths (412nm & 443nm). Removal of NIR chl*a* pixels associated with these reflectances removes nearly all remaining data in the SoG (not shown). In contrast to the first two methods, the MUMM+SWIR technique produces consistent pixel-pixel variability with chlorophyll ranging 3.0-20.0mg m^{-3}, with distinguishable bloom features. The relative noise and extreme values are present during summer conditions for the NIR and SWIR methods. MUMM+SWIR remains relatively consistent, however much of the data in the northern SoG in the example for 9th September is flagged for negative reflectances (443nm) and removed.

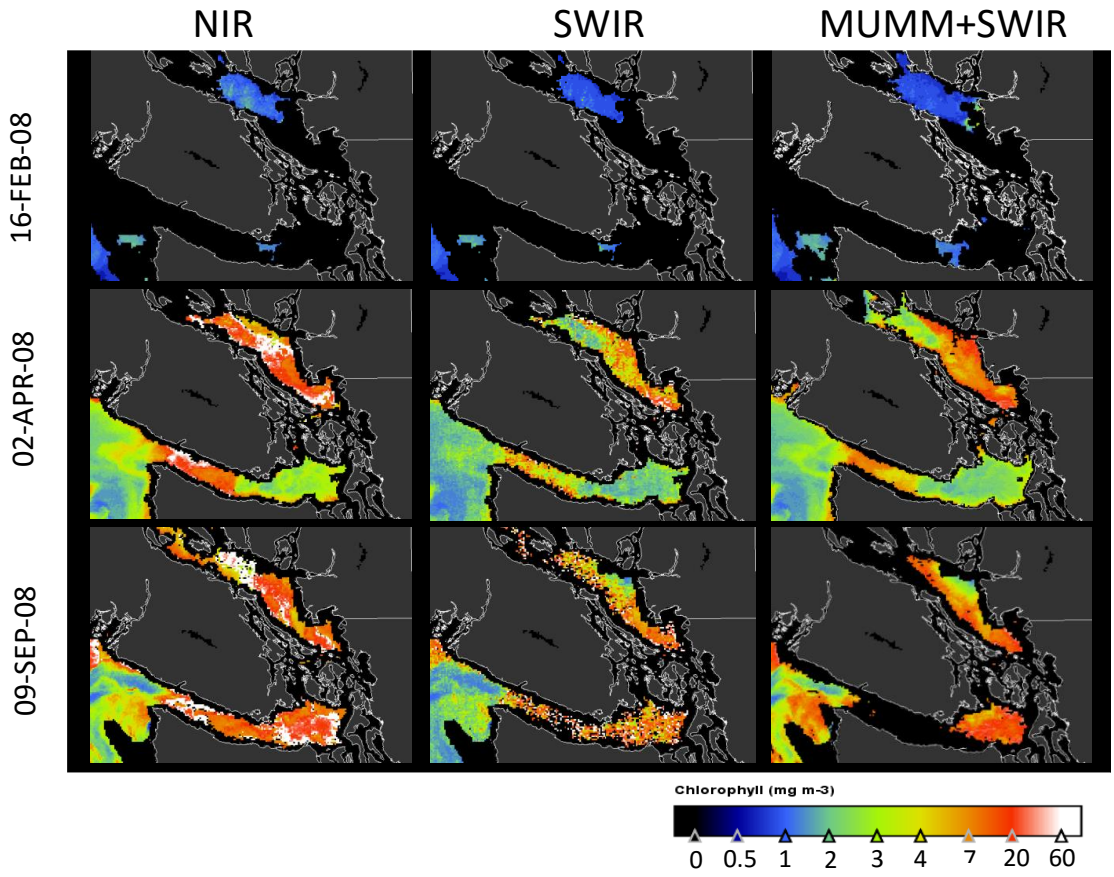

Figure 11. Example chlorophyll distribution maps for February, April, and September.

4.3 Binned *chla* time series

The combined analyses of atmospheric correction (section 4.1) and *chla* (section 4.2) components support the MUMM+SWIR as the most appropriate method of the three presented atmospheric correction in determining the most accurate chlorophyll concentrations for the SoG. Therefore, the MUMM+SWIR *chla* products were selected to construct a 2002-2014 time series of weekly binned chlorophyll as per the decision framework illustrated in Figure 3. For the 2002-2014 binned dataset an average of 21.5% of pixels in both the Northern and Central regions were flagged (§ 3.2) and removed from the analysis. Of the remaining valid pixels used to create 8-day bins, there was an average of 46.2% spatial *chla* coverage for the central region compared to 33.2% available for the Northern region. The increased coverage is primarily due to start and end of year (winter) values, where there is an average of 18% more coverage for the central region due to less solar-zenith flagging.

The Central and Northern *chla* time series presented in Figures 12-13 exhibit several distinct trends. In general there is a moderate seasonality in the central SoG, where lower values (<5.0mg m^{-3}) are present at both beginning and end of year corresponding to winter conditions, and higher median *chla* values (10.0-20.0 mg $^{-3}$) present in the spring and summer periods. Typically, *chla* values in the Northern region are lower than 3.0 mg m^{-3} during winter months. Higher concentrations are generally observed after February of each year, and are consistently higher from April through June (Figure 12). Pulses of elevated *chla* in the Northern region tend to coincide with larger bloom periods in the

Central region, but are lower in both magnitude and duration. The median absolute deviation, representing spatial variability of *chla* within the specific region, indicates that periods of highest variability occur during spring and summer conditions; while during winter, less variability associated to lower *chla* magnitude (generally ≤ 3mg m^3) are observed for both regions. The *chla* time series also shows that, for both the Central and Northern regions, late summer and fall blooms occur. Fall blooms are more prevalent in the Central region where *chla* exceeding 5.0mg m^{-3} occurs after September for every year with the exception of 2007 (Figure 13). The most notable fall event occurred in 2005, with Central SoG *chla* peak exceeding 20.0mg m^{-3}, followed by a similar event in 2010 (16.0 mg m^{-3}) (Figure 12). Based on the bloom criteria for YD_{dur} in section 3.5, the central SoG maintains continuous spring bloom conditions for an average of 7 weeks, in which the longest YD_{dur} spring bloom occurred in 2007 lasting approximately 160 days (Table 5) with *chla* concentrations on average 8.0 mg m^{-3}, and the shortest duration occurred in 2010 (~8 days) with *chla* average of 10.8 mg m^{-3}. Similar YD_{dur} results were observed for the Northern region for these years, however, average concentrations were 7.6 mg m^{-3} and 8.0 mg m^{-3}, respectively.

Despite the observed interannual differences in regard to chlorophyll concentrations and duration of the spring bloom, the results indicate that, on average, the spring bloom YD_{init} is on March 29 (day=88 ±4 days) and on March 20 (day=80 ±4 days) for the Central and North SoG, respectively (Table 5 and Figures 13 & 14). However, 2005 had the earliest YD_{init} dates with the Central region blooming on February 22 (day=53 ±4 days) and the Northern region approximately one week later on March 2 (day=62 ±4 days). In 8 out of

the 12 years analyzed, the spring bloom initiated on average 9 days earlier in the North compared to the Central region. Also, bloom duration, $YD_{dur,}$ tends to last an average of 9 days longer in the Central compared to the North SoG, and YD_{max} occurs nine days earlier. In terms of *chla* concentrations during YD_{dur}, the average *chla* is 8.6 mg m^{-3} and 6.0 mg m^{-3} for the Central and North, respectively. Therefore, when compared to the Central region, the Northern bloom generally starts earlier, is of a lower magnitude, and shorter in duration in comparison with the Central bloom.

Table 5. Summary of derived bloom metrics for Central and Northern SoG including timing of initiation (YD_{init}), timing of maxima (YD_{max}), and duration of the spring mass (YD_{dur}). Estimates of initiation dates from a Hindcast model (Allen & Wolfe, 2013), and MODIS flourescent line height (FLH)(J. Gower et al., 2013) are given.

	Central			North				
Year	YD_{init} (±4)	YD_{max} (±4)	YD_{dur} (±8)	YD_{init} (±4)	YD_{max} (±4)	YD_{dur} (±8)	Hindcast (±4)	FLH
2003	101	149	32	105	149	24	86	84
2004	69	117	56	65	85	64	81	71
2005	53	133	56	49	117	24	62	56
2006	85	117	88	57	117	48	88	84
2007	101	117	160	65	176	128	100	47
2008	93	125	96	49	125	24	90	71
2009	69	125	136	97	133	64	97	55
2010	109	109	8	105	109	8	104	83
2011	101	149	16	105	149	16	102	97
2012	85	109	48	65	141	24	98	90
2013	93	117	24	89	157	40	88	69
2014	93			97			86	92
Average	88	124	65	79	133	42	90	75

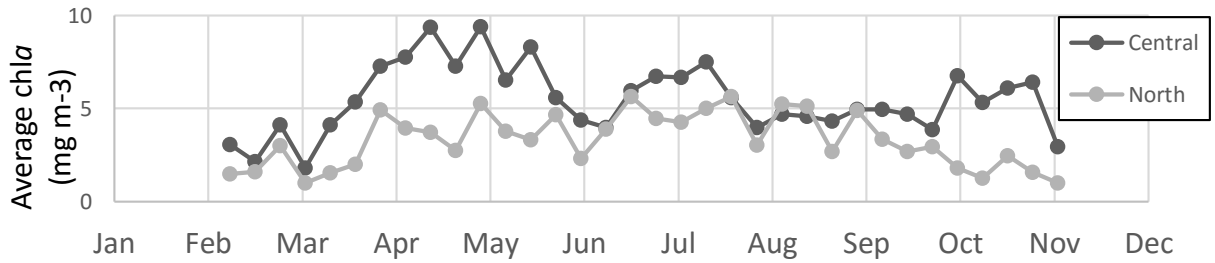

Figure 12. Weekly-averaged Chlorophyll timeseries for the Central (dark line) and Northern (grey line) SoG (2003-2014).

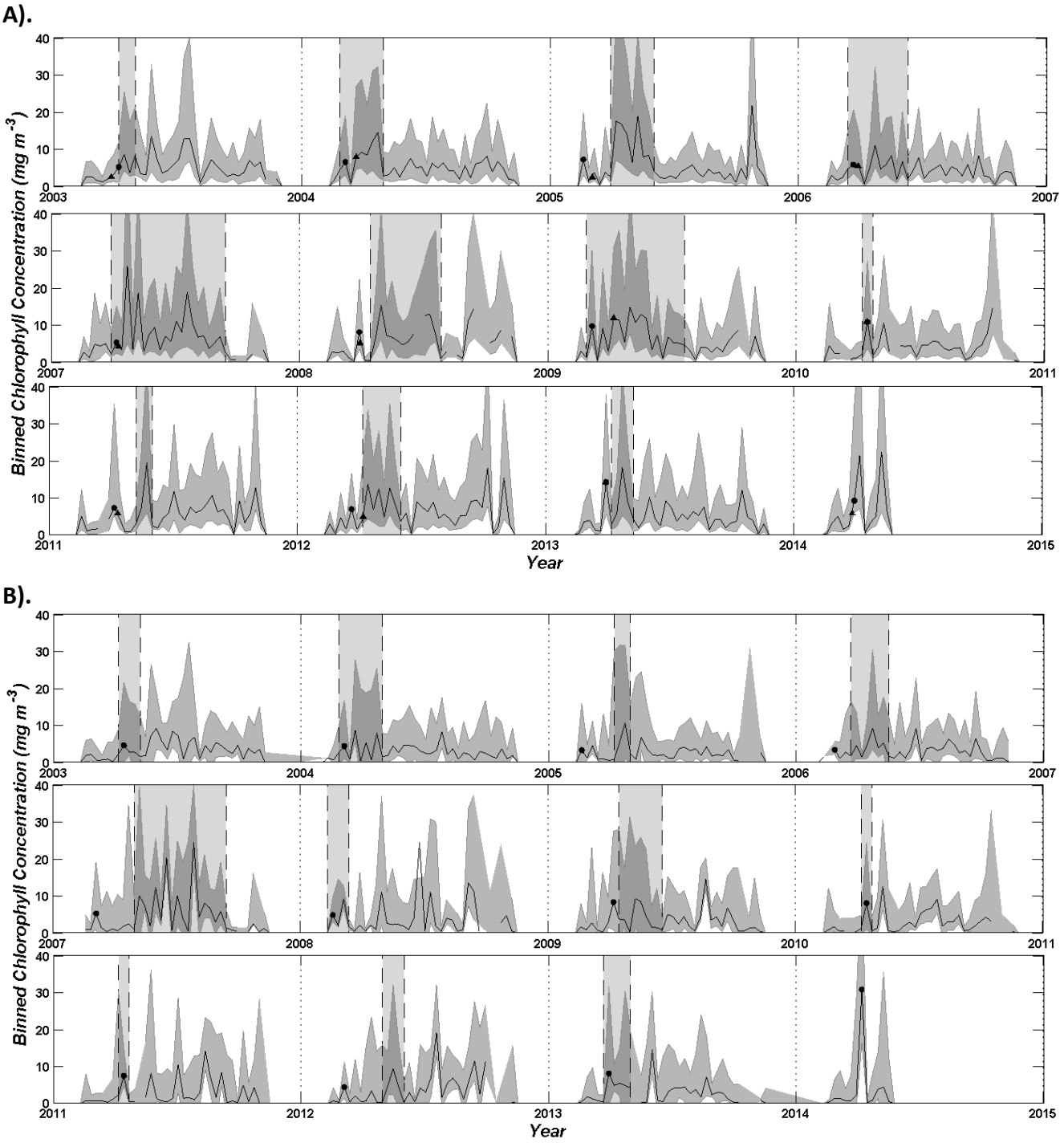

Figure 13. 8-day Binned *chla* time series (black line) for the A). Central SoG and B). Northern SoG for the period 2003-May, 2014 using the MUMM+SWIR atmospheric correction and OC3M *chla* algorithm. Shaded area indicates 1-Median absolute deviation about the median. Black circle represents bloom start date, and areas bounded by hash marks indicate the calculated spring bloom bulk.

A).

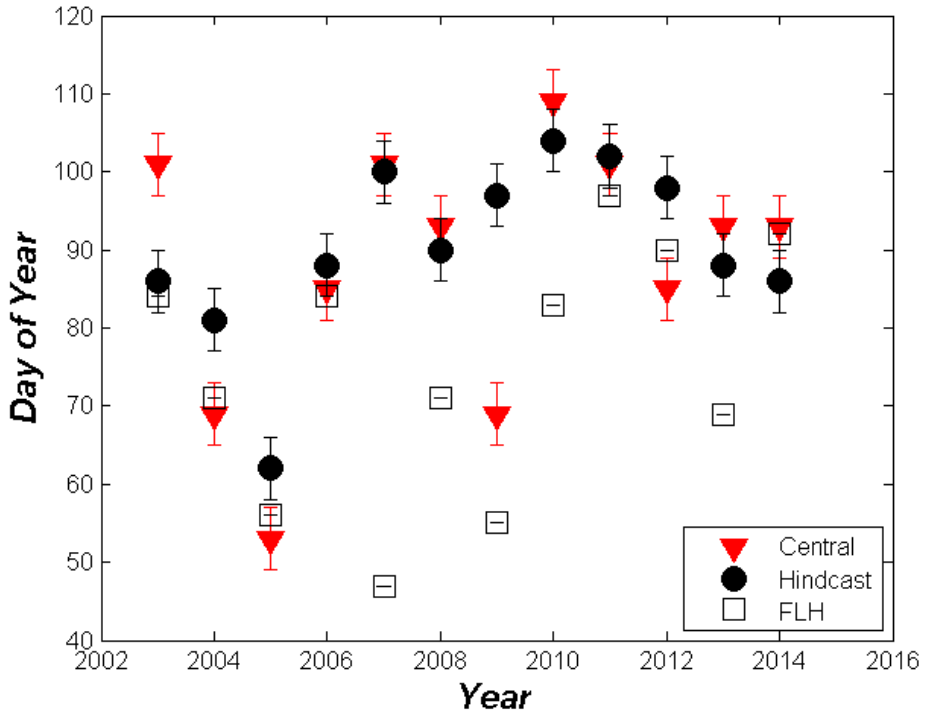

B).

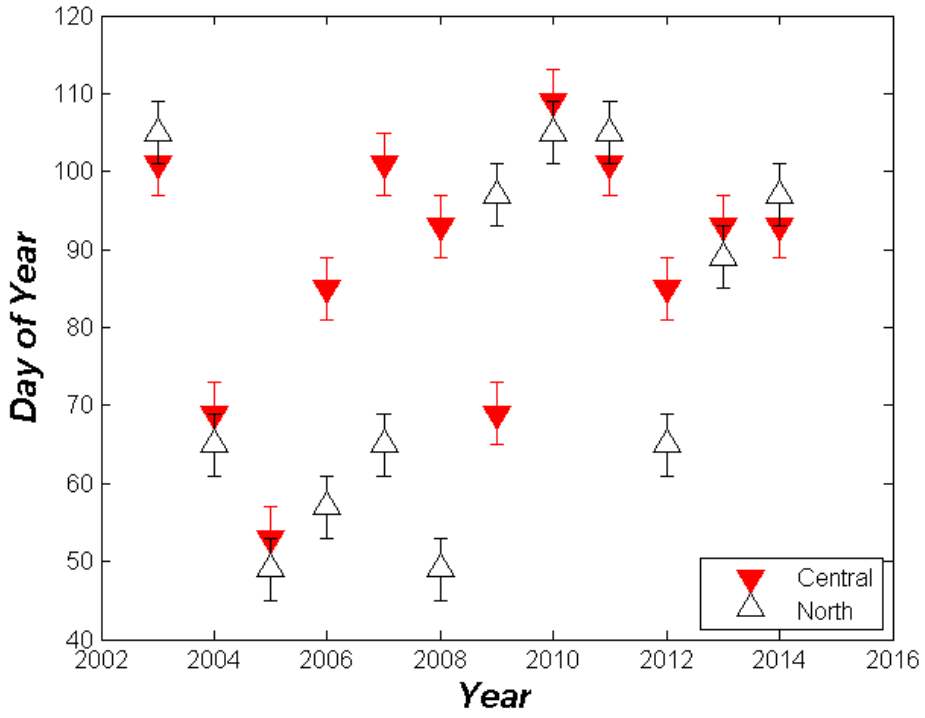

Figure 14. A). A comparison of spring bloom start dates for the central SoG including Allen & Wolfe's (2013) *Hindcast model*, and Fluorescence Line Height (FLH) *(Gower, et al.*, 2013). B). Bloom start date estimates for the Northern SoG.

5.4.1 Hierarchical clustering of spring seasons

For the Central SoG, HCA analysis indicates that six of the eleven years are positively correlated (r) with one or more years, and are statistically significant at the $p < 0.05$ level (Table 4). The most correlated years are 2009 to 2012 (r=0.8) and 2003 to 2011 (r=0.67), while 2004-2010 showed no correlation. Year 2008 showed most dissimilarity to any other year in a subcluster. These results correspond to the first join in the dendrogram of the Central region (Figure 15), where clustering groups based on correlation and averaging produces two distinct final clusters. In contrast, similarity tables for the Northern region indicate there is less correlation between spring seasons, where only two of eleven years showed correlation with significance ($p < 0.05$). The most correlated years were again 2009 to 2012 (r=0.62), followed by moderately correlated 2007 to 2012 (r=0.53) seasons.

Table 6. Correlation coefficients values (Pearson's correlation) between spring chlorophyll time series of each year (A. Central, B. North)

A).

Year	2003	2004	2005	2006	2007	2008	2009	2010	2011	2012	2013
2003	-										
2004	-0.04	-									
2005	0.27	0.37	-								
2006	-0.10	0.37	0.12	-							
2007	0.03	0.35	0.52*	0.57*	-						
2008	0.28	-0.18	-0.12	0.33	0.15	-					
2009	0.44	0.10	0.55*	-0.04	0.02	0.21	-				
2010	0.31	0.00	0.60*	-0.04	0.19	-0.01	0.29	-			
2011	0.67*	-0.21	0.18	-0.24	-0.10	-0.02	0.32	0.01	-		
2012	0.48*	0.22	0.38	0.33	-0.01	0.29	0.80*	0.29	0.22	-	
2013	0.18	0.57*	0.11	0.59*	0.51*	0.47	-0.08	-0.13	-0.20	0.11	-

Note: *$p < 0.05$.

B).

Year	2003	2004	2005	2006	2007	2008	2009	2010	2011	2012	2013
2003	-										
2004	0.16	-									
2005	0.01	0.32	-								
2006	0.18	0.01	0.28	-							
2007	-0.06	0.27	0.33	0.47	-						
2008	0.33	-0.11	-0.13	0.47	-0.16	-					
2009	0.00	0.18	0.17	0.10	0.42	0.00	-				
2010	-0.03	-0.28	-0.09	0.23	0.53*	-0.07	0.42	-			
2011	0.40	-0.26	0.20	-0.13	-0.13	-0.12	0.25	0.21	-		
2012	0.07	0.03	0.28	-0.17	0.05	0.16	0.62*	0.22	0.29	-	
2013	0.40	0.10	-0.01	0.22	0.02	-0.04	-0.07	-0.10	0.05	-0.37	-

Note: *$p < 0.05$.

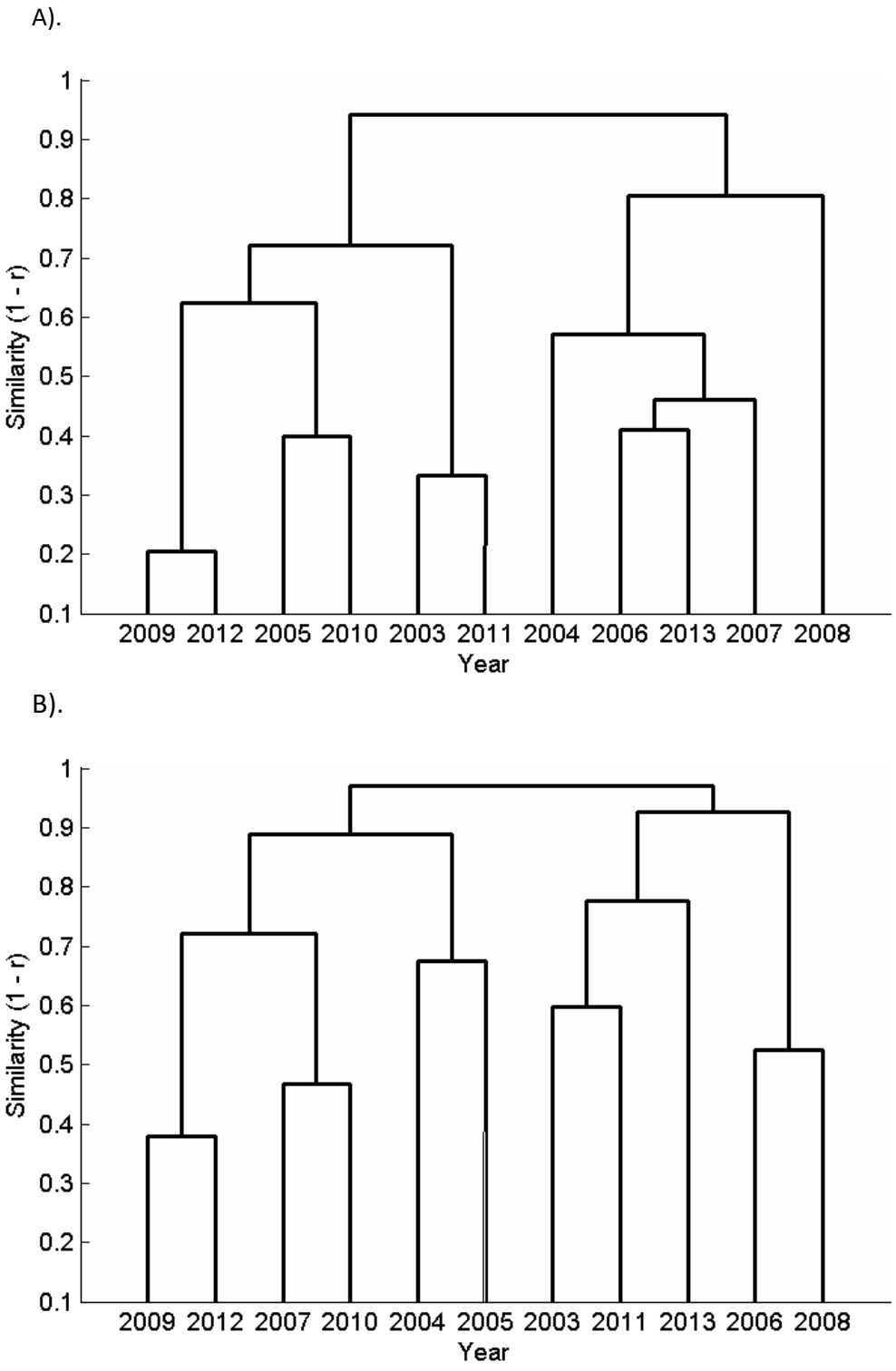

Figure 15. Hierarchical clustering results indicating similarity of interannual spring blooms for A). Central and B). Northern Strait of Georgia for the period of 2003-2013.

Chapter 6 - Discussion

Recovering biogeochemical data, including phytoplankton bloom dynamics, from satellite imagery requires validation of both the atmospheric correction of images and the chlorophyll derived products (ZhongPing *et al*., 2010; Werdell *et al*., 2009). To achieve these requirements, in optically complex waters of the Strait of Georgia we (1) evaluate three atmospheric correction techniques in comparison with AERONET *in situ* and spectral *in situ* data, and (2) validate OC3M *chla* derived with *in situ chla* data. The most appropriate technique, MUMM+SWIR, represents an improvement over the Standard NIR correction, and was subsequently used to create a time series (2002-2014) of chlorophyll products and derive phytoplankton phenology in the SoG. The phenologies presented here provide insight into the spatial and temporal patterns of spring blooms in the Strait of Georgia. In particular, for the first time, estimates of spring bloom duration and maxima are defined as well as refined initiation dates. The accuracy of satellite derived products followed by the analysis of derived phytoplankton phenology will be discussed.

6.1 Product Validation

6.1.1 Atmospheric correction

To understand the capabilities of the three atmospheric correction method to accurately retrieve $\rho_w(\lambda)$ required for *chla* determination, products of the each method were compared to a stationary AERONET site and radiometric samples collected throughout the SoG. The NIR method was the most accurate to *in situ AERONET data* for all analyzed atmospheric properties, closely followed by MUMM+SWIR, while SWIR method was consistently the least accurate (Figures 4-6, Table 2). Radiometric samples from a broad

range of geographic and water conditions, however, showed a much closer agreement to the MUMM+SWIR over NIR for retrieving accurate ρ_w in the bands required to calculate chlorophyll concentration based on the OC3M algorithm (Figure 9, Table 3). Ultimately, the MUMM+SWIR approach was best for determining *chla* retrievals in the SoG (Fig 10, Table 4).

The NIR and SWIR approaches are derived through the same iterative procedure, with exception of bands substitution to choose the aerosol model (Sanwlani *et al*., 2011; Wang & Shi, 2005; Wang *et al*., 2009a). Despite similarities in procedure to solve for ρ_t, SWIR performed significantly worse for all matchups with the largest absolute deviation of method retrievals (Table 3, Figure 8). The current MODIS SWIR band (1240nm) used for ocean color was originally designed for land and atmosphere applications, which generally represents bright signals (Franz *et al.*, 2006). While there exists a 1640nm band designed for ocean color, it is currently non-functional due to a number of broken detectors (Vanhellemont & Ruddick, 2015). The non-functional 1640nm band has a much larger theoretical signal-to-noise ratio (SNR) compared to the 1240nm band (275 vs. 74, respectively). Although the current 1240/2130nm SWIR bands have produced effective results in turbid waters *(Shi & Wang, 2014a; Wang et al.*, 2013b), more recent studies, similar to our results, show that the lower SNR often produces poor outcomes (Vanhellemont & Ruddick, 2015; Wang & Shi, 2012; Werdell *et al.*, 2010). Lower SNR produces increased SWIR dynamic ranges leading to large percent differences and overall variability of MODIS $\tau_{a,}$ and ultimately inaccurate final chlorophyll products (Table 4). Our results are corroborated with observations by Werdell *et al*., (2010) and Chen *et al*.,

(2013) where products derived using current SWIR bands are less accurate than standard NIR bands (748 and 869 nm)(Wang & Shi, W., 2005).

There is a recognition of the need for future ocean colour sensors to have integrated SWIR bands with the required sensor SNR characteristics (180 for 1640nm, 100 for 2135nm) for turbid waters (Vanhellemont & Ruddick, 2015; Wang *et al*., 2009b; Werdell *et al*., 2010). In the most turbid conditions, a low level of reflectance from the water column have been reported by several authors at 1240nm (Dogliotti *et al*., 2011; Knaeps, Dogliotti, Raymaekers, Ruddick, & Sterckx, 2012; Shi & Wang, 2009, 2014b; Doxaron; Lavander *et al.*, 2005). Turbidity in the SoG reached values of 1.49-3.84 mg L^{-1} in the Northern region with much higher values ranging from 10.9 to 26.6 mg L^{-1} for the central region (Figure 2), which is consistent to previous studies of the region (Johannessen *et al*., 2006; Komick *et al*., 2009; Loos & Costa, 2010). High turbidity levels in the SoG may cause non-negligible $R_{rs}(1240nm)$, resulting in poor method retrievals. Improved SWIR band SNR is defined for the Sea and Land Surface Temperature (SLSTR) sensor onboard the upcoming Sentinel-3 platform (Ruddick & Vanhellemont, 2015), although it remains to be seen whether the SLSTR characteristics will be sufficient for effective SWIR correction. Therefore the SWIR method, as defined here, is not an appropriate atmospheric correction technique for the SoG.

The remaining atmospheric correction methods (NIR, MUMM+SWIR) used in this study were derived from two very different approaches (Section 2.1). Overall, the MUMM+SWIR τ_a and Ångstrom AERONET matchups were similar, but not as effective as

NIR (Figures 4-7, Tables 2&3). These results conflict with HyperSAS and *chla* results, where MUMM+SWIR performed best.

Despite matchup similarity between NIR and SWIR in the absolute relative differences ($|\psi|$, in %), relative differences (ψ, in %), and absolute differences *(*$|\delta|$) of AERONET τ_a(443nm, 865nm) and Ångstrom, results of both methods are not as accurate as similar studies of European marginal seas (Mélin *et al*., 2013). In these studies, the NIR approach was compared with *in situ* AERONET for four major European coastal sites (Adriatic, Baltic, North, and Black Sea, 1999-2009). These sites exhibit much lower $|\psi|$ for τ_a(443nm) and τ_a(865nm) (14-26% and 13-28%, respectively) when compared to SoG NIR (93.57%, 91.76%) and MUMM+SWIR results (71.34%, 88.90%). SoG results corroborate a positive bias, however they are an order of magnitude more biased than in Melin *et al.* (2013) (+70 to +93% vs. +5 to +27%), but similar in absolute differences for τ_a(443nm) ($|\delta|$= 0.03-0.06). Interestingly, there was a higher degree of SoG Ångstrom similarity to the Adriatic Sea location, a constrained estuarine site bordered by anthropogenic aerosol sources. The SoG exhibited a higher $|\psi|$ (27.51% vs. 17%) and absolute difference ($|\delta|$= 0.34 vs. 0.269), but both were negatively biased 13%. When compared to average results from global analysis (Melin, Zibordi, & Holben, 2013; Mélin et al., 2013), the methods applied for the images from the SoG did not result in as accurate results. We speculate that this is likely attributed to the SoG being a much more constrained water body and air mass surrounded by anthropogenic inputs to aerosols in contrast to Melin, Zibordi, & Holben, (2013) whose results are largely influenced from more open and exposed coastal sites.

The MUMM+SWIR method, which was similar to NIR AERONET matchup results, used an aerosol type that was defined based on a sample from a Northern ROI in the SoG and assuming spatial homogeneity. The relatively close agreement to AERONET indicates the assumption of aerosol-type uniformity within the SoG is, at least, somewhat consistent. However, the inability of MUMM+SWIR method to resolve larger Ångstrom values indicates that the assumption of spatial homogeneity of aerosol properties may not be entirely accurate for the SoG. ROI selection in northern waters, under less urban influence to identify aerosol contribution for the entire region, results in values that do not always correspond to the AERONET data located in closer proximity to an urban environment (Figure 1). Any significant SoG aerosol gradient would produce the unintended consequence of ignoring southern urban aerosols when northern aerosol properties are applied to solve for $\rho_w(\lambda)$. The MUMM+SWIR method ability to better characterizes smaller angstroms while missing fine mode particles over 2.0 (Figure 4), corresponding to combustible particles and sulfates (Eck et al., 1999) may account for the observed results. Fine-mode carbonaceous aerosols alter atmospheric correction results through either incorrect selection of atmospheric models or, in the case of strongly absorbing aerosols, leads to significant over-estimation or aerosol radiance contributions and an overcorrection and negative reflectance in the blue bands (412 and 443 nm)(Gordon & Voss, 1999). Considerable negative bias (ψ = -13.79%) observed for Ångstrom estimates using MUMM+SWIR is evidence of different aerosol type composition in the northern waters where $\varepsilon(\lambda i,\lambda j)$ is defined. Specifically, the bias of the observed Ångstrom values results from $\tau_a(440nm)$ being proportionally larger than $\tau_a(870nm)$. High $\tau_a(440nm)$

can occur when aerosol single scattering albedo term, $\omega_{a,}$ decreases due to extinction from combustion by-products (Eck, 2005). Therefore, the significant carbonaceous aerosol loads present in the southern SoG (Hoff *et al*., 1997; Pawlowicz *et al*., 2007; Vingarzan & Thomson, 2004) may not be present in the relatively more isolated Northern ROI used to define ε(λi,λj) for the MUMM+SWIR method. Furthermore, the fraction of regional fine-mode absorbing aerosols show a temporal variability with increased levels occurring during summer (Eck, 2005; Edwards, 2004; Schurman *et al*., 2015). As a consequence, MUMM+SWIR efficacy is expected to vary depending on optical complexity and absorbing aerosol loading levels in the SoG. Therefore it is possible that MUMM+SWIR derived τ_a and Ångstrom will more closely match AERONET data during winter periods, or times of less fine-mode aerosol loadings in the more densely populated southern SoG. How τ_a uncertainty translates into R_{RS} uncertainties, however, depends on several factors including τ_a and aerosol reflectance relationships, and the relative contribution of the aerosol reflectance to the TOA signal (Mélin *et al.*, 2013).

All correction methods and AERONET matchups may be affected by the mismatch in absolute location of τ_a and Ångstrom ROI used for MODIS imagery. Previous analysis, however, indicates that slight variations of location and size of the nearby satellite pixel ROI does not significantly alter final comparisons (Mélin *et al*., 2010). Therefore, while it is unlikely that the 5x5 pixel-box used in the study (Section 3.2.1) significantly affected overall uncertainty and bias calculations, the spatial mismatch between satellite and AERONET samples on Saturna Island may have contributed to discrepancies in AOT and

Ångstrom matchups for all correction methods. While adjacent to the SoG, the Saturna AERONET site is located at an altitude of approximately 200m. The columnar integrated altitude difference between AERONET and MODIS methods means a difference in AOT being calculated, and therefore can create considerable bias for matchups (Schutgens, Nakata, & Nakajima, 2013).

The AERONET τ_a and Ångstrom results indicate that MUMM+SWIR method produced relatively adequate and similar aerosol retrievals as the NIR approach. The comparison with the *in situ* HyperSAS data, however, indicates that the MUMM+SWIR method retrieves more accurate reflectance values for the bands used in the OC3M algorithm, with the lowest percent difference, specifically for the ratios of 443 or 489 to 547 (O'Reilly *et al*., 2000) (Table 3). The advantage of the *in situ* HyperSAS data includes sampling from many locations throughout the SoG, representative of various water conditions and types (Figure 1). The MUMM+SWIR method produced smaller absolute error and variance (1.33, 0.17 sr^{-1}) than NIR (1.42, 0.19 sr^{-1}), when calculating reflectance ratio X compared to HyperSAS.

Since it is the reflectance ratio X that ultimately determines chlorophyll concentrations (Equations 11-12), these results indicate that MUMM+SWIR method produces the most accurate ρ_W(443, 488, 547nm) over a broad area and water conditions (Figure 9). This is an important consideration, as error in ratio X is propagated to *chla* determination. Absolute percentage difference results (Figure 9) contrast to a similar study focused on arctic waters (Mustapha, Bélanger, & Larouche, 2014a), that found standard NIR correction resulted in errors exceeding 70-120% in the blue bands and upwards of 50%

for the green and red bands. In contrast, all three methods tested in our study produced lower percent errors (<70% blue, <40% green). Trends of disproportionate R_{RS} error of blue and red bands compared to green bands are corroborated.

NIR systematic underestimation of $R_{rs}(\lambda)$ across all bands when compared to HyperSAS (Figure 7), suggests atmospheric overcorrection, and is coupled with a large range of APD and RPD compared to MUMM+SWIR (Table 3). The range in APD and RPD suggests that the atmospheric model selection and correction is not applied proportionally, likely a result of turbidity causing invalid model selection, and further CDOM absorption in the blue wavelengths affecting individual pixel $\rho_w(\lambda)$. Underestimation of the blue bands (443nm, 488nm) relative to green (547nm) likely resulted in the overestimation of *chla* over a broad range of water conditions for the study (Figures 10-11, Table 4), as reported in similar studies (Goyens *et al.*, 2013; Mustapha, Bélanger, & Larouche, 2014).

Unfortunately, our study had a small number of matchups for HyperSAS and the Saturna AERONET site is land-based. Improvements on the validation of atmospheric correction methods would be facilitated by increased number of *in situ* reflectance data such as other coastal sites that equipped with AERONET-OC (Ocean Colour) network (Zibordi *et al*., 2010; McCarthy *et al*., 2012), or many ship-based initiatives (Garaba & Zielinski, 2013; Garaba *et al*., 2015). This will also be the case for the new above-water radiometers aboard of the BC Ferries (FOCOS - Ferry Ocean Colour Observation Systems). This feature will make it possible to directly assess the accuracy of various atmospheric correction methods to derive water reflectance needed for biophysical algorithms (Jamet *et al*., 2011; Zibordi, *et al*., 2009).

6.1.2 Chlorophyll

MUMM+SWIR atmospheric corrected method resulted in the best performance for retrievals of *chla*, regardless the match up time frame. Statistically significant correlations were consistently high with R^2=0.55 for 8hrs (n=83 match ups) time difference increasing to R^2=0.69 for 1hr match ups (n=16), and accompanied slopes close to 1.0 - 0.77 and 0.86, respectively. This statistics resulted in the lowest absolute and relative percentage difference compared to the *chla* retrievals using NIR and SWIR products. Both the NIR and SWIR tend to overestimate *in situ chla* observations, and both returned the lowest number of valid retrievals regardless of the match up time. The NIR chl*a* relationship (Figure 10) was generally good, with exception of MODIS chl*a* >~35mg m^{-3}. NIR chl*a* exhibiting extreme values are associated with negligible or negative $R_{rs}(443nm)$ (Figure 11). While the MUMM method specifically removed pixels associated with errors in $R_{rs}(443nm)$, it produced chl*a* estimates in locations where the NIR failed (September 9th, Figure 11).

Since the OC3M *chla* algorithm was implemented for all three methods, the *chla* matchup exercise does not account for contributions of error from the coefficients of the algorithm itself. Empirical blue-green (440-550 nm) band-ratio algorithms such as the OC3M are the most commonly implemented due to their relative simplicity, and phytoplankton absorption is most influential in this spectral region (Blondeau-Patissier *et al*., 2014). This simplicity is useful for the diverse waters in the SoG, providing *chla* estimates under the greatest range of surface-water optical properties (Komick *et al*., 2009). However, we must consider that the increased concentrations of CDOM and total suspended matter in

the waters of the SoG impact the accuracy of the current blue-green ratio algorithms, such as the OC3M, to retrieve *Chla*, as demonstrated for other optically complex waters (Minu *et al*., 2014; Tilstone *et al*., 2013). Generally, for coastal waters, the OC3M algorithm is observed to overestimate retrievals in excess of 100%, particularly at concentrations below 0.2 mg m^{-3} (Komick *et al*., 2009; Radenac, Messié, Léger, & Bosc, 2013; Volpe *et al*., 2007). While values at this magnitude were observed for the IOS and Ricker cruise samples, the majority of *chla* samples were above these concentrations in the SoG since the sampling periods were primarily spring and summer seasons (Table 1) when elevated *chla* is observed. At these seasons, we also generally observe higher levels of both CDOM and TSS due to increased Fraser River discharge (Johannessen *et al*., 2003; Komick *et al*., 2009; Loos & Costa, 2010). Our limited number of *chla*, *aCDOM*(443), and TSS matchups available (n=6, 8 hour temporal difference) show a general positive trend between MODIS derived *chla* residuals to *aCDOM*(443) and TSM, thus suggesting that the bias on the *chla* satellite retrievals is likely is due to optically active water constituents altering ρ_w and therefore the efficacy of the OC3M algorithm. The mean SoG *aCDOM*(443) absorption of 0.47 m^{-1} (range, 0.14-1.16 m^{-1}) and range of TSM (1.49-26.6 mg L^{-1}) is typical of coastal waters such as Beaufort Sea, Chesapeake Bay, and Baltic Sea, where Standard OBPG *chla* algorithms fail (Kirk, 1994; Kowalczuk *et al.*, 2005; Mustapha, Bélanger, & Larouche, 2014; Twardowski & Donaghay, 2001). It is possible CDOM absorption produces negligible R_{rs}(443nm) responsible for data loss in the MUMM method (Figure 11). Further match up data is required to evaluate the cause of bias in the *chla* retrievals. There remains a specific need for methods that produce more accurate retrievals, for example,

regional algorithms, even though our results are statistically in the same range of acceptance as results for other coastal regions of the world (Ahmad *et al*., 2010; Mustapha *et al*., 2014a; Werdell *et al*., 2010).

Regardless of the adopted model approach, global or regional, the in situ *chla* samples are here compared to satellite derived *chla* with spatial resolution of ~1km (at nadir) or less (>1km). There is no provision for the sample itself to be located near the pixel centroid or to evaluate the variability within a 1x1 km. In the SoG, the variability of water optical constituents (Figure 2) (Komick et al., 2009; Loos & Costa, 2010) likely cause sub $1km^2$ variability in absolute chlorophyll concentrations at any given location. Given that the at-sensor radiance is a function of all the optically active properties within the pixel as well as adjacency effects from surrounding pixel-atmosphere interactions (Loisel, 2013), it is reasonable to conclude that a portion of the error in matchups are due to coarse spatial resolution. This is compounded by the evidence that coastal waters, and in particular estuarine systems, are highly variable in time (Cloern, Powell, & Huzzey, 1989; Cloern, 1991; Litaker, Duke, Kenney, & Ramus, 1987). Therefore given the spatial and temporal constraints for the matchups, our results are considered promising given the accuracy that was achieved for the complex coastal system of study.

Aside from our efforts, the most consistent effort for satellite ocean colour *chla* retrieval in the SoG has focused on chlorophyll fluorescence emission centered at 685nm from the MERIS (2002-2012)(Gower, Brown, & Borstad, 2004; Gower & King, 2010), and MODIS (2002-current) (Gower *et al*., 2004; Gower *et al*., 2013) platforms. For these studies, the

fluorescence signal is quantified through a calculation of the Fluorescence Line Height (FLH). FLH is a simple baseline height calculation of the 678nm band above the bounding 667nm and 748nm bands, encompassing the 685nm peak emission wavelength (Gower, Doerffer, & Borstad, 1999; Gower *et al*., 2013; Letelier, 1996). A limited pilot study on the FLH product was conducted for this project for comparison purposes. Here MODIS FLH product was produced from top of atmosphere radiances (Level 1 data) and compared with a subset of IOS *chla* (2003-2005), and visually to the MUMM+SWIR OC3M product. Similar to published studies (Gower *et al.*, 1999; Gower & King, 2010), there was a good agreement (R^2=0.53, n=37, 2hr resolution) to *in situ chla* $\lesssim$25mg m^{-3}. Outliers (n=4) were present when FLH values exceeded 0.0011 $W/m^{-2}/\mu m^{-1}/sr^{-1}$. All outliers were found to be located adjacent to the Fraser River outlet, within the plume. Due to FLH band placement positioning to avoid heavy atmospheric absorption found at ~690nm (oxygen) and ~730nm, atmospheric correction was not critical to acquire a visually clear signal. Whereas OC3M is an empirical relationship of band-ratios to *chla* concentration, the FLH signal describes one of the main deexitation pathways of photosynthesis. Therefore the signal can vary with *chla* concentration, photo-inhibition, phytoplankton species, cell physiology *(Gower et al.*, 2004; Kiefer, 1973). Effective FLH retrieval can be difficult in turbid coastal waters with TSM exceeding >5mg m^{-3} (Gilerson et al., 2008; Moreno-Madriñán & Fischer, 2013) where NIR elastic scattering confounds the signal (Ahmed et al., 2007; Gilerson et al., 2007). While not used in this study, this method produced clear and easily interpretable images of fluorescence distribution as a proxy for phytoplankton

blooms and may be a viable compliment to band-ratio algorithms in optically complex coastal waters.

All derived *chla* and associated timeseries represents the first optical depth, which is defined as the depth where the portion of surface column contributing 90% of water-leaving radiance has a depth, *z*, described by $z = 1/K_d$, where K_d is the diffuse attenuation function for spectral downwelling irradiance (Kirk, 2010; Montes-Hugo *et al*., 2009). This is a major limitation of current remote sensing methods (Mouw & Yoder, 2005) since the chlorophyll maximum layer frequently occurs deeper (Miller, Castillo, & McKee, 2005), and production can extend three times deeper (Morel, 1988). As a result, the top of atmosphere signal from deep chlorophyll maxima (DCM) are not always recorded (Blondeau-Patissier *et al*., 2014; Cullen, 1982; Huisman, Pham Thi, Karl, & Sommeijer, 2006). In Case 1 waters, the optical depth can be relatively invariable over large spatial scales, however in the SoG the optical depth ranges from under a meter to a few meters, exhibiting high spatial variability (Loos & Costa, 2010). The considerations of a variable first optical depth and uneven depth integrated chlorophyll are twofold. First, the time series for the North and Central regions (Figure 13) represent chlorophyll concentrations that may be derived from different absolute depths. Here optically simpler waters in the north may contain signal from slightly deeper chlorophyll when compared to highly attenuating waters under the Fraser River plume. Secondly, since HPLC sampling was conducted at 3m depth, which would not always correspond to the DCM. Both considerations may have introduced errors propagated through to the matchup analysis.

6.2 Phytoplankton blooms

Successful marine resource management requires an understanding of ecosystem dynamics and controls (Chassot et al., 2010). For the SoG, the controls of productivity to higher trophic levels have been recently evaluated in the Ecosystem Research Initiative, summarized in Masson & Perry, (2013) and Perry & Masson, (2013). This research initiative, among others has highlighted the need to properly characterize primary production and its forcing effects for SoG fisheries management (e.g., Schweigert *et al*., 2013 ;Beamish *et al*., 2010; Ji, Edwards, Mackas, Runge, & Thomas, 2010; Preikshot, Beamish, & Neville, 2013; Riche, Johannessen, & Macdonald, 2014; Thomson et al., 2012). Aside from basic food availability to higher trophic levels, the spring phytoplankton phenology (initiation time, peak, end, duration) affects the biogeochemical status for the SoG through removal of available nutrients, the conversion of CO_2 and H^+ ions into organic matter, and in the process, release of O_2 (Riche *et al.*, 2014). By studying phytoplankton phenology through techniques that allow for larger scale analysis such as remote sensing a better understanding of these processes may be realized in the SoG.

The results of this study show that the annual *chla* dynamic in the SoG rarely exhibits one clear seasonal mode of variability (Figure 13). Instead *chla* levels are characterized by elevated and variable concentrations in the spring, summer, and fall, and lower concentrations in the winter, similar to findings by other research for this region (Halverson & Pawlowicz, 2013; Masson & Peña, 2009; Schweigert et al., 2013). The 14

years *chla* time series shows that *chla* concentration are generally lower in the winter (November through February) when concentration are on average 1.5mg m^{-3} and 3.1mg m^{-3} for the North and Central regions, respectively (Figure 12). Spring, summer and fall show average concentrations ranging 3.0-6.0 mg m^{-3} and 4.0-9.5 mg m^{-3} for the North and Central region, respectively. In general the months with highest concentrations are April through June. High variability in *chla* concentrations reported here and in several other near-shore productivity studies can be generally attributed to disruptions of the bloom formation due to physical events (Erga & Heimdal, 1984; Sournia, Birrien, Douvillé, Klein, & Viollier, 1987; Yin, Harrison, Goldblatt, & Beamish, 1996). This is in contrast to the typical one dominant mode of *chla* variability mostly observed in temperate, open ocean water (Cloern, 1996).

The relative simplicity of phytoplankton phenology for open ocean temperate waters makes it easier to model. For example, Platt *et al*., (2009) and Zhai, Platt, Tang, Sathyendranath, & Hernandez Walls, (2011) successfully demonstrated that a shifted Gaussian function can be applied to a time-series of satellite derived *chla* products to derive phenological indices for the Scotian shelf. In temperate case 1 waters phytoplankton variability is generally forced by annual cycles of solar radiation (Sverdup, 1953), in coastal/estuarine waters productivity is shaped by interactions with land, open-ocean, a more complex atmosphere, and more variable marine biogeochemical state (Cloern, 1996). In coastal waters such as the SoG, considerations in regard to the different methods used to define phytoplankton phenology is of great importance. For instance, the spatial and temporal scales of the data, the employed bloom definition method

(Brody *et al*., 2013) and definition of phytoplankton blooms (Blondeau-Patissier *et al*. 2014), in part, dictates how the bloom phenology is characterized (Rantajarvi, 1998).

For the SoG, several studies have estimated bloom phenology based on a coupled biophysical model which indicates the bloom initiation day based on nutrient depletion and physical forcing (Allen & Wolfe, 2013; Sprules *et al.*, 2009), *chla* timeseries from discrete sampling *(Pawlowicz et al*., 2003), and from *chla* fluorescence sensors aboard ferries on regular routes in the central SoG (Halverson & Pawlowicz, 2013). Synoptic spatial-temporal estimates from ocean colour satellites have also been reported using different scales and methods (Gower *et al*., 2013; Gower & King, 2010; Jackson, Thomson, Brown, Willis, & Borstad, 2015; Schweigert *et al*., 2013). Gower *et al.,* (2013) take advantage of the fluorescence signal centered at 685nm using 300m MERIS, and 1km MODIS spatial resolutions. Jackson *et al*., (2015) and Schweigert *et al*., (2013) rely on the standard MODIS NIR product using OC3M, reduced spatial resolutions (9km), and consider the SoG as a single region. These authors define YD_{init} as the time when *chla* exceeds a threshold of $6.0mg^{-3}$. However, Schweigert *et al*., (2013) has the additional provision to define YD_{init} when *chla* reaches the annual median plus 5% for two consecutive weeks, similar to Siegel *et al*., (2002). The approach used in this study is similar to Schweigert's method, but a distinct method was applied to generate the input satellite products and geographical thresholds to define YD_{init}.

Generally, previous studies derive only one value of bloom initiation for the whole SoG of each year, which assumes a single physical and biogeochemical regime for the study area.

The northern waters, however, differ in water movement (Halverson & Pawlowicz, 2008; Masson & Cummins, 2004), residence time (Waldichuk, 1957), and biological and optical characteristics when compared to the Fraser River influenced parts of the Central region (Hoff et al., 1997; Loos & Costa, 2010). Therefore, it is reasonable to assume different bloom phenology between these areas. Time-series results of this study support this assumption as there is an average magnitude difference of 2.0mg m^{-3} for *chla* between the two regions, North and Central, and often differences in YD_{init} and YD_{dur} (Table 5).

Our bloom phenology results are compared with two different studies also focused on bloom phenology in the SoG, Allen & Wolfe (2013) and Gower *et al.,* 2013 (Table 5 & Figure 14). The first is a one-dimensional coupled biophysical model composed of a modified near-surface mixing model coupled with nitrate-phytoplankton biological model (Allen & Wolfe, 2013; Sprules et al., 2009). *In situ* wind, temperature, cloud fraction, and Fraser River discharge data force this model. The bloom timing is defined as the time of highest concentration of phytoplankton unless an earlier bloom (≥4 days earlier) was associated with nitrate levels going below 0.5 µM. The authors define the average YD_{init} as March 24 (day 84, ±4 days) according to 42 years considered in the analysis (1968-2010). The results from our time-series analysis (2003-2014) for the Central region indicated YD_{init} as March 28 (day 88, ±4 days). For the analysed years, we observed agreement in bloom timing (YD_{init}) for seven out of 12 years, within the ±4 day bounds with Allen & Wolfe (2013). Our method produced a single estimate that was later than the hindcast model (2003, +7 days), and four years where the method produced slightly earlier YD_{init} (2004, 2005, 2009, 2012). Of these, 2004, 2005, and 2012 exhibited very small

differences of 3, 1, and 5 days, respectively, while 2009 exhibited the largest difference; our approach defined the start of the bloom 20 days earlier in 2009 (Table 5). While we cannot exclude an earlier YD_{init} for 2009, we found that a large bloom event happened in the Northern region (YD_{init} =97), similar to timing of the hindcast modelling (Table 5). The high *chla* concentrations at this time was also observed in the Central region, but was preceded by two smaller events in March that resulted in the earlier YD_{init} as defined by our method.

Comparison of our YD_{init} for the North region with the hindcast model shows larger difference; only 4 years of the hindcast model exhibited similar YD_{init}. Three of these estimates, however, correspond to the same YD_{init} observed in Central region. The resulting discrepancy for the North region compared with the model may be best explained by the forcing data used in the model itself. The forcing data for the hindcast model is representative of the Central region of the SoG, located between Nanaimo and Vancouver (approximately station "S3" of Figure 1 in Allen & Wolfe, 2013), with the majority of forcing data used from Sands Head and YVR, both in proximity to the Fraser River (Allen & Wolfe, 2013). It is plausible that if the hindcast predictions were performed using forcing data from the North region, YD_{init} may better coincide.

The second major study, for comparison with our bloom phenology results, uses the FLH algorithm to define *chla* concentrations (Gower *et al*., 1999; Gower *et al*., 2013). The authors define bloom initiation as the day in which the MODIS-retrieved fluorescence signal corresponds to chlorophyll concentrations of $5.0mg^{-3}$ or higher and covers >30% of

the SoG (Gower *et al*., 2013). According to data for the years 2003-2011, Gower *et al.,* (2013) define February 29 (Day 60) and March 27 (day 87) as average bloom initiation days for the SoG when inlet blooms are observed versus when inlet blooms ("Malaspina Dragon") appear inactive, respectively. When compared to FLH results by Gower *et al*., (2013), our YD_{init} estimates coincided mostly with inlet-inactive blooms conditions, and were in general after the YD_{init} defined by the FLH approach; on average 15 days later for the Central region and 9 days later in the Northern region (Table 5). Differences between applied approaches may have resulted in the observations. This study for example, excluded images acquired before February 18 of each year to avoid atmospheric correction failure from large solar zenith angles (>75°) (Ding & Gordon, 1994) whereas Gower *et al*. (2013) included earlier year images. Pixels with high zenith angles are flagged and removed to improve data quality at the expense of complete temporal coverage (Darecki & Stramski, 2004; Gregg & Casey, 2007). Other instances of early blooms, however, including the unusually early bloom that occurred in February of 2005 as reported in both Allen and Wolfe (2013) (Day 62) and Gower *et al*. (2013) (day 56) is confirmed through this study (Central = 53, North = 49, respectively). Further, discrepancies in our results compared to the Gower *et al* approach could be a result of further differences between the two methods. Notwithstanding an observed good relationship of FLH to *in situ* surface *chla* concentration lower than 20.0mg m^{-3} (Gower & King, 2010), several method differences such as, the physical phenomena being observed, atmospheric corrections, regions definition, daily vs. binned products, and different methods for definitions of bloom initiation all likely contribute to observed differences.

Although the SoG was divided into North and Central regions, there remains the possibility of bias from the definition of the extents of the regions themselves through the modifiable areal unit problem (MAUP) versus a pixel by pixel analysis (Fotheringham & Wong, 1991). Different definitions of region spatial extents and associated spatial phytoplankton phenology variability would ultimately change median weekly values recorded, especially in instances of few pixels. This could be the case for studies including Gower *et al*., 2013, 2010; Jackson *et al*., 2015; Schweigert *et al*., 2013, where the SoG is treated as one region to derive bloom timing, and ours even if we treated the SoG as two regions to derive phenology. Further, spatial restraints related to the exclusion of small inlets and island chains which are too fine scale to be included in the analysis due to the spatial resolution of the MODIS images. Our methods specifically excluded *chla* estimates from the major coastal inlets and island chains. The smaller spatial scales and increased optical complexity made it unrealistic to acquire imagery for these locations. Excluding these regions could be an important consideration as productivity here can range in excess of 500g C m^{-2} annually (Stockner, Cliff, & Shortreed, 1979; Timothy & Soon, 2001), and seeding events from these regions may mediate seasonal blooms as a whole (Gower *et al*., 2013). More research is needed to better understand the existence of possible seeding events and the issue with spatial resolution of ocean colour imagery.

The temporal definition of the binned period is critical as it can also alter the derived phenology indices. If the time definition is too narrow , for instance, daily, shorter duration *chla* events can add noise and precede the first significant spring bloom., If the binned time period is too broad, for instance, monthly, temporal difference may be lost.

To test whether the OBPG standard 8-day binned period was a reasonable representation for the SoG, we compared the *chla* 8-day binned products to *chla* fluorescence data acquired from the ferry (MV Spirit of Vancouver Island) that transects the Southern region daily (Jim Gower, personal communication). When *chla* ferry data was aggregated to the same extent (5km x 5km ROI) and temporal period (8-days), the matchups with our data showed a general agreement in bloom trends regardless of the fact it was a comparison between two different phytoplankton processes to quantify chlorophyll, and compared track-line to pixel-area. Degrading temporal resolution to ~8 days for spatial binning is a useful method, therefore, when there is a lack of complete and consistent ocean colour product for the SoG. The OBPG 8 day binning procedure was found to be appropriate for the SoG.

Different definitions used to derive phenology would alter results for the SoG. As recently presented in Blondeau-Patissier *et al.*, (2014), bloom phenology techniques consist of two broad approaches. The first approach is based on a time-domain signal processing, which analyzes the data series in the same temporal resolution it is observed. The shifted Gaussian modelling method (Platt et al., 2009; Zhai et al., 2011), and the modified Siegel *et al*., (2002) method investigated for our study fall into this category. Time-domain processing tends to require a certain level of *a priori* knowledge of general bloom dynamics for a study region. The exercise then is to find appropriate modelling technique to be able to derive meaningful phenology statistics. Our adopted modified Siegel's method holds constant the *chla* concentration threshold both inter-annually and spatially to define bloom initiation.

In contrast, the second approach consists of mixed time-frequency domain methods, which is based on the decomposition of a data series into different time and scale frequencies. Here the signal is decomposed into the closest fitting sinusoidal waves of high and low frequencies that reveal temporal features in noisy time-series, where knowledge of a bloom may be *a posteriori*. This approach was evaluated for our data series and found to be incompatible with the high variability in *chla* concentrations (Section 3.5).

In light of inherent difficulties in modelling highly variable *chla* time-series, several simple quantitative definitions of bloom phenology have been used. The use of annual median +5% to define YD_{init} proposed by Siegel et al. (2002) has most frequently been used in lieu of other time-domain methods (Henson, Dunne, & Sarmiento, 2009; Henson & Thomas, 2007; Racault, Le Quéré, Buitenhuis, Sathyendranath, & Platt, 2012). As part of a study comparing YD_{init} methods, Brody, Lozier, & Dunne (2013) compared the HANTS algorithm to the Siegel *et al*. (2002) threshold method for oceanic locations in the North Atlantic. Similar to our study, their findings indicate that using the threshold method, YD_{init} occurs during or immediately after the largest increases in *chla* concentration. Furthermore, they found HANTS fitting probably negatively affected certain YD_{init} estimates, and required interpolated data for missing values. The modified Siegel *et al*. (2002) threshold used here produced YD_{init} similar to Allen and Wolfs' hindcast model, thus indicating its usefulness for identifying the initiation of the first significant spring bloom in the SoG. With the advent of the VENUS/ONC ferry box data (Taylor, 2009; Woodroffe & Round, 2008), acquiring *chla* and complimentary data including dissolved O_2 from a ferries that transects

both North and Central SoG (Wang, 2015) we will be able in the future to better define in conjunction with satellite derived chla the bloom timing and exhaustion in relation to the SoG biogeochemical status. Further investigation on the association of the approach applied in our study and the approach by Gower *et al.* (2013) will likely result in increased accuracy of using satellite data for bloom phenology in the Salish Sea.

Most focus of ocean color bloom studies is ascribed to YD_{init} estimates, with the assumption that this phenology metric is the time when there can be a match of biomass to higher trophic levels at critical periods (Allen & Wolfe, 2013; Platt et al., 2003; Riche et al., 2014; Schweigert et al., 2013; Zhai et al., 2011). YD_{init} has been discussed as an important potential input to investigate fishery stock health and recruitment (Cushing, 1990) because of this assumption. Unfortunately, YD_{init} does not describe the trophic coupling, but rather the first available time this could occur within a calendar year. For the first time, we are providing the duration (YD_{dur}) and timing of maxima (YD_{max}) estimates for two regions in the SoG, which describe potential duration of coupling and time of maximum availability of phytoplankton to higher trophic levels. For the SoG and surrounding waters, zooplankton stocks can lower levels of phytoplankton through grazing, thereby coupling biomass to higher trophic levels (Garay & Soberanis, 2008; Strom *et al.*, 2001; Tommasi *et al*., 2013). A theoretical coupling metric would require detailed information on the composition and fate of present phytoplankton during the spring bloom, as well as composition, grazing rates and metabolism of zooplankton assemblages.

In lieu of a coupling metric from bloom phenology, the HCA provides information of similar versus dissimilar spring bloom time series. In particular, identification of phenological clustering may provide insight into forcing mechanisms of the SoG. The results indicate a very similar spring bloom phenology of north and south for 2009 and 2012, while 2008 is by comparison atypical (Figure 15). Given an appropriately complete set of both fisheries stock metrics and ocean color series, it would be possible to relate stock status condition in terms of phenology membership of bloom series. This study was constrained to a relatively short time-series (2003-2014), however, D'Ortenzio et al., (2012) have demonstrated that HCA can be applied to multiple ocean color missions (e.g. CZCS – Sentinel-3) to determine how regional phenology membership changes over time. In Allen & Wolfe (2013) hindcast modelling, no strong correlation of modelled YD_{dur} to large scale indices including Pacific decadal oscillation (PDO), and North Pacific gyre oscillation (NPGO) were found. A longer imagery time-series derived from historical and current platforms would facilitate the investigation bloom phenology in relation to larger scale processes including climate variability patterns.

Chapter 7 - Conclusion

The goal of this thesis was to derive phytoplankton bloom phenology for the Strait of Georgia, Canada, by validating three MODIS atmospheric correction schemes, and using the most accurate to build a timeseries of OC3M *chla* derived products. To accomplish this goal, *in situ* optical measurements (Å, $\tau_a(\lambda)$, $\mathrm{R_{RS}}(\lambda)$) and discrete sampling for biophysical constituents (*chla*, TSM, CDOM) were analyzed at various locations in the SoG in respect to the NIR, SWIR, and MUMM+SWIR atmospheric corrections. The MUMM+SWIR approach was used to construct a weekly-binned timeseries from 2002-2014, from which spring phenology indices (YD_{init}, YD_{max}, YD_{dur}) were derived. Finally, similarity of spring bloom trends between years were investigated using hierarchical clustering analysis as an attempt to isolate anomalous conditions.

Compared to *in situ* AERONET site located in the southern extent of the SoG, the MUMM method that uses an aerosol model defined from the Central region works nearly as well as the NIR black pixel assumption to define $\tau_a(\lambda)$ and wavelength dependence (Å). This partly supports the assumption of aerosol type spatial homogeneity for the MUMM correction. The SWIR correction produced erroneous $\tau_a(\lambda)$, Å, and ultimately, *chla* distributions attributed to the very low SNR of the 1240nm and 1640nm bands. MUMM+SWIR failed to resolve fine mode fraction Å when compared to NIR. This indicates that in at least certain instances, the definition of an aerosol model from northern waters is inappropriate as it neglects the influence of strongly absorbing urban aerosols.

When compared to radiometric ($R_{RS}(\lambda)$) and *chla* samples collected from broader water and atmospheric conditions throughout the SoG, the MUMM+SWIR performed the best. This was attributable to more similar $R_{RS}(\lambda)$ when compared to *in situ* HyperSAS measurements, specifically for the bands used to calculate reflectance ratio in the OC3M *chla* algorithm. The effect of MUMM+SWIR correction is more consistent *chla* distribution products that show less anomalously high *chla* regions. While the findings suggest the MUMM+SWIR performs better in waters where the black pixel assumption fails, a major limitation of this study is the small number of viable matchups of $R_{RS}(\lambda)$ to compare atmospheric correction methods, over a broad range of waters with varying optical constituents (TSM, CDOM). The MUMM+SWIR approach, as used in this study, was best at determining *in situ chla* concentrations, being superior to the standard OBPG approach. It exhibited consistently low APD, bias, and residuals when compared to the other methods. Most importantly, it was the only method exhibiting increased correlation (0.69) and slope closer to 1.0 (0.89) with finer temporal differences. Given the dynamic nature of the water mass, phytoplankton, and physical inputs (Fraser River) this was a reasonably effective method to determine *chla* as a proxy for phytoplankton.

There was good agreement of MUMM+SWIR bloom initiation when compared to a coupled biophysical forcing model (Allen & Wolfe, 2013) and A MODIS algorithm relying on chlorophyll photosynthesis to produce fluorescence (Gower et al., 2013; Gower & King, 2010). Results indicate Central SoG start dates range from late February to late April, with an average start date at the last week of March. These results compare favorably to Hindcast predictive modelling of bloom start dates. The North bloom phenology starts on

average 9 days earlier, and experiences lower chlorophyll-*a* magnitudes. Differences between methods can be partly explained through differences in spatial considerations and the biophysical phenomena used to estimate phytoplankton blooms. YD_{init} results for the Northern region better coincide with Gower *et al* (2013) during years the authors identify the "Malaspina Dragon" occurring, when there is evidence of inlet seeding YD_{init}. This study added further phenology metrics of time of maximum *chla* and a duration of the largest spring phytoplankton bloom as potential diagnostic tools for other studies. While there is no discernable Gaussian distribution of *chla* over time, a spring season is identifiable through the definition of YD_{dur}. When compared to all years, 2007 is unique in it's later than average start date paired with an extreme YD_{dur}. HCA allowed the comparison of similarity of spring bloom timeseries for both the North and Central regions of the SoG. Our results indicate that 2009 and 2012 were most similar, while 2008 was least correlated to any other season, as evident in the shapes of the timeseries. Despite HCA determined similarity, 2009 & 2012 did not show similarYD_{init}, YD_{max} or YD_{dur}. At present, there is no mechanistic explanation of underlying biophysical drivers for similarly grouped HCA members. This could be attempted, however, with a longer timeseries of data-merged products from past and present ocean color sensors. Chlorophyll concentrations are highly variable both spatially and temporally for the SoG, making determination of the spring phytoplankton phenology difficult when relying on modelling methods designed for simpler systems. For the SoG, where variability is attributed to short duration physical forcing, established phenology methods are inappropriate as no Gaussian distribution of phytoplankton biomass exists over the times investigated. The

variability can be simplified into more interpretable ‘weekly’ binned composites that provide useful information on seasonal dynamics.

Our study highlights the ongoing need for improved ocean color sensor temporal, spatial, and radiometric resolutions. In particular, improving the SNR of SWIR detectors may prove invaluable for atmospheric correction in the highly turbid regions present in the SoG. While assuming a homogenous aerosol type produces generally better results than the standard NIR over a broad range of waters, more work is needed to produce accurate pixel-level models for ocean color.

8. Bibliography

Abbas, A. a., Mansor, S. B., Pradhan, B., & Tan, C. K. (2012). Spatial and seasonal variability of Chlorophyll-a and associated oceanographic events in Sabah water. *Proceedings of the 2nd International Workshop on Earth Observation and Remote Sensing Applications, EORSA 2012*, (July 2002), 215–219. http://doi.org/10.1109/EORSA.2012.6261168

Ahmad, Z., Franz, B. A., McClain, C. R., Kwiatkowska, E. J., Werdell, J., Shettle, E. P., & Holben, B. N. (2010). New aerosol models for the retrieval of aerosol optical thickness and normalized water-leaving radiances from the SeaWiFS and MODIS sensors over coastal regions and open oceans. *Applied Optics*, *49*(29), 5545–5560.

Ahmed, S., Gilerson, A., Harmel, T., Hlaing, S., Tonizzo, A., Weidemann, A., & Arnone, R. (2012). Evaluation of atmospheric correction procedures for ocean color data processing using hyper-and multi-spectral radiometric measurements from the Long Island Sound Coastal Observatory. In *SPIE Defense, Security, and Sensing* (p. 83720M–83720M–14). International Society for Optics and Photonics.

Ahmed, S., Gilerson, A., Zhou, J., Hlaing, S., Ioannou, I., Jerez, W., … Moshary, F. (2007). <title>Impact of scattering and absorption of photosynthetic pigments on fluorescence retrieval algorithms for coastal waters</title>. In C. R. Bostater, Jr., S. P. Mertikas, X. Neyt, & M. Vélez-Reyes (Eds.), *REMOTE SENSING OF THE OCEAN, SEA ICE, AND LARGE WATER REGIONS 2007* (Vol. 6743, pp. 674307–674307–11). SPIE-INT SOC OPTICAL ENGINEERING, 1000 20TH ST, PO BOX 10, BELLINGHAM, WA 98227-0010 USA. http://doi.org/10.1117/12.737431

Allen, S. E., & Wolfe, M. A. (2013). Hindcast of the timing of the spring phytoplankton bloom in the Strait of Georgia, 1968-2010. *Progress in Oceanography*, *115*, 6–13. http://doi.org/10.1016/j.pocean.2013.05.026

Ångström, A. (1964). The parameters of atmospheric turbidity. *Tellus*, *16*(1), 64–75. http://doi.org/10.1111/j.2153-3490.1964.tb00144.x

Arar, E. J. (1997). *Method 447.0: Determination of Chlorophylls a and B and Identification of Other Pigments of Interest in Marine and Freshwater Algae Using High Performance Liquid Chromatography with Visible Wavelength Detection*. United States Environmental Protection Agency, Office of Research and Development, National Exposure Research Laboratory.

Bailey, S. W., Franz, B. A., & Werdell, P. J. (2010). Estimation of near-infrared water-leaving reflectance for satellite ocean color data processing. *Optics Express*, *18*(7), 7521–7527.

Bailey, S. W., & Werdell, P. J. (2006). A multi-sensor approach for the on-orbit validation of ocean color satellite data products. *Remote Sensing of Environment*, *102*(1), 12–23.

Beamish, R. J., Neville, C., Sweeting, R., & Lange, K. (2012). The Synchronous Failure of Juvenile Pacific Salmon and Herring Production in the Strait of Georgia in 2007 and the Poor Return of Sockeye Salmon to the Fraser River in 2009. *Marine and Coastal Fisheries*, *4*(1), 403–414. http://doi.org/10.1080/19425120.2012.676607

Beamish, R. J., Sweeting, R. M., Lange, K. L., Noakes, D. J., Preikshot, D., & Neville, C. M. (2010). Early Marine Survival of Coho Salmon in the Strait of Georgia Declines to Very Low Levels. *Marine and Coastal Fisheries*, *2*(1), 424–439. http://doi.org/10.1577/C09-040.1

Blondeau-Patissier, D., Gower, J. F. R., Dekker, A. G., Phinn, S. R., & Brando, V. E. (2014). A review of ocean color remote sensing methods and statistical techniques for the detection, mapping and analysis of phytoplankton blooms in coastal and open oceans. *Progress in Oceanography*, *123*, 123–144. http://doi.org/10.1016/j.pocean.2013.12.008

Bokoye, A. I., Royer, A., O'Neil, N. T., Cliche, P., Fedosejevs, G., Teillet, P. M., & McArthur, L. J. B. (2001). Characterization of atmospheric aerosols across Canada from a ground-based sunphotometer network: AEROCAN. *Atmosphere-Ocean*, *39*(4), 429–456.

British Columbia Gov. (2011). *Comprehensive GNSS Technology training for Resource Mapping: Quality assurance and Quality Control Procedures*. *Integrated Land Management Bureau Archive*. Retrieved from http://geobc.gov.bc.ca/base-mapping/atlas/gsr/courses/pdf/M04_v2011_final.pdf

Brody, S. R., Lozier, M. S., & Dunne, J. P. (2013). A comparison of methods to determine phytoplankton bloom initiation. *Journal of Geophysical Research: Oceans*, *118*(5), 2345–2357. http://doi.org/10.1002/jgrc.20167

Campbell, J. W. (1995). The lognormal distribution as a model for bio-optical variability in the sea. *Journal of Geophysical Research: Oceans (1978–2012)*, *100*(C7), 13237–13254.

Campbell, J. W., Blaisdell, J. M., & Darzi, M. (1995). Volume 32 , Level -3 SeaWiFS Data Products : Spatial and Temporal Binning Algorithms. *SeaWiFS Technical Report Series*, *32*(August).

Chassot, E., Bonhommeau, S., Dulvy, N. K., Mélin, F., Watson, R., Gascuel, D., & Le Pape, O. (2010). Global marine primary production constrains fisheries catches. *Ecology Letters*, *13*(4), 495–505. http://doi.org/10.1111/j.1461-0248.2010.01443.x

Chen, J., Quan, W., & Cui, T. (2015). A Multi-Band Semi-Analytical Algorithm for Estimating Chlorophyll-a Concentration in the Yellow River Estuary, China. *Water Environment Research*, *87*(1), 44–51. http://doi.org/10.2175/106143014X14062131179032

Chen, J., Zhang, M., Cui, T., & Wen, Z. (2013). A review of some important technical problems in respect of satellite remote sensing of chlorophyll-a concentration in coastal waters. *Selected Topics in Applied Earth Observations and Remote Sensing, IEEE Journal of*, *6*(5), 2275–2289.

Cloern, J. E. (1991). Tidal stirring and phytoplankton bloom dynamics in an estuary. *Journal of Marine Research*, *49*(1), 203–221. http://doi.org/10.1357/002224091784968611

Cloern, J. E. (1996). Phytoplankton bloom dynamics in coastal ecosystems: A review with some general lessons from sustained investigation of San Francisco Bay, California. *Reviews of Geophysics*, *34*(2), 127. http://doi.org/10.1029/96RG00986

Cloern, J. E., Powell, T. M., & Huzzey, L. M. (1989). Spatial and temporal variability in South San Francisco Bay (USA). II. Temporal changes in salinity, suspended sediments, and phytoplankton biomass and productivity over tidal time scales. *Estuarine, Coastal and Shelf Science*, *28*(6), 599–613. http://doi.org/10.1016/0272-7714(89)90049-8

Cullen, J. J. (1982). The Deep Chlorophyll Maximum: Comparing Vertical Profiles of Chlorophyll a. *Canadian Journal of Fisheries and Aquatic Sciences*, *39*(5), 791–803. http://doi.org/10.1139/f82-108

Cushing, D. H. (1990). Plankton production and year class strength in fish populations - an update of the match mismatch hypothesis. *Advances in Marine Biology*, *26*, 249–293.

D'haeseleer, P. (2005). How does gene expression clustering work? *Nature Biotechnology*, *23*(12), 1499–1501. http://doi.org/10.1038/nbt1205-1499

D'Ortenzio, F., Antoine, D., Martinez, E., & Ribera d'Alcalà, M. (2012). Phenological changes of oceanic phytoplankton in the 1980s and 2000s as revealed by remotely sensed ocean-color observations. *Global Biogeochemical Cycles*, *26*(4), n/a–n/a. http://doi.org/10.1029/2011GB004269

Darecki, M., & Stramski, D. (2004). An evaluation of MODIS and SeaWiFS bio-optical algorithms in the Baltic Sea. *Remote Sensing of Environment*, *89*(3), 326–350. http://doi.org/10.1016/j.rse.2003.10.012

Ding, K., & Gordon, H. R. (1994). Atmospheric correction of ocean-color sensors: effects of the Earth's curvature. *Applied Optics*, *33*(30), 7096–7106.

Dixon, W. J. (1953). Processing data for outliers. *Biometrics*, *9*(1), 74–89.

Dogliotti, A. I., Ruddick, K., Nechad, B., & Lasta, C. (2011). Improving water reflectance retrieval from MODIS imagery in the highly turbid waters of La Plata River. In *Proceedings of VI International Conference "Current Problems in Optics of Natural Waters*.

Doxaran, D., Cherukuru, N., & Lavender, S. J. (2006). Apparent and inherent optical properties of turbid estuarine waters: measurements, empirical quantification relationships, and modeling. *Applied Optics*, *45*(10), 2310. http://doi.org/10.1364/AO.45.002310

Drinkwater, M., & Rebhan, H. (2005). Sentinel-3: Mission Requirements Document. *Final Report: Reference EOP-SMO/1151/MD-Md (*. http://doi.org/19/02/2007

Eck, T. F. (2005). Columnar aerosol optical properties at AERONET sites in central eastern Asia and aerosol transport to the tropical mid-Pacific. *Journal of Geophysical Research*, *110*(D6), D06202. http://doi.org/10.1029/2004JD005274

Eck, T. F., Holben, B. N., Reid, J. S., Dubovik, O., Smirnov, A., O'neill, N. T., … Kinne, S. (1999). Wavelength dependence of the optical depth of biomass burning, urban, and desert dust aerosols. *Journal of Geophysical Research: Atmospheres (1984–2012)*, *104*(D24), 31333–31349.

Edwards, D. P. (2004). Observations of carbon monoxide and aerosols from the Terra satellite: Northern Hemisphere variability. *Journal of Geophysical Research*, *109*(D24), D24202. http://doi.org/10.1029/2004JD004727

Erga, S. R., & Heimdal, B. R. (1984). Ecological studies on the phytoplankton of Korsfjorden, western Norway. The dynamics of a spring bloom seen in relation to hydrographical conditions and light regime. *Journal of Plankton Research*, *6*(1), 67–90. http://doi.org/10.1093/plankt/6.1.67

Forget, M.-H., Stuart, V., & Platt, T. (2009). *Reports and Monographs of the International Ocean-Colour Coordinating Group Remote Sensing in Fisheries and Aquaculture*. *Aquaculture*.

Fotheringham, A. S., & Wong, D. W. S. (1991). The modifiable areal unit problem in multivariate statistical analysis. *Environment and Planning A*, *23*(7), 1025–1044. http://doi.org/10.1068/a231025

Franz, B. A., Bailey, S. W., Meister, G., & Werdell, P. J. (2012). Quality and consistency of the NASA ocean color data record. *Proc.Ocean Optics XXI, Glasgow, Scotland*, 8–12.

Franz, B. A., Werdell, P. J., Meister, G., Bailey, S. W., Eplee Jr, R. E., Feldman, G. C., … Thomas, D. (2003). The continuity of ocean color measurements from SeaWiFS to MODIS. *Earth Observing Systems X, SPIE*, 1–13.

Franz, B. A., Werdell, P. J., Meister, G., Kwiatkowska, E. J., Bailey, S. W., Ahmad, Z., & McClain, C. R. (2006). MODIS Land Bands for Ocean Remote Sensing Applications. In *Ocean optics XVIII*.

Fraser, R. S., & Kaufman, Y. J. (1985). The Relative Importance of Aerosol Scattering and Absorption in Remote Sensing. *IEEE Transactions on Geoscience and Remote Sensing*, *GE-23*(5). http://doi.org/10.1109/TGRS.1985.289380

Garaba, S. P., Voß, D., Wollschläger, J., & Zielinski, O. (2015). Modern approaches to shipborne ocean color remote sensing. *Applied Optics*, *54*(12), 3602. http://doi.org/10.1364/AO.54.003602

Garaba, S. P., & Zielinski, O. (2013). Methods in reducing surface reflected glint for shipborne above-water remote sensing. *Journal of the European Optical Society: Rapid Publications*, *8*, 13058. http://doi.org/10.2971/jeos.2013.13058

Garay, M. J. H., & Soberanis, L. H. (2008). Dominance shift of zooplankton species composition in the central Strait of Georgia, British Columbia during 1997. *Hidrobiológica*, *18*(Su1), 53–60. Retrieved from http://www.redalyc.org/articulo.oa?id=57809808

Gilerson, A., Zhou, J., Hlaing, S., Ioannou, I., Amin, R., Gross, B., … Ahmed, S. (2007). <title>Fluorescence contribution to reflectance spectra for a variety of coastal waters</title>. In R. J. Frouin (Ed.), *Optical Engineering + Applications* (p. 66800C–66800C–12). International Society for Optics and Photonics. http://doi.org/10.1117/12.731663

Gilerson, A., Zhou, J., Hlaing, S., Ioannou, I., Gross, B., Moshary, F., & Ahmed, S. (2008). Fluorescence Component in the Reflectance Spectra from Coastal Waters. II. Performance of retrieval algorithms. *Optics Express*, *16*(4), 2446. http://doi.org/10.1364/OE.16.002446

Gordon, H. R., & Castaño, D. J. (1989). Aerosol analysis with the Coastal Zone Color Scanner: a simple method for including multiple scattering effects. *Applied Optics*, *28*(7), 1320–1326.

Gordon, H. R., & Clark, D. K. (1981). Clear water radiances for atmospheric correction of coastal zone color scanner imagery. *Applied Optics*, *20*(24), 4175. http://doi.org/10.1364/AO.20.004175

Gordon, H. R., & Voss, K. J. (1999). MODIS normalized water-leaving radiance algorithm theoretical basis document. *NASA Technical Report Series, NAS5-31363*.

Gordon, H. R., & Wang, M. (1994). Retrieval of water-leaving radiance and aerosol optical thickness over the oceans with SeaWiFS: a preliminary algorithm. *Applied Optics*, *33*(3), 443–452.

Gower, J. F. R., Brown, L., & Borstad, G. a. (2004). Observation of chlorophyll fluorescence in west coast waters of Canada using the MODIS satellite sensor. *Canadian Journal of Remote Sensing*, *30*(1), 17–25. http://doi.org/10.5589/m03-048

Gower, J. F. R., Doerffer, R., & Borstad, G. a. (1999). Interpretation of the 685nm peak in water-leaving radiance spectra in terms of fluorescence, absorption and scattering, and its observation by MERIS. *International Journal of Remote Sensing*, *20*(March 2015), 1771–1786. http://doi.org/10.1080/014311699212470

Gower, J., & King, S. (2010). Validation of chlorophyll fluorescence derived from MERIS on the west coast of Canada. *International Journal of Remote Sensing*. Retrieved from http://www.tandfonline.com/doi/abs/10.1080/01431160600821010

Gower, J., King, S., Statham, S., Fox, R., & Young, E. (2013). The Malaspina Dragon: A newly-discovered pattern of the early spring bloom in the Strait of Georgia, British Columbia, Canada. *Progress in Oceanography*, *115*, 181–188. http://doi.org/10.1016/j.pocean.2013.05.024

Goyens, C., Jamet, C., & Schroeder, T. (2013). Evaluation of four atmospheric correction algorithms for MODIS-Aqua images over contrasted coastal waters. *Remote Sensing of Environment*, *131*, 63–75. http://doi.org/10.1016/j.rse.2012.12.006

Gregg, W. W., & Casey, N. W. (2007). Sampling biases in MODIS and SeaWiFS ocean chlorophyll data. *Remote Sensing of Environment*, *111*(1), 25–35. http://doi.org/10.1016/j.rse.2007.03.008

Hale, G. M., & Querry, M. R. (1973). Optical constants of water in the 200-nm to 200-µm wavelength region. *Applied Optics*, *12*(3), 555–563.

Halverson, M. J., & Pawlowicz, R. (2008). Estuarine forcing of a river plume by river flow and tides. *Journal of Geophysical Research: Oceans (1978–2012)*, *113*(C9).

Halverson, M. J., & Pawlowicz, R. (2013). High-resolution observations of chlorophyll-a biomass from an instrumented ferry: Influence of the Fraser River plume from 2003 to 2006. *Continental Shelf Research*, *59*, 52–64. http://doi.org/10.1016/j.csr.2013.04.010

Harrison, P. J., Fulton, J. D., Taylor, F. J. R., & Parsons, T. R. (1983). Review of the biological oceanography of the Strait of Georgia: pelagic environment. *Canadian Journal of Fisheries and Aquatic Sciences*, *40*(7), 1064–1094.

Henson, S. A., Dunne, J. P., & Sarmiento, J. L. (2009). Decadal variability in North Atlantic phytoplankton blooms. *Journal of Geophysical Research*, *114*(C4), C04013. http://doi.org/10.1029/2008JC005139

Henson, S. A., & Thomas, A. C. (2007). Interannual variability in timing of bloom initiation in the California Current System. *Journal of Geophysical Research*, *112*(C8), C08007. http://doi.org/10.1029/2006JC003960

Hoff, R. M., Harwood, M., Sheppard, A., Froude, F., Martin, J. B., & Strapp, W. (1997). Use of airborne lidar to determine aerosol sources and movement in the Lower Fraser Valley (LFV), BC. *The Lower Fraser Valley Oxidants/Pacific '93 Field Study*, *31*(14), 2123–2134. http://doi.org/http://dx.doi.org/10.1016/S1352-2310(96)00302-0

Hoge, F. E., Vodacek, A., & Blough, N. V. (1993). Inherent optical properties of the ocean: retrieval of the absorption coefficient of chromophoric dissolved organic matter from fluorescence measurements. *Limnology and Oceanography*, *38*(7), 1394–1402.

Holben, B. N., Eck, T. F., Slutsker, I., Tanre, D., Buis, J. P., Setzer, A., … Nakajima, T. (1998). AERONET—A federated instrument network and data archive for aerosol characterization. *Remote Sensing of Environment*, *66*(1), 1–16.

Holm-Hansen, O., Lorenzen, C. J., Holmes, R. W., & Strickland, J. D. H. (1965). Fluorometric determination of chlorophyll. *Journal Du Conseil*, *30*(1), 3–15.

Hooker, S., Firestone, E. R., Patt, F. S., Barnes, R. A., Eplee Jr, R. E., Franz, B. A., … Bailey, S. W. (2003). Algorithm updates for the fourth SeaWiFS data reprocessing.

Huber, P. J. (1981). Robust Statistics. *John Wiley*.

Hubert Loisel, V. V. C. J. and D. N. D. (2013). *Topics in Oceanography*. (E. Zambianchi, Ed.). InTech. http://doi.org/10.5772/50266

Huisman, J., Pham Thi, N. N., Karl, D. M., & Sommeijer, B. (2006). Reduced mixing generates oscillations and chaos in the oceanic deep chlorophyll maximum. *Nature*, *439*(7074), 322–5. http://doi.org/10.1038/nature04245

Jackson, J. M., Thomson, R. E., Brown, L. N., Willis, P. G., & Borstad, G. A. (2015). Satellite chlorophyll off the British Columbia coast, 1997-2010. *Journal of Geophysical Research: Oceans*, n/a–n/a. http://doi.org/10.1002/2014JC010496

Jamet, C., Loisel, H., Kuchinke, C. P., Ruddick, K., Zibordi, G., & Feng, H. (2011). Comparison of three SeaWiFS atmospheric correction algorithms for turbid waters using AERONET-OC measurements. *Remote Sensing of Environment*, *115*(8), 1955–1965. http://doi.org/10.1016/j.rse.2011.03.018

Ji, R., Edwards, M., Mackas, D. L., Runge, J. A., & Thomas, A. C. (2010). Marine plankton phenology and life history in a changing climate: current research and future directions. *Journal of Plankton Research*, *32*(10), 1355–1368. http://doi.org/10.1093/plankt/fbq062

Johannessen, S. C., Macdonald, R. W., & Paton, D. W. (2003). A sediment and organic carbon budget for the greater Strait of Georgia. *Estuarine, Coastal and Shelf Science*, *56*, 845–860. http://doi.org/10.1016/S0272-7714(02)00303-7

Johannessen, S. C., Masson, D., & Macdonald, R. W. (2006). Distribution and cycling of suspended particles inferred from transmissivity in the strait of Georgia, ham strait and Juan de Fuca Strait. *Atmosphere-Ocean*, *44*(1), 17–27.

Jönsson, P., & Eklundh, L. (2004). TIMESAT - A program for analyzing time-series of satellite sensor data. *Computers and Geosciences*, *30*(8), 833–845. http://doi.org/10.1016/j.cageo.2004.05.006

Kahru, M., & Mitchell, B. G. (2001). Seasonal and nonseasonal variability of satellite-derived chlorophyll and colored dissolved organic matter concentration in the California Current. *Journal of Geophysical Research*, *106*, 2517. http://doi.org/10.1029/1999JC000094

Keith, D. J., Yoder, J. a, & Freeman, S. a. (2002). Spatial and Temporal Distribution of Coloured Dissolved Organic Matter (CDOM) in Narragansett Bay, Rhode Island: Implications for Phytoplankton in Coastal Waters. *Estuarine, Coastal and Shelf Science*, *55*(5), 705–717. http://doi.org/10.1006/ecss.2001.0922

Kiefer, D. A. (1973). Fluorescence properties of natural phytoplankton populations. *Marine Biology*, *22*(3), 263–269. http://doi.org/10.1007/BF00389180

Kirk, J. T. O. (1994). *Light and photosynthesis in aquatic ecosystems*. Cambridge university press.

Kirk, J. T. O. (2010). *Light and Photosynthesis in Aquatic Ecosystems*. Cambridge University Press. Retrieved from https://books.google.com/books?id=DXCl0fw__noC&pgis=1

Knaeps, E., Dogliotti, A. I., Raymaekers, D., Ruddick, K., & Sterckx, S. (2012). In situ evidence of non-zero reflectance in the OLCI 1020nm band for a turbid estuary. *Remote Sensing of Environment*, *120*, 133–144. http://doi.org/10.1016/j.rse.2011.07.025

Komick, N. M. (2007). *Remote Sensing Chlorophyll-a in the Strait of Georgia*. ProQuest.

Komick, N. M., Costa, M. P. F., & Gower, J. (2009). Bio-optical algorithm evaluation for MODIS for western Canada coastal waters: An exploratory approach using in situ reflectance. *Remote Sensing of Environment*, *113*(4), 794–804. http://doi.org/10.1016/j.rse.2008.12.005

Kowalczuk, P., Olszewski, J., Darecki, M., & Kaczmarek, S. (2005). Empirical relationships between coloured dissolved organic matter (CDOM) absorption and apparent optical properties in Baltic Sea waters. *International Journal of Remote Sensing*, *26*(2), 345–370.

Kuchinke, C. P., Gordon, H. R., Harding, L. W., & Voss, K. J. (2009). Spectral optimization for constituent retrieval in Case 2 waters II: Validation study in the Chesapeake Bay. *Remote Sensing of Environment*, *113*(3), 610–621. http://doi.org/10.1016/j.rse.2008.11.002

Lee, B., Ahn, J. H., Park, Y., & Kim, S. (2013). Turbid water atmospheric correction for GOCI : Modification of MUMM algorithm, *29*(2), 73–82.

Lee, Z., Arnone, R., Hu, C., Werdell, P. J., & Lubac, B. (2010). Uncertainties of optical parameters and their propagations in an analytical ocean color inversion algorithm. *Applied Optics*, *49*(3), 369–381. http://doi.org/10.1364/AO.49.000369

Lee, Z., Carder, K. L., Mobley, C. D., Steward, R. G., & Patch, J. S. (1998). Hyperspectral Remote Sensing for Shallow Waters. I. A Semianalytical Model. *Applied Optics*, *37*(27), 6329. http://doi.org/10.1364/AO.37.006329

Letelier, R. (1996). An analysis of chlorophyll fluorescence algorithms for the moderate resolution imaging spectrometer (MODIS). *Remote Sensing of Environment*, *58*(2), 215–223. http://doi.org/10.1016/S0034-4257(96)00073-9

Leys, C., Ley, C., Klein, O., Bernard, P., & Licata, L. (2013). Detecting outliers: Do not use standard deviation around the mean, use absolute deviation around the median. *Journal of Experimental Social Psychology*, *49*(4), 764–766. http://doi.org/http://dx.doi.org/10.1016/j.jesp.2013.03.013

Li, M., Gargett, A., & Denman, K. (2000). What Determines Seasonal and Interannual Variability of Phytoplankton and Zooplankton in Strongly Estuarine Systems? *Estuarine, Coastal and Shelf Science*, *50*(4), 467–488. http://doi.org/http://dx.doi.org/10.1006/ecss.2000.0593

Litaker, W., Duke, C. S., Kenney, B. E., & Ramus, J. (1987). Short-term environmental variability and phytoplankton abundance in a shallow tidal estuary. *Marine Biology*, *96*(1), 115–121. http://doi.org/10.1007/BF00394844

Loos, E. A., & Costa, M. (2010). Inherent optical properties and optical mass classification of the waters of the Strait of Georgia, British Columbia, Canada. *Progress in Oceanography*, *87*(1), 144–156.

Louis, A. (1997). Temporal variations among planktonic diatom assemblages in a turbulent environment of the southern Strait of Georgia, British Columbia, Canada. *Mar Ecol Prog Ser*, *150*, 263–274.

Maritorena, S., Siegel, D. A., & Peterson, A. R. (2002). Optimization of a semianalytical ocean color model for global-scale applications. *Applied Optics*, *41*(15), 2705. http://doi.org/10.1364/AO.41.002705

Martin Taylor, S. (2009). Transformative ocean science through the VENUS and NEPTUNE Canada ocean observing systems. *Nuclear Instruments and Methods in Physics Research Section A: Accelerators, Spectrometers, Detectors and Associated Equipment*, *602*(1), 63–67. http://doi.org/10.1016/j.nima.2008.12.019

Masson, D., & Cummins, P. F. (2004). Observations and modeling of seasonal variability in the Straits of Georgia and Juan de Fuca. *Journal of Marine Research*, *62*(4), 491–516.

Masson, D., & Peña, A. (2009). Chlorophyll distribution in a temperate estuary: The Strait of Georgia and Juan de Fuca Strait. *Estuarine, Coastal and Shelf Science*, *82*(1), 19–28. http://doi.org/http://dx.doi.org/10.1016/j.ecss.2008.12.022

Masson, D., & Perry, R. I. (2013). The Strait of Georgia Ecosystem Research Initiative: An overview. *Progress in Oceanography*, *115*, 1–5. http://doi.org/10.1016/j.pocean.2013.05.009

MathWorks. (2015). Pairwise distance betweena pair of objects: Users Guide (2015a). Retrieved January 29, 2015, from http://www.mathworks.com/help/stats/pdist.html

McCain, C., Hooker, S., Feldman, G., & Bontempi, P. (2006). Satellite data for ocean biology, biogeochemistry, and climate research. *Eos, Transactions American Geophysical Union*, *87*(34), 337–343.

McClain, C. R. (2009). A decade of satellite ocean color observations*. *Annual Review of Marine Science*, *1*, 19–42.

Mcclain, C. R., Ainsworth, E. J., Barnes, R. a, Eplee, R. E., Patt, F. S., Robinson, W. D., … Bailey, S. W. (2000). SeaWiFS Postlaunch Technical Report Series Volume 9 , SeaWiFS Postlaunch Calibration and Validation Analyses , Part 1, *9*, 1–81.

Meister, G., Franz, B. A., Kwiatkowska, E. J., & McClain, C. R. (2012). Corrections to the calibration of MODIS Aqua ocean color bands derived from SeaWiFS data. *Geoscience and Remote Sensing, IEEE Transactions on*, *50*(1), 310–319.

Mélin, F., Clerici, M., Zibordi, G., Holben, B. N., & Smirnov, A. (2010). Validation of SeaWiFS and MODIS aerosol products with globally distributed AERONET data. *Remote Sensing of Environment*, *114*(2), 230–250. http://doi.org/10.1016/j.rse.2009.09.003

Mélin, F., Zibordi, G., Carlund, T., Holben, B. N., & Stefan, S. (2013). Validation of SeaWiFS and MODIS Aqua/Terra aerosol products in coastal regions of European marginal seas. *Oceanologia*, *55*(1), 27–51. http://doi.org/10.5697/oc.55-1.027

Melin, F., Zibordi, G., & Holben, B. N. (2013). Assessment of the aerosol products from the SeaWiFS and MODIS ocean-color missions. *IEEE Geoscience and Remote Sensing Letters*, *10*(5), 1185–1189. http://doi.org/10.1109/LGRS.2012.2235408

Miller, R. L., Castillo, C. E. Del, & McKee, B. A. (2005). *Remote Sensing of Coastal Aquatic Environments: Technologies, Techniques and Applications*. Springer Science & Business Media. Retrieved from https://books.google.com/books?id=PljY6fbL2cEC&pgis=1

Minu, P., Lotliker, A. A., Shaju, S. S., SanthoshKumar, B., Ashraf, P. M., & Meenakumari, B. (2014). Effect of optically active substances and atmospheric correction schemes on remote-sensing reflectance at a coastal site off Kochi. *International Journal of*

Remote Sensing, *35*(14), 5434–5447. http://doi.org/10.1080/01431161.2014.926420

Mobley, C. D. (1999). Estimation of the remote-sensing reflectance from above-surface measurements. *Applied Optics*, *38*(36), 7442. Retrieved from http://www.opticsinfobase.org/ao/abstract.cfm?uri=ao-38-36-7442

Montes-Hugo, M. A., Gould, R., Arnone, R., Ducklow, H., Carder, K., English, D., … Kerfoot, J. (2009). <title>Beyond the first optical depth: fusing optical data from ocean color imagery and gliders</title>. In R. J. Frouin (Ed.), *SPIE Optical Engineering + Applications* (p. 74590N–74590N–9). International Society for Optics and Photonics. http://doi.org/10.1117/12.831429

More, S., Pradeep Kumar, P., Gupta, P., Devara, P. C. S., & Aher, G. R. (2013). Comparison of aerosol products retrieved from AERONET, MICROTOPS and MODIS over a tropical urban city, Pune, India. *Aerosol and Air Quality Research*, *13*(1), 107–121. http://doi.org/10.4209/aaqr.2012.04.0102

Morel, A. (1980). In-water and remote measurements of ocean color. *Boundary-Layer Meteorology*, *18*(2), 177–201.

Morel, A. (1988). Optical modeling of the upper ocean in relation to its biogenous matter content (case I waters). *Journal of Geophysical Research*, *93*(C9), 10749. http://doi.org/10.1029/JC093iC09p10749

Morel, A., Huot, Y., Gentili, B., Werdell, P. J., Hooker, S. B., & Franz, B. A. (2007). Examining the consistency of products derived from various ocean color sensors in open ocean (Case 1) waters in the perspective of a multi-sensor approach. *Remote Sensing of Environment*, *111*(1), 69–88. http://doi.org/10.1016/j.rse.2007.03.012

Morel, A., & Prieur, L. (1977). Analysis of variations in ocean color. *Limnol.Oceanogr.*, *22*(4), 709–722.

Moreno-Madriñán, M. J., & Fischer, A. M. (2013). Performance of the MODIS FLH algorithm in estuarine waters: A multi-year (2003-2010) analysis from Tampa Bay, Florida (USA). *International Journal of Remote Sensing*, *34*(19), 6467–6483. http://doi.org/http://dx.doi.org/10.1080/01431161.2013.804227

Mouw, C. B., & Yoder, J. a. (2005). Primary production calculations in the Mid-Atlantic Bight, including effects of phytoplankton community size structure. *Limnology and Oceanography*, *50*(4), 1232–1243. http://doi.org/10.4319/lo.2005.50.4.1232

Mueller, J. L., McClain, G. S. F. C. R., Mueller, J. L., Bidigare, R. R., Trees, C., Balch, W. M., … Van, L. (2003). Ocean optics protocols for satellite ocean color sensor validation,

revision 5, volume V: Biogeochemical and bio-optical measurements and data analysis protocols. *NASA Tech.Memo*, *211621*, 36.

Mustapha, S. Ben, Bélanger, S., & Larouche, P. (2014a). Evaluation of ocean color algorithms in the southeastern Beaufort Sea, Canadian Arctic: New parameterization using SeaWiFS, MODIS, and MERIS spectral bands. *Canadian Journal of Remote Sensing*, *38*(5), 535–556. http://doi.org/10.5589/m12-045

Mustapha, S. Ben, Bélanger, S., & Larouche, P. (2014b). Evaluation of ocean color algorithms in the southeastern Beaufort Sea, Canadian Arctic: New parameterization using SeaWiFS, MODIS, and MERIS spectral bands. *Canadian Journal of Remote Sensing*, *38*(5), 535–556. http://doi.org/10.5589/m12-045

O'Reilly, J. E., Maritorena, S., O'Brien, M. C., Siegel, D. A., Toole, D., Menzies, D., Smith, R. C., Mueller, J. L., Mitchell, B. G., Kahru, M., Chavez, F. P., S., P., Cota, G. F., Hooker, S. B., McClain, C. R., Carder, K. L., M.-K., F., Harding, L., Magnuson, A., Phinney, D., Moore, G. F., Aiken, J., A., & K. R., Letelier, R., Culver, M. (2000). *Volume 11, SeaWiFS postlaunch calibration and validation analyses, part 3. Tech. Rep.*

Pawlowicz, R., Allen, S., Dower, J., Lee, R., Harris, S., Halverson, M., … Bird, T. (2003). Stratogem–The Strait of Georgia Ecosystem Project. In *Proc Georgia Basin/Puget Sound Res Conf* (Vol. 2003, pp. 1–5).

Pawlowicz, R., Riche, O., & Halverson, M. (2007). The circulation and residence time of the Strait of Georgia using a simple mixing-box approach. *Atmosphere-Ocean*, *45*(4), 173–193.

Perry, R. I., & Masson, D. (2013). An integrated analysis of the marine social–ecological system of the Strait of Georgia, Canada, over the past four decades, and development of a regime shift index. *Progress in Oceanography*, *115*, 14–27. http://doi.org/10.1016/j.pocean.2013.05.021

Platt, T., Fuentes-Yaco, C., & Frank, K. T. (2003). Marine ecology: Spring algal bloom and larval fish survival. *Nature*, *423*(6938), 398–399. Retrieved from http://dx.doi.org/10.1038/423398b

Platt, T., & Sathyendranath, S. (2008). Ecological indicators for the pelagic zone of the ocean from remote sensing. *Earth Observations for Marine and Coastal Biodiversity and Ecosystems Special Issue*, *112*(8), 3426–3436. http://doi.org/http://dx.doi.org/10.1016/j.rse.2007.10.016

Platt, T., White, G. N., Zhai, L., Sathyendranath, S., & Roy, S. (2009). The phenology of phytoplankton blooms: Ecosystem indicators from remote sensing. *Ecological Modelling*, *220*(21), 3057–3069. http://doi.org/10.1016/j.ecolmodel.2008.11.022

Pospelova, V., Esenkulova, S., Johannessen, S. C., O'Brien, M. C., & Macdonald, R. W. (2010). Organic-walled dinoflagellate cyst production, composition and flux from 1996 to 1998 in the central Strait of Georgia (BC, Canada): A sediment trap study. *Marine Micropaleontology*, *75*(1–4), 17–37. http://doi.org/http://dx.doi.org/10.1016/j.marmicro.2010.02.003

Preikshot, D., Beamish, R. J., & Neville, C. M. (2013). A dynamic model describing ecosystem-level changes in the Strait of Georgia from 1960 to 2010. *Progress in Oceanography*, *115*, 28–40. http://doi.org/10.1016/j.pocean.2013.05.020

Racault, M.-F., Le Quéré, C., Buitenhuis, E., Sathyendranath, S., & Platt, T. (2012). Phytoplankton phenology in the global ocean. *Ecological Indicators*, *14*(1), 152–163. http://doi.org/10.1016/j.ecolind.2011.07.010

Radenac, M.-H., Messié, M., Léger, F., & Bosc, C. (2013). A very oligotrophic zone observed from space in the equatorial Pacific warm pool. *Remote Sensing of Environment*, *134*, 224–233. http://doi.org/10.1016/j.rse.2013.03.007

RANTAJARVI, E. (1998). Effect of sampling frequency on detection of natural variability in phytoplankton: unattended high-frequency measurements on board ferries in the Baltic Sea. *ICES Journal of Marine Science*, *55*(4), 697–704. http://doi.org/10.1006/jmsc.1998.0384

Riche, O., Johannessen, S. C., & Macdonald, R. W. (2014). Why timing matters in a coastal sea: Trends, variability and tipping points in the Strait of Georgia, Canada. *Journal of Marine Systems*, *131*, 36–53. http://doi.org/10.1016/j.jmarsys.2013.11.003

Robinson, I. S. (2007). Remote Assessment of Ocean Color for Interpretation of Satellite Visible Imagery: A review: By H. R. Gordon and A. Y. Morel. Springer-Verlag, Berlin, 1983. Pp. 114. DM 58 (approx. US$22.5). *Quarterly Journal of the Royal Meteorological Society*, *111*(469), 872–872. http://doi.org/10.1002/qj.49711146913

Roerink, G. J., Menenti, M., & Verhoef, W. (2000). Reconstructing cloudfree NDVI composites using Fourier analysis of time series. *International Journal of Remote Sensing*, *21*(9), 1911–1917. http://doi.org/10.1080/014311600209814

Ruddick, K. G., De Cauwer, V., Park, Y.-J., & Moore, G. (2006). Seaborne measurements of near infrared water-leaving reflectance: The similarity spectrum for turbid

waters. *Limnology and Oceanography*, *51*(2), 1167–1179. http://doi.org/10.4319/lo.2006.51.2.1167

Ruddick, K. G., Ovidio, F., & Rijkeboer, M. (2000). Atmospheric correction of SeaWiFS imagery for turbid coastal and inland waters. *Applied Optics*, *39*(6), 897–912.

Ruddick, K., & Vanhellemont, Q. (2015). USE OF THE NEW OLCI AND SLSTR BANDS FOR ATMOSPHERIC CORRECTION OVER TURBID COASTAL AND INLAND WATERS, (June), 2–5.

Sanwlani, N., Chauhan, P., & Navalgund, R. R. (2011). Atmospheric correction using 1240 and 2130 nm combination of MODIS SWIR channels. *Asian Journal of Geoinformatics*, *11*(1), 1–9.

Schurman, M. I., Lee, T., Desyaterik, Y., Schichtel, B. A., Kreidenweis, S. M., & Collett, J. L. (2015). Transport, biomass burning, and in-situ formation contribute to fine particle concentrations at a remote site near Grand Teton National Park. *Atmospheric Environment*, *112*, 257–268. http://doi.org/10.1016/j.atmosenv.2015.04.043

Schuster, G. L., Dubovik, O., & Holben, B. N. (2006). Angstrom exponent and bimodal aerosol size distributions. *Journal of Geophysical Research*, *111*(D7), D07207. http://doi.org/10.1029/2005JD006328

Schutgens, N. A. J., Nakata, M., & Nakajima, T. (2013). Validation and empirical correction of MODIS AOT and AE over ocean. *Atmospheric Measurement Techniques*, *6*(9), 2455–2475. http://doi.org/10.5194/amt-6-2455-2013

Schweigert, J. F., Thompson, M., Fort, C., Hay, D. E., Therriault, T. W., & Brown, L. N. (2013). Factors linking pacific herring (clupea pallasi) productivity and the spring plankton bloom in the strait of Georgia, British Columbia, Canada. *Progress in Oceanography*, *115*, 103–110. http://doi.org/10.1016/j.pocean.2013.05.017

Shettle, E. P., & Fenn, R. W. (1979). No Title. *Models for the Aerosols of the Lower Atmosphere and the Effects of Humidity Variations on Their Optical Properties*.

Shi, W., & Wang, M. (2009). An assessment of the black ocean pixel assumption for MODIS SWIR bands. *Remote Sensing of Environment*, *113*(8), 1587–1597.

Shi, W., & Wang, M. (2014a). Ocean reflectance spectra at the red, near-infrared, and shortwave infrared from highly turbid waters: A study in the Bohai Sea, Yellow Sea, and East China Sea. *Limnology and Oceanography*, *59*(2), 427–444. http://doi.org/10.4319/lo.2014.59.2.0427

Shi, W., & Wang, M. (2014b). Ocean reflectance spectra at the red, near-infrared, and shortwave infrared from highly turbid waters: A study in the Bohai Sea, Yellow Sea, and East China Sea. *Limnology and Oceanography*, *59*(2), 427–444. http://doi.org/10.4319/lo.2014.59.2.0427

Siegel, D. a, Doney, S. C., & Yoder, J. a. (2002). The North Atlantic spring phytoplankton bloom and Sverdrup's critical depth hypothesis. *Science (New York, N.Y.)*, *296*(5568), 730–733. http://doi.org/10.1126/science.1069174

Siegel, D. A., Wang, M., Maritorena, S., & Robinson, W. (2000). Atmospheric correction of satellite ocean color imagery: the black pixel assumption. *Applied Optics*, *39*(21), 3582–3591.

Sournia, A., Birrien, J.-L., Douvillé, J.-L., Klein, B., & Viollier, M. (1987). A daily study of the diatom spring bloom at Roscoff (France) in 1985. I. The spring bloom within the annual cycle. *Estuarine, Coastal and Shelf Science*, *25*(3), 355–367. http://doi.org/10.1016/0272-7714(87)90078-3

Sprules, G., Collins, A. K., Allen, S. E., & Pawlowicz, R. (2009). The role of wind in determining the timing of the spring bloom in the Strait of Georgia. *Canadian Journal of Fisheries and Aquatic Sciences*, *66*(9), 1597–1616.

Stelzenmüller, V., Breen, P., Stamford, T., Thomsen, F., Badalamenti, F., Borja, Á., … Dankers, N. (2013). Monitoring and evaluation of spatially managed areas: a generic framework for implementation of ecosystem based marine management and its application. *Marine Policy*, *37*, 149–164.

Strom, S. L., Brainard, M. A., Holmes, J. L., & Olson, M. B. (2001). Phytoplankton blooms are strongly impacted by microzooplankton grazing in coastal North Pacific waters. *Marine Biology*, *138*(2), 355–368. http://doi.org/10.1007/s002270000461

Stronach, J. A. (1981). The Fraser River plume, Strait of Georgia. *Ocean Management*, *6*(2–3), 201–221. http://doi.org/http://dx.doi.org.ezproxy.library.uvic.ca/10.1016/0302-184X(81)90039-1

Stumpf, R. P., Arnone, R. A., Gould, R. W., Martinolich, P. M., & Ransibrahmanakul, V. (2003). A partially coupled ocean-atmosphere model for retrieval of water-leaving radiance from SeaWiFS in coastal waters. *NASA Tech.Memo*, *206892*, 51–59.

Sutton, J. N., Johannessen, S. C., & Macdonald, R. W. (2013). A nitrogen budget for the strait of Georgia, British Columbia, with emphasis on particulate nitrogen and dissolved inorganic nitrogen. *Biogeosciences*, *10*(11), 7179–7194. http://doi.org/10.5194/bg-10-7179-2013

Sverdup, H. . (1953). On conditions for the vernal blooming of phytoplankton. *Jounral Du Conseil*, *18*(3), 287–295.

Takemura, T., Okamoto, H., Maruyama, Y., Numaguti, A., Higurashi, A., & Nakajima, T. (2000). Global three-dimensional simulation of aerosol optical thickness distribution of various origins. *Journal of Geophysical Research: Atmospheres (1984–2012)*, *105*(D14), 17853–17873.

Thomson, R. E. (1981). *Oceanography of the British Columbia coast* (Vol. 56). Department of Fisheries and Oceans Sidney, BC.

Thomson, R. E., Beamish, R. J., Beacham, T. D., Trudel, M., Whitfield, P. H., & Hourston, R. a. S. (2012). Anomalous Ocean Conditions May Explain the Recent Extreme Variability in Fraser River Sockeye Salmon Production. *Marine and Coastal Fisheries*, *4*(1), 415–437. http://doi.org/10.1080/19425120.2012.675985

Tilstone, G. H., Lotliker, A. A., Miller, P. I., Ashraf, P. M., Kumar, T. S., Suresh, T., … Menon, H. B. (2013). Assessment of MODIS-Aqua chlorophyll-a algorithms in coastal and shelf waters of the eastern Arabian Sea. *Continental Shelf Research*, *65*, 14–26. http://doi.org/10.1016/j.csr.2013.06.003

Tommasi, D. A. G., Routledge, R. D., Hunt, B. P. V., & Pakhomov, E. A. (2013). The seasonal development of the zooplankton community in a British Columbia (Canada) fjord during two years with different spring bloom timing. *Marine Biology Research*, *9*(2), 129–144. http://doi.org/10.1080/17451000.2012.708044

Twardowski, M. S., & Donaghay, P. L. (2001). Separating in situ and terrigenous sources of absorption by dissolved materials in coastal waters. *Journal of Geophysical Research: Oceans (1978–2012)*, *106*(C2), 2545–2560.

Vanhellemont, Q., & Ruddick, K. (2015). Advantages of high quality SWIR bands for ocean colour processing: Examples from Landsat-8. *Remote Sensing of Environment*, *161*, 89–106. http://doi.org/10.1016/j.rse.2015.02.007

Vingarzan, R., & Thomson, B. (2004). Temporal variation in daily concentrations of ozone and acid-related substances at Saturna Island, British Columbia. *Journal of the Air & Waste Management Association*, *54*(4), 459–472.

Volpe, G., Santoleri, R., Vellucci, V., Ribera d'Alcalà, M., Marullo, S., & D'Ortenzio, F. (2007). The colour of the Mediterranean Sea: Global versus regional bio-optical algorithms evaluation and implication for satellite chlorophyll estimates. *Remote Sensing of Environment*, *107*(4), 625–638. http://doi.org/10.1016/j.rse.2006.10.017

Waldichuk, M. (1957). Physical oceanography of the Strait of Georgia, British Columbia. *Journal of the Fisheries Board of Canada*, *14*(3), 321–486.

Wang & Shi, W., M. (2005). Estimation of ocean contribution at the MODIS near-infrared wavelengths along the east coast of the US: Two case studies.. *Geophysical Research Letters*, *32*(13).

Wang, C. (2015, May 1). Oxygen budgets and productivity estimates in the Strait of Georgia from a continuous ferry-based monitoring system. University of British Columbia. Retrieved from https://circle.ubc.ca/handle/2429/52405

Wang, M. (2002). The Rayleigh lookup tables for the SeaWiFS data processing: accounting for the effects of ocean surface roughness. *International Journal of Remote Sensing*, *23*(13), 2693–2702.

Wang, M. (2007). Remote sensing of the ocean contributions from ultraviolet to near-infrared using the shortwave infrared bands: simulations. *Applied Optics*, *46*(9), 1535–1547.

Wang, M., & Bailey, S. W. (2001). Correction of sun glint contamination on the SeaWiFS ocean and atmosphere products. *Applied Optics*, *40*(27), 4790–4798.

Wang, M., & Shi, W. (2012). Sensor Noise Effects of the SWIR Bands on MODIS-Derived Ocean Color Products. *IEEE Transactions on Geoscience and Remote Sensing*, *50*(9), 3280–3292. http://doi.org/10.1109/TGRS.2012.2183376

Wang, M., Son, S., & Shi, W. (2009a). Evaluation of MODIS SWIR and NIR-SWIR atmospheric correction algorithms using SeaBASS data. *Remote Sensing of Environment*, *113*(3), 635–644. http://doi.org/http://dx.doi.org.ezproxy.library.uvic.ca/10.1016/j.rse.2008.11.005

Wang, M., Son, S., & Shi, W. (2009b). Evaluation of MODIS SWIR and NIR-SWIR atmospheric correction algorithms using SeaBASS data. *Remote Sensing of Environment*, *113*(3), 635–644.

Wang, M., Son, S., Zhang, Y., & Shi, W. (2013a). Remote sensing of water optical property for China's inland Lake Taihu using the SWIR atmospheric correction with 1640 and 2130 nm bands. *Selected Topics in Applied Earth Observations and Remote Sensing, IEEE Journal of*, *6*(6), 2505–2516.

Wang, M., Son, S., Zhang, Y., & Shi, W. (2013b). Remote Sensing of Water Optical Property for China's Inland Lake Taihu Using the SWIR Atmospheric Correction With 1640 and 2130 nm Bands.

Warren Liao, T. (2005). Clustering of time series data—a survey. *Pattern Recognition*, *38*(11), 1857–1874. http://doi.org/10.1016/j.patcog.2005.01.025

Welsch, C., Swenson, H., Cota, S. A., Deluccia, F., Haas, J. M., Spring, S., … Ardanuy, P. E. (2001). VIIRS (Visible Infrared Imager Radiometer Suite): A Next-Generation Operational Environmental Sensor for NPOESS, (C), 1020–1022.

Werdell, P. J., & Bailey, S. W. (2005). An improved in-situ bio-optical data set for ocean color algorithm development and satellite data product validation. *Remote Sensing of Environment*, *98*, 122–140. http://doi.org/10.1016/j.rse.2005.07.001

Werdell, P. J., Bailey, S. W., Franz, B. A., Harding Jr, L. W., Feldman, G. C., & McClain, C. R. (2009). Regional and seasonal variability of chlorophyll-a in Chesapeake Bay as observed by SeaWiFS and MODIS-Aqua. *Remote Sensing of Environment*, *113*(6), 1319–1330.

Werdell, P. J., Franz, B. A., & Bailey, S. W. (2010). Evaluation of shortwave infrared atmospheric correction for ocean color remote sensing of Chesapeake Bay. *Remote Sensing of Environment*, *114*(10), 2238–2247. http://doi.org/http://dx.doi.org/10.1016/j.rse.2010.04.027

Werdell, P. J., Franz, B. A., Bailey, S. W., Harding Jr, L. W., & Feldman, G. C. (2007). Approach for the long-term spatial and temporal evaluation of ocean color satellite data products in a coastal environment. In *Optical Engineering Applications* (p. 66800G–66800G–12). International Society for Optics and Photonics.

Williams, G. N., Dogliotti, A. I., Zaidman, P., Solis, M., Narvarte, M. A., González, R. C., … Gagliardini, D. A. (2013). Assessment of remotely-sensed sea-surface temperature and chlorophyll-a concentration in San Matías Gulf (Patagonia, Argentina). *Continental Shelf Research*, *52*, 159–171. http://doi.org/10.1016/j.csr.2012.08.014

Woodroffe, A., & Round, A. (2008). Design and operation of a multi node cabled observatory. In *OCEANS 2008* (pp. 1–5). IEEE. http://doi.org/10.1109/OCEANS.2008.5151905

Yin, K. D., Goldblatt, R. H., Harrison, P. J., St. John, M., Clifford, P. J., & Beamish, R. J. (1997). Importance of wind and river discharge in influencing nutrient dynamics and phytoplankton production in summer in the central Strait of Georgia. *Marine Ecology-Progress Series*, *161*, 173–183.

Yin, K., Harrison, P., Goldblatt, R., & Beamish, R. (1996). Spring bloom in the central Strait of Georgia:interactions of river discharge, winds and grazing. *Marine Ecology Progress Series*, *138*(1-3), 255–263. http://doi.org/10.3354/meps138255

Yunker, M. B., & Macdonald, R. W. (2003). Alkane and PAH depositional history, sources and fluxes in sediments from the Fraser River Basin and Strait of Georgia, Canada. *Organic Geochemistry*, *34*(10), 1429–1454. http://doi.org/http://dx.doi.org.ezproxy.library.uvic.ca/10.1016/S0146-6380(03)00136-0

Zhai, L., Platt, T., Tang, C., Sathyendranath, S., & Hernandez Walls, R. (2011). Phytoplankton phenology on the Scotian Shelf. *ICES Journal of Marine Science*, *68*(4), 781–791. http://doi.org/10.1093/icesjms/fsq175

Zhu, W.-J., Shen, F., & Hong, G.-L. (2010). [Optical characteristics of colored dissolved organic material (CDOM) in Yangtze Estuary]. *Huan Jing Ke Xue= Huanjing Kexue / [bian Ji, Zhongguo Ke Xue Yuan Huan Jing Ke Xue Wei Yuan Hui "Huan Jing Ke Xue" Bian Ji Wei Yuan Hui.]*, *31*(10), 2292–8. Retrieved from http://www.ncbi.nlm.nih.gov/pubmed/21229734

Zibordi, G., Berthon, J.-F., Mélin, F., D'Alimonte, D., & Kaitala, S. (2009). Validation of satellite ocean color primary products at optically complex coastal sites: Northern Adriatic Sea, Northern Baltic Proper and Gulf of Finland. *Remote Sensing of Environment*, *113*(12), 2574–2591.

Zibordi, G., Holben, B., Mélin, F., D'Alimonte, D., Berthon, J.-F., Slutsker, I., & Giles, D. (2010). AERONET-OC: an overview. *Canadian Journal of Remote Sensing*, *36*(5), 488–497.

Zibordi, G., Mélin, F., Berthon, J.-F., Holben, B., Slutsker, I., Giles, D., … Schuster, G. (2009). AERONET-OC: a network for the validation of ocean color primary products. *Journal of Atmospheric and Oceanic Technology*, *26*(8), 1634–1651.